

Aus dem
Institut für Experimentelle Pneumologie
Klinikum der Ludwig-Maximilians-Universität München

und dem
Comprehensive Pneumology Center (CPC)
Helmholtz Center Munich



**Virus infections as risk factors in the development of
bronchopulmonary dysplasia (BPD)**

Dissertation
zum Erwerb des Doctor of Philosophy (Ph.D.)
an der Medizinischen Fakultät der
Ludwig-Maximilians-Universität München

vorgelegt von
Anna Michaylovna Dmitrieva

aus
Sankt Petersburg, Russische Föderation

Jahr
2024

Mit Genehmigung der Medizinischen Fakultät der
Ludwig-Maximilians-Universität München

Erstes Gutachten: Prof. Dr. Heiko Adler
Zweites Gutachten: Prof. Dr. Anne Hilgendorff
Drittes Gutachten: Prof. Dr. Andreas W. Flemmer
Viertes Gutachten: Priv. Doz. Dr. Susanne Jonat

Dekan: Prof. Dr. med. Thomas Gudermann

Tag der mündlichen Prüfung: 27.05.2024

Table of content

Abstract.....	6
List of figures	8
List of tables.....	9
1. Introduction	10
1.1. Lung development.....	10
1.2. Prematurely born infants	12
1.3. Bronchopulmonary dysplasia	13
1.4. Risk factors of BPD	19
1.5. MHV-68	25
1.6. Experimental <i>in vitro</i> BPD models	26
1.7. Experimental <i>in vivo</i> BPD models	27
1.8. Mouse models of BPD combined with virus infection.....	28
1.9. Aim of the project	30
2. Materials	31
2.1. Primary antibodies.....	31
2.2. Secondary antibodies	31
2.3. Primers	31
2.4. Cell culture	32
2.4.1. Cell lines	32
2.4.2. Media formulations.....	32
2.4.3. Reagents and chemicals.....	33
2.4.4. Buffer formulations	34
2.5. Kits	36
2.6. Consumables	36
2.7. Laboratory equipment and software	37
3. Methods.....	41
3.1. Cells	41
3.1.1. Mouse primary fibroblasts isolation from neonatal mouse lungs	41
3.1.2. Flow cytometry analysis.....	41
3.1.3. Cell culture treatment.....	42
3.1.3.1. Hyperoxia exposure.....	42
3.1.3.2. TGF β treatment.....	42
3.2. MHV-68	42
3.2.1. Virus stock preparation	42
3.2.2. Plaque assay (quantification of MHV-68).....	43

3.2.3. Cell infection	44
3.2.4. Determination of the number of infected cells	44
3.2.5. Determination of viral replication	44
3.3. Functional assays.....	45
3.3.1. Trypan blue cell counting	45
3.3.2. Wound healing "scratch" assay	45
3.3.3. Migration measurement assays	46
3.3.3.1. Cell migration assay	46
3.3.3.2. Cell Migration/Chemotaxis Assay	47
3.3.4. Apoptosis measurement assays	48
3.3.4.1. Caspase-Glo 3/7 assay	48
3.3.4.2. RealTime-Glo Annexin V Apoptosis and Necrosis Assay.....	48
3.3.5. MTT Cell viability measurements	48
3.4. Analytical assays.....	49
3.4.1. Protein isolation from cells in 2D cell culture.....	49
3.4.2. Bicinchoninic acid (BCA) assay	49
3.4.3. SDS-PAGE and immunoblotting	50
3.4.4. RNA extraction from cells in 2D cell culture	50
3.4.5. cDNA synthesis by Reverse Transcription	51
3.4.6. qRT-PCR	51
3.5. Animal experiments.....	52
3.5.1. Hyperoxia exposure	52
3.5.2. MHV-68 infection	53
3.5.3. Organs harvesting.....	53
3.5.4. Brain and lung fixation and paraffin embedding.....	54
3.5.5. Haematoxylin Eosin staining.....	54
3.5.6. Homogenization of the lung or spleen tissue	55
3.5.7. Determination of lung viral titers.....	55
3.5.8. Determination of viral load in spleens	55
3.6. Statistical analysis	56
4. Results.....	58
4.1. Effects of <i>in vitro</i> infection of mouse primary fibroblasts and CCL-206 cells by MHV-68 in the presence or absence of hyperoxia or TGF β pre-treatment	58
4.1.1. Effects of <i>in vitro</i> MHV-68 infection in mouse primary fibroblasts and CCL-206 cells	58
4.1.2. Effects of <i>in vitro</i> MHV-68 infection in mouse primary fibroblasts and CCL-206 cells following pre-exposure with hyperoxia or pretreatment with TGF- β	71
4.2. <i>In vivo</i> MHV-68 infection of C57BL/6J mice after exposure to hyperoxia.....	93

4.2.1. Establishment of a new in vivo experimental model to study viral infection and hyperoxia exposure	93
4.2.2. Hyperoxia increased the lytic MHV-68 titer in the lungs but did not change the viral genomic load in the spleen.....	95
4.2.3. Histological changes in the lung.....	96
4.2.4. MHV-68 infection and hyperoxia exposure in the first month of life significantly changed lung morphology in adults.....	98
4.2.5. Vascular development in the lungs after double-hit injury.....	105
4.2.6. The impact of Hyperoxia treatment on the regulation of developmentally relevant genes following secondary MHV-68 infection	107
5. Discussion	114
Conclusions	126
References	127
Acknowledgments.....	136
Affidavit.....	138
Confirmation of congruency.....	139

Abstract

Bronchopulmonary dysplasia (BPD) is a multifactorial chronic lung disease primarily affecting premature infants, often resulting from the complex interplay of preterm birth, mechanical ventilation, and oxygen therapy. The complicated relationship between inflammation, oxidative stress, and impaired lung growth contributes to the development of this challenging condition. The immune system of prematurely born children, often referred to as preterm or premature infants, is underdeveloped compared to those born at full term. Premature birth and the associated underdeveloped respiratory system render affected infants more susceptible to various infections. Viral infections in infants with BPD often manifest with heightened severity, posing a substantial challenge in clinical management. Virus infections represent a significant global health concern, affecting millions of individuals annually and posing a substantial burden on healthcare systems. Gammaherpesviruses, a subgroup of the Herpesviridae family, encompass notable pathogens such as Epstein-Barr virus (EBV) and Kaposi's sarcoma-associated herpesvirus (KSHV). These viruses present significant health concerns due to their association with various cancers and their intricate evasion strategies against the host immune system. Both EBV and KSHV can cause severe respiratory complications in individuals with compromised immune systems. A key challenge in studying human herpesviruses is the absence of a dependable small animal model for investigating fundamental aspects of viral pathogenesis. Murine gammaherpesvirus 68 (MHV-68) serves as a naturally occurring virus genetically related to human gammaherpesviruses, including EBV and KSHV. My study addressed the impact of MHV-68 infection on the development of BPD in one of the major lung cell types – fibroblasts: CCL-206 and neonatal primary mouse lung fibroblasts (in vitro part). This investigation presents novel outcomes resulting from early postnatal exposure to clinically significant hyperoxia concentrations ($\text{FiO}_2 = 0.4$, 24 hours) with the following MHV-68 infection.

A significant finding in this study was the observed impact of O_2 treatment ($\text{FiO}_2 = 0.4$), leading to a noteworthy decrease in Caspase 3/7 activity, necrosis, and proliferation in primary fibroblasts. Importantly, this effect occurred without any

discernible changes in cell morphology. The study suggests that hyperoxic conditions potentially trigger adaptive mechanisms in primary fibroblasts within the initial 24 hours post-exposure, moderating apoptosis and necrosis without altering cell morphology. Conversely, MHV-68 infection resulted in a substantial increase in necrosis and a decrease in apoptosis, proliferation, and cell migration capabilities. The infected cells exhibited reduced *Pdgfra* gene expression, elevated *Vegf* gene expression, and irreversible morphological changes, indicative of potential cell-cycle arrest. Virus replication curve was significantly lower in cells exposed to hyperoxia, this finding demonstrated decreased proliferation of exposed cells. Notably, CCL-206 cells, being immortalized, displayed increased Caspase 3/7 activity, potentially attributed to their artificial ability for continuous proliferation. I conducted an investigation utilizing TGF β stimulation on CCL-206 cells and primary fibroblasts to assess its potential influence on MHV-68 infection, juxtaposing its effects with those resulting from hyperoxia exposure. TGF β treatment elicited distinct impacts on cellular responses and MHV-68 infection. Specifically, within the initial 24-hour post-virus infection period, TGF β treatment exhibited no alterations in necrosis or apoptosis in fibroblasts, and it did not induce changes in cellular proliferation and migration. Owing to the disparate signaling pathways engaged, TGF β cannot serve as a suitable comparative control for in vitro hyperoxia studies.

Exploring BPD, we aimed to develop a clinically relevant animal model for studying lifelong consequences. The study employed a double-hit model involving hyperoxia exposure ($FiO_2 = 0.4$) and MHV-68 infection in neonatal mice, revealing significant changes in Radial Alveolar Count (RAC) and septal wall thickness of the adult mice, indicating altered lung morphology after mice were treated in the early days of life, emphasizing the mutual influence nature of hyperoxia and viral infection injuries in adult alveoli. MHV-68 titer in lungs was significantly increased in mice prior exposed to hyperoxia, indicating the enhanced immune response in lung cells due to the preliminary hyperoxia exposure. The study's exploration of sex-related differences uncovered notable variations in lytic MHV-68 titer, RAC, and alveolar wall thickness between male and female mice, adding an additional layer of complexity to the interplay of infection, hyperoxia, and BPD.

List of figures

Figure 1.1. Lung developmental stages in humans	11
Figure 1.2. Processes involved in the pathophysiology of bronchopulmonary dysplasia.....	16
Figure 1.3. Factors that contribute to alveolar arrest in BPD	19
Figure 1.4. A schematic diagram showing pathways associated with preterm birth may result in diminished immune responses and increased susceptibility to acute respiratory infection	22
Figure 3.5.1. Double-hit model experimental design	53
Figure 4.1. Recombinant MHV-68 expressing GFP infects CCL-206 and primary neonatal mouse lung fibroblasts	59
Figure 4.2. MHV-68 infection did not change metabolic activity in primary mouse lung fibroblasts	61
Figure 4.3. Annexin V binding after MHV-68 infection of primary neonatal mouse lung fibroblasts	62
Figure 4.4. Caspase 3/7 activity after MHV-68 infection in primary neonatal mouse lung fibroblasts in normoxia ($FiO_2 = 0.21$).....	63
Figure 4.5. Necrosis after MHV-68 infection of primary neonatal mouse lung fibroblasts	64
Figure 4.6. Images of primary neonatal mouse lung fibroblasts	64
Figure 4.7. A wound healing “scratch” assay. Primary neonatal mouse lung fibroblasts.....	65
Figure 4.8. A wound healing “scratch” assay. Primary neonatal mouse lung fibroblasts.....	66
Figure 4.9. Cell number measurements and PCNA expression analysis in MHV-68 infected mouse primary fibroblasts	67
Figure 4.10. Quantitative analysis of infected mouse primary fibroblasts migration	68
Figure 4.11. <i>Acta2</i> gene expression in CCL-206 (A) and primary neonatal mouse lung fibroblasts (B) after MHV-68 infection for 24 hours.....	69
Figure 4.12. PDGF-R α protein expression (A, B) and <i>Pdgfra</i> gene expression (C) in primary neonatal mouse lung fibroblasts after MHV-68 infection.....	70
Figure 4.13. <i>Vegf</i> gene expression in CCL-206 (A) and primary neonatal mouse lung fibroblasts (B) after MHV-68 infection	71
Figure 4.14. Recombinant MHV-68 expressing GFP infects primary neonatal mouse lung fibroblasts with prior hyperoxia exposure	72
Figure 4.15. MHV-68 replication in primary neonatal mouse lung fibroblasts under hyperoxia exposure ($FiO_2 = 0.4$)	73
Figure 4.16. MHV-68 infection and hyperoxia exposure did not change metabolic activity in the primary neonatal mouse lung fibroblasts.....	74
Figure 4.17. Annexin V binding after MHV-68 infection with or without primary exposure to hyperoxia of primary neonatal mouse lung fibroblasts	75
Figure 4.18. Caspase 3/7 activity after MHV-68 infection in primary neonatal mouse lung fibroblasts in normoxia ($FiO_2 = 0.21$) or hyperoxia ($FiO_2 = 0.4$)	76
Figure 4.19. Necrosis after hyperoxia exposure ($FiO_2 = 0.4$) for 24 hours and MHV-68 infection for 24 hours of primary neonatal mouse lung fibroblasts.....	77
Figure 4.20. Images of primary neonatal mouse lung fibroblasts	78
Figure 4.21. A wound healing “scratch” assay. Primary neonatal mouse lung fibroblasts.....	79
Figure 4.22. A wound healing “scratch” assay. Primary neonatal mouse lung fibroblasts.....	80
Figure 4.23. Cell number measurements and PCNA expression analysis in hyperoxia exposed mouse primary fibroblasts with or without following MHV-68 infection	81

Figure 4.24. Quantitative analysis of hyperoxia exposed and infected mouse primary fibroblasts migration.....	82
Figure 4.25. <i>Acta2</i> gene expression in CCL-206 (A) and primary neonatal mouse lung fibroblasts (B) after hyperoxia exposure and MHV-68 infection	83
Figure 4.26. PDGF-R α protein expression (A) and <i>Pdgfra</i> gene expression (B) in primary neonatal mouse lung fibroblasts after hyperoxia exposure and MHV-68 infection.....	84
Figure 4.27. <i>Vegf</i> gene expression in CCL-206 cells (A) and primary neonatal mouse lung fibroblasts (B) after hyperoxia exposure and MHV-68 infection	85
Figure 4.28. Recombinant MHV-68 expressing GFP infects primary neonatal mouse lung fibroblasts	86
Figure 4.29. MHV-68 replication in primary neonatal mouse lung fibroblasts after TGF β treatment.....	87
Figure 4.30. MHV-68 infection or TGF β treatment did not change or increase metabolic activity in the primary neonatal mouse lung fibroblasts	88
Figure 4.31. Annexin V binding after MHV-68 infection and TGF β treatment of primary neonatal mouse lung fibroblasts	90
Figure 4.32. Necrosis after MHV-68 infection and TGF β treatment of primary neonatal mouse lung fibroblasts	91
Figure 4.33. A wound healing “scratch” assay. Primary neonatal mouse lung fibroblasts	92
Figure 4.34. A mouse model of hyperoxia exposure and subsequent MHV-68 infection	94
Figure 4.35. MHV-68 titer in the “right lung lobe” lysates (A, C, E) and viral genomic load in the spleen (B, D, F)	95
Figure 4.36. H&E staining of lung sections	97
Figure 4.37. Assessment of inflammation in H&E-stained lung tissue sections.....	98
Figure 4.38. Alveolar size measured in adult mice after hyperoxia exposure and MHV-68 infection in childhood	100
Figure 4.39. RAC measurements in adult mice after hyperoxia exposure and MHV-68 infection in childhood	102
Figure 4.40. Septal wall thickness measured in adult mice after hyperoxia exposure and MHV-68 infection in childhood	104
Figure 4.41. Vascularization development in adult mice after MHV-68 infection and hyperoxia exposure in childhood	106
Figure 4.42. <i>Pdgfra</i> gene expression in adult mice in the double-hit model	108
Figure 4.43. <i>Pcna</i> gene expression in adult mice in the double-hit model.....	109
Figure 4.44. <i>Acta2</i> gene expression in adult mice in the double-hit model.....	111
Figure 4.45. <i>Hif1a</i> gene expression in adult mice in the double-hit model.....	112
Figure 4.46. <i>Wnt5a</i> gene expression in adult mice in the double-hit model	113

List of tables

Table 1. Comparison of "old" and "new" BPD	14
Table 2. Therapeutic activities to minimize lung injury in premature infants	17
Table 3. Assessment of RSV-related re-hospitalizations in preterm infants with and without BPD from selected references.....	23
Table 4 delineates the stages of lung development in animals, employed for the examination of lung morphogenesis and the modeling of bronchopulmonary dysplasia in comparison to humans.....	27

1. Introduction

1.1. Lung development

Lung formation is a highly regulated process implemented and controlled by multiple biochemical events and cellular mechanisms moderated through the interaction of epithelial and mesenchymal cells (Caldeira I. et al., 2021). The primary function of the lung is to enrich our blood with oxygen from the air through specialized structures called *alveoli* (Weibel, E. R., 2016). Alveoli are hollow, elastic sphere-shaped cavities in the lung. The alveolar *septum* is a particular structure that separates the alveoli from each other and contains the pulmonary capillaries responsible for gas exchange (Ochs M. et al., 2020). Each alveolus consists of three types of cells:

- type 1 pneumocytes: 70% of the internal surface of each alveolus, promote gas exchange, and stimulate type 2 cells to secrete surfactant in response to alveolar stretch;
- type 2 pneumocytes: produce and secrete *pulmonary surfactant* (the unique substance that reduces surface tension, preventing alveolar collapse), and play an important role as stem cells;
- alveolar macrophages: an essential role in our immune system (Michael Kasper and Kathrin Barth, 2017).

Fibroblasts and endothelial cells are also part of the alveolar unit. In humans and some mammals, the development of the lung is a continuing process from the very beginning of a new life (progress of fertilized ovum to an embryo) and for several years after birth (**Figure 1.1.**).

The first stage, called *embryonic*, starts with the formation of right and left lung buds. These lung buds subsequently divide to form an analog for the main bronchi (Sana Rehman and Dhouha Bacha, 2021). Later in the same stage, the trachea and larynx develop, and the bronchi continue to subdivide in exceptional patterns depending on the plane along which branching occurs. These patterns are called "domain branching," "planar branching," "orthogonal bifurcation" (Asima Hameed, Rizwan UI-haq, et al., 2013).

The next stage, *pseudoglandular*, is known to develop the bronchial tree; bronchial buds undergo comprehensive branching morphogenesis to form the first generation of the respiratory tree. In addition, terminal bronchioles, arterial system, cartilage, and smooth muscle develop at the end of this stage. The third stage, *canalicular*, is characterized by intensive angiogenesis and is responsible for capillary network formation. Here, the blood-air barrier starts to form, allowing some respiration. Children born at this stage could survive if provided with appropriate care (extremely preterm infants).

At the *saccular* stage, the gas-exchange surface area of the lungs grows, saccules (terminal sacs) develop, and pulmonary surfactant production begins. However, surfactant production is insufficient to avoid lung collapse and closure, and infants still require intensive care. The last stage, *alveolar*, lasts from 32 weeks through the whole life (Rehman S. and Bacha D., Embryology, Pulmonary, NCBI Bookshelf, 2022) and is characterized by the increased number and size of alveoli, capillaries, and continued lung maturation.

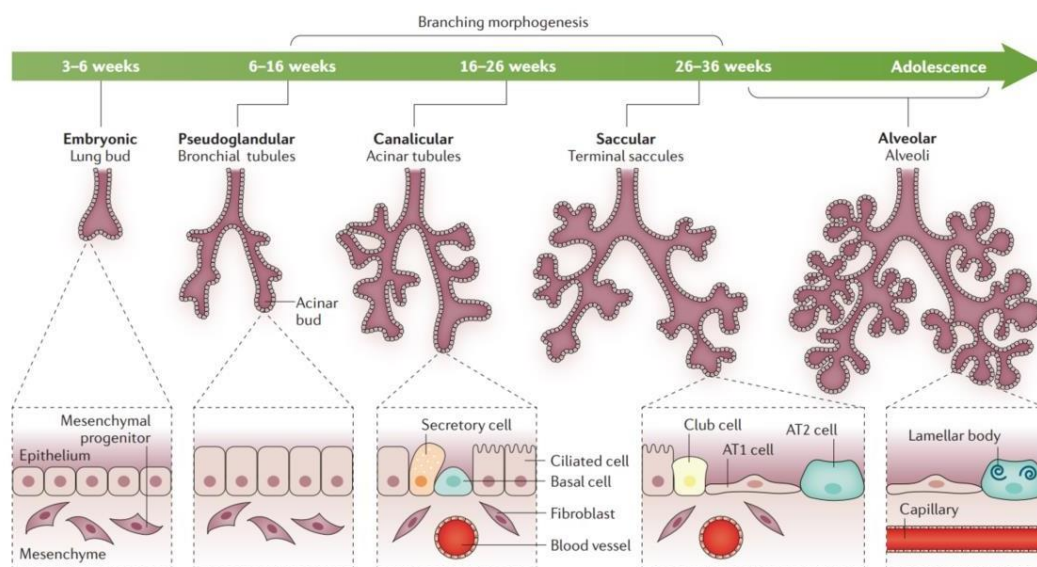


Figure 1.1. Lung developmental stages in humans.

This figure was published in Thébaud B, Goss KN, Laughon M, Whitsett JA, Abman SH, Steinhorn RH, Aschner JL, Davis PG, McGrath-Morrow SA, Soll RF, Jobe AH. Bronchopulmonary dysplasia. Nat Rev Dis Primers. 2019 Nov 14;5(1):78. doi: 10.1038/s41572-019-0127-7. PMID: 31727986; PMCID: PMC6986462.

Many biological processes and networks of signaling pathways ultimately control lung patterning, growth, and differentiation. For instance, Fibroblast Growth Factor (FGF), Transforming Growth Factor β (TGF β), Wingless-related Integration Site (WNT), (Caldeira, I., 2021). Nkx2.1 expression in endodermal

cells indicates the beginning of the lung specification in the embryonic stage (Ines Caldeira et al., 2021). Specifying Nkx2.1 respiratory endoderm progenitors during lung growth requires a Wnt/ β -catenin signaling pathway active work (Michael Herriges and Edward E. Morrisey, 2014). Wnt signaling pathways depend on Bmp signaling activity, which disrupts lung architecture (Sountoulidis, A. et al. 2012). TGF- β pathway is crucial for lung alveolarization and branching morphogenesis (Saito, A et al. 2018). Its upregulation and downregulation cause different respiratory diseases such as bronchial asthma, pulmonary fibrosis, and emphysema.

1.2. Prematurely born infants

In the modern world, the progression of neonatal intensive care and technological advancements has led to a rise in the population of infants born prematurely (Lammertink F et al., 2021). As a result, approximately 15 million babies per year are born too early, more than 1 in 10. Furthermore, it was reported in 2018 that complications arising from preterm birth stand as the primary contributor to mortality in children below the age of 5 years. (Li Liu et al., 2016).

The World Health Organization (WHO) divides prematurely born neonates into the following groups:

- preterm (birth at less than 37 weeks);
- moderate to late preterm (birth at 32-36 completed weeks of gestation);
- very preterm (28 to 32 weeks);
- extremely preterm (less than 28 weeks)).

Prematurely born babies are usually at a greater risk of health problems than full-term newborns; some health problems can develop into chronic forms and remain with the patient for life. Generally, the immune system and the structure and physiology of newborn organs are not complete, and babies require additional treatment and lifelong health validation (Richard E. Behrman and Adrienne Stith Butler, 2007). The consequences of preterm birth include neurological damage, cardiac dysfunction, impaired renal development, and chronic lung diseases, which may be characterized as an early childhood "asthma phenotype" or bronchopulmonary "phenotype" etc. (Alexander Humberg et al., 2020).

The usual respiratory outcomes from premature delivery are listed below.

1. *Neonatal respiratory distress syndrome* is also known as surfactant deficiency lung disease. The name comes from airway epithelial cells type I (responsible for gas exchange) and II (surfactant production) that are not fully differentiated from the mesenchyme in the immature lungs. As a result, many neonates require additional mechanical ventilation to force their lungs to breathe (Carolyn S Calfee et al., 2019).
2. Several respiratory diseases are known by the common name *pulmonary vascular disease*. They are all characterized by poorly developed blood vessels and high blood pressure in the pulmonary arteries or veins. Impaired pulmonary circulation is an outcome of patients with bronchopulmonary dysplasia (Peter M. Mourania and Steven H. Abmanb, 2013).
3. Impaired or aberrant *alveolar development* leads to a reduced surface area for gas exchange and obstructed breathing in adulthood.
4. According to the latest research studies, extremely preterm birth can increase asthma risk in grown neonates (Kristina Sundquist et al., 2011).
5. Extremely preterm delivery causes the risk of having lung function below the lower limit of normal (Per Thunqvist et al., 2017).
6. *Bronchopulmonary dysplasia* is one of the most common increases of morbidity and mortality in preterm infants (Sahni M., Mowes AK., 2022).

1.3. Bronchopulmonary dysplasia

In the last decades, neonatal care efficacy has increased leading to a higher survival rate of prematurely delivered babies. However, immature babies require additional care, such as oxygen therapy and/or mechanical ventilation, to survive. Bronchopulmonary dysplasia (BPD) is a chronic lung disease that most commonly affects preterm infants who receive respiratory support with mechanical ventilation and/or oxygen-rich gas (Cindy T. McEvoy and Judy L. Aschner, 2015). BPD was first described in 1967 by Northway et al. Back then, the cause of BPD was linked to the concept of "oxygen, pressure, and time (gestational age)". Researchers observed histopathological changes in lung

structure, nonhomogeneous airways, disruption of the pulmonary system, and relatively immature lungs (Jacqueline J. Coalson, 2006).

With improvements in mechanical ventilation strategies (f. i., the use of non-invasive ventilation), the introduction of exogenous surfactant replacement therapy, the use of antenatal steroids for mothers in their last weeks of pregnancy, and better control of oxygen therapy, the BPD morphological signs also changed. Nowadays, scientists and doctors distinguish between "old" BPD and "new" BPD (Fabio Mosca, Mariarosa Colnaghi, and Monica Fumagalli, 2011).

Table 1. Comparison of "old" and "new" BPD.

Old BPD	New BPD
Larger preterm infants	Extremely premature infants
High ventilation and oxygen needs	Modest ventilation and oxygen needs
Severe large airway injury	Minimal large airway disease
Interstitial and alveolar edema	Arrested alveolarization
Extensive small airway disease with alternating areas of overinflation and fibrosis	Minimal small airway disease with less inflammation and fibrosis
Pulmonary artery muscularization	Fewer and abnormal pulmonary arteries

The table was adapted from Cerny, Laura & Torday, John & Rehan, and Virender, 2008, Prevention and Treatment of Bronchopulmonary Dysplasia: Contemporary Status and Future Outlook. Lung. 186. 75-89.

"Old" BPD was described by a general definition of "abnormal pulmonary findings" (Shennan, A. T. et al., 1988). The description "old" is based on lung injury from oxygen therapy and mechanical ventilation. Although the degree of prematurity was relatively mild, the mortality rate of prematurely delivered babies was more than 50%. The mean gestational age of the survivors was approximately 34 weeks. Better care resulted in smaller (lower gestational age) babies having better chances of survival, leading to increased BPD incidence.

"New" BPD is characterized by early developmental arrest and lung disorder, simplified enlarged alveolar structure, dysmorphic capillary configuration, variable interstitial cellularity, fibroproliferation, and extracellular matrix

remodeling (Hilgendorff & O'Reilly, 2015; Sucre et al., 2021; Niedermaier & Hilgendorff, 2015; Thébaud et al., 2019).

The architecture of the alveoli and peripheral lung sacculus is important for respiration and gas exchange. Delivery at an early gestational age is followed by incomplete morphogenesis and alveolar differentiation. Pathologies in the airways that occur in patients with BPD suggest impaired angiogenesis, early disruption of pulmonary vascular growth, and endothelial dysfunction. This may be the reason for the simplified alveolarization (Lignelli, E. et al, 2019).

The alveolar walls, specifically the primary septa, are composed of endothelial cells and various interstitial cell types, including fibroblasts that have their origin in the lung mesoderm (Rodríguez-Castillo J. A. et al., 2018). On the tip of the septa, myofibroblasts expressing α -smooth muscle actin (α SMA) emerge, leading to heightened expression of extracellular matrix (ECM) components like elastin, and subsequent deposition of elastin by fibroblasts takes place (Mižíková, I., Morty, R. E., 2015). The pathological changes in alveolar structure are believed to be based on changed growth factor signaling, i.e., transforming growth factor β (TGF- β), vascular endothelial growth factor A (VEGF-A), platelet-derived growth factor receptor α (PDGF-R α), and others (Hilgendorff & O'Reilly, 2015; Oak & Hilgendorff, 2017; Oak et al., 2017) (**Figure 1.2.**). One of the secondary septation features is the deposition of ECM components and the presence of alveolar myofibroblasts. PDGF-A and its receptor PDGF-R α signaling are required to form the pulmonary alveolar septa walls. The ligand PDGF-A is produced by epithelial cells and works via the respective receptor PDGF-R α , expressed by mesenchymal cells (McGowan, S. E. et al., 2008). Animal experiments studying BPD demonstrated a strong dependence of lung formation on PDGF-R α expression (Gouveia, L. et al., 2018). Studies have shown that *Pdgfa*^{-/-} mouse lungs have enlarged alveoli without secondary septation.

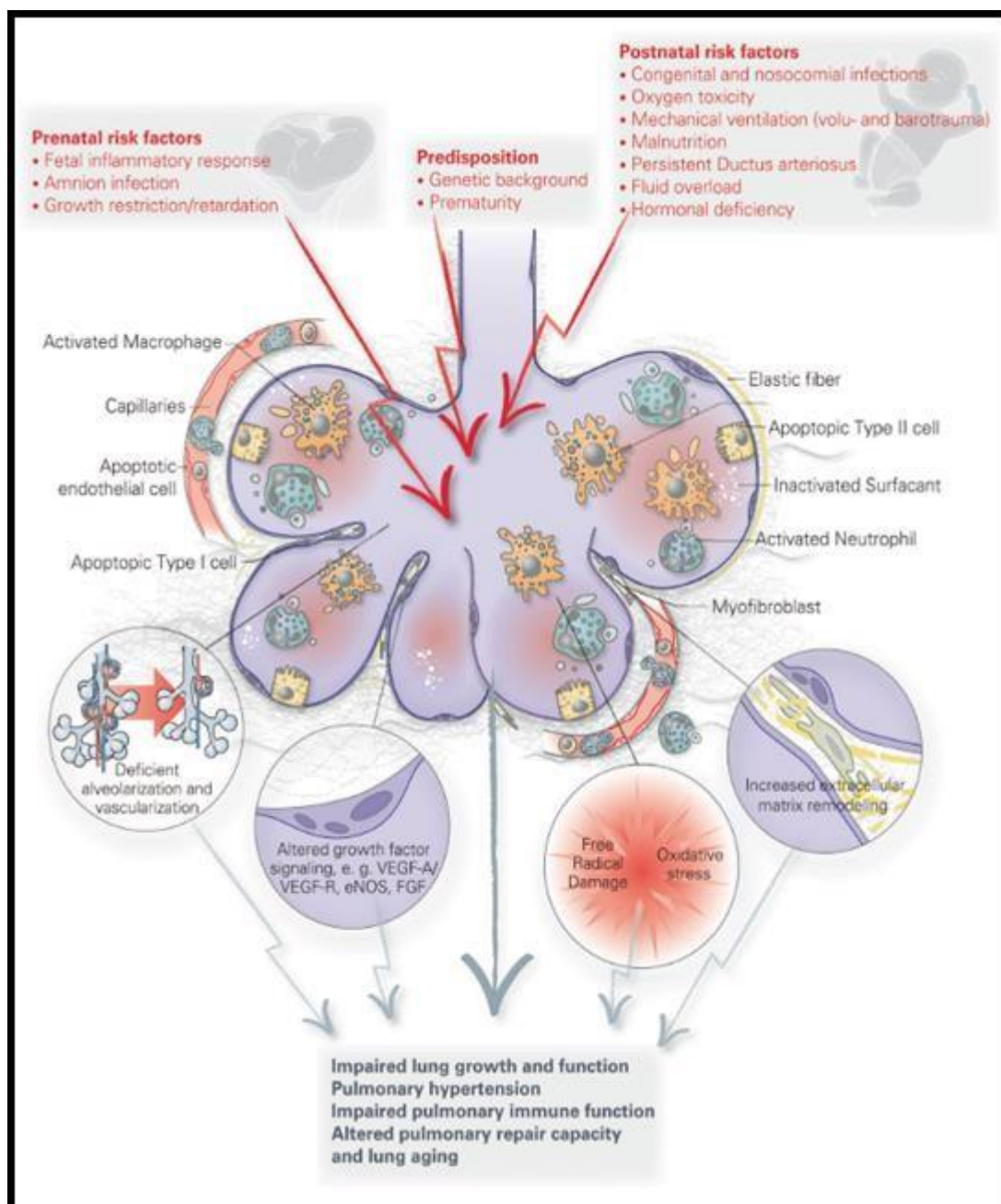


Figure 1.2. Processes involved in the pathophysiology of bronchopulmonary dysplasia (BPD).

This figure was published in Hilgendorff & O'Reilly. Bronchopulmonary dysplasia early changes are leading to long-term consequences. *Front Med (Lausanne)*. 2015 12; 2:2 (Hilgendorff & O'Reilly, 2015).

The focus of reducing BPD incidence is avoiding or minimizing long-term lung injury. For example, strategies such as choosing non-invasive respiratory support at birth could decrease the risk of BPD development (Committee on Fetus and Newborn; American Academy of Pediatrics, 2013). One of the best-evaluated treatments for BPD risk reduction is treatment with respiratory stimulants. Furthermore, a noteworthy progression in neonatal care involves the

administration of antenatal corticosteroids, a measure that diminishes mortality rates and lowers the risks of respiratory distress syndrome, intraventricular hemorrhage, and necrotizing enterocolitis. However, it does not reduce BPD incidences (Roberts, D. et al., 2017). **Table 2** demonstrates commonly used methods to minimize lung damage in preterm neonates.

Table 2. Therapeutic activities to minimize lung injury in premature infants

Intervention	Rationale	Level of evidence	Clinical implications
Caffeine	Reduced time on a ventilator <u>leading to less lung damage</u>	High quality: large RCT with long-term follow-up	Recommended for use in extremely preterm infants at the doses used in the CAP trial
Ventilation (conventional, high-frequency oscillation or jet ventilation)	Volutrauma is an important pathophysiological mechanism	Moderate quality: despite many RCTs, evidence of a substantial benefit of one mode is lacking	BPD rates remain high in all trials, suggesting that establishing and maintaining skills with a chosen mode may be the most important factor
Less-invasive surfactant therapy	Avoids the risks of Endotracheal intubation	Low quality: small RCTs, imprecise estimates of safety and efficacy	Very promising, but more <u>research required</u>
Vitamin A	Low levels seen in preterm infants; vitamin A required for normal lung growth	Moderate quality: meta-analysis suggests a small reduction in rates of death or BPD	Depends on local incidence of BPD; trade-off between the modest reduction in BPD and acceptability of intramuscular treatment
Targeting lower oxygen saturation levels throughout NICU stay	Avoidance of high oxygen levels may reduce BPD	High quality: individual patient data meta-analysis of five high quality RCTs	Targeting higher oxygen saturations (91–95%) improves survival rates without increasing risk of BPD
Dexamethasone	Reduced inflammation allowing earlier extubation	Moderate quality: meta-analyses and meta-	Low-dose, short courses that are useful for ventilated

		regression of numerous small trials	infants at highest risk of BPD
Hydrocortisone	Avoids adverse neurodevelopmental effects of dexamethasone	Moderate quality: small RCTs, imprecise estimates of safety and efficacy	Promising, but more research into neurodevelopmental outcomes is required
With surfactant	Better distribution of steroids and reduced systemic effects	Low quality: small RCTs, imprecise estimates of safety and efficacy	Very promising, but more research required

Table adapted from (Thébaud et al., 2019).

While effective treatment approaches have markedly enhanced the prognosis for individuals confronting BPD, it is essential to investigate the root causes and origins of underlying injuries to achieve a comprehensive understanding of the enduring challenges. An exacerbated inflammatory response commonly triggers the initial injury that can lead to BPD. All infants require breast milk to get maternally transferred antibodies. Also, they depend on the innate immune system, the first line of defense and protection against intruding pathogens, which gradually develops after birth. However, preterm infants' defenses against pathogens are severely changed (Melville J.M. et al., 2013).

In immature lungs, a hyporesponsive (tolerant) state can occur because the immune system becomes too active because of the misinterpretation of perinatal infection, leading to long-lasting changes in the immune response. This is caused by the excess production of inflammatory substances. At the same time, oxygen toxicity and mechanical ventilation have also been associated with the increased production of pro-inflammatory cytokines leading to sustained, systematic inflammation, which can distort future immune responses (Melville J.M. et al., 2013).

Several research studies investigate the impact of inhibitors targeting inflammatory mediators, receptors, and signaling pathways on the onset of BPD

in mice, rats, and rabbits (Surate Solaligue D. E. et al., 2017). These inquiries have demonstrated that subjecting newborn mice to hyperoxia, followed by recovery in room air, can create a predisposition to respiratory virus infection (O'Reilly, M. et al., 2012). Consequently, exposure to hyperoxia during the neonatal period might contribute to increased susceptibility to viral infections later in life.

1.4. Risk factors of BPD

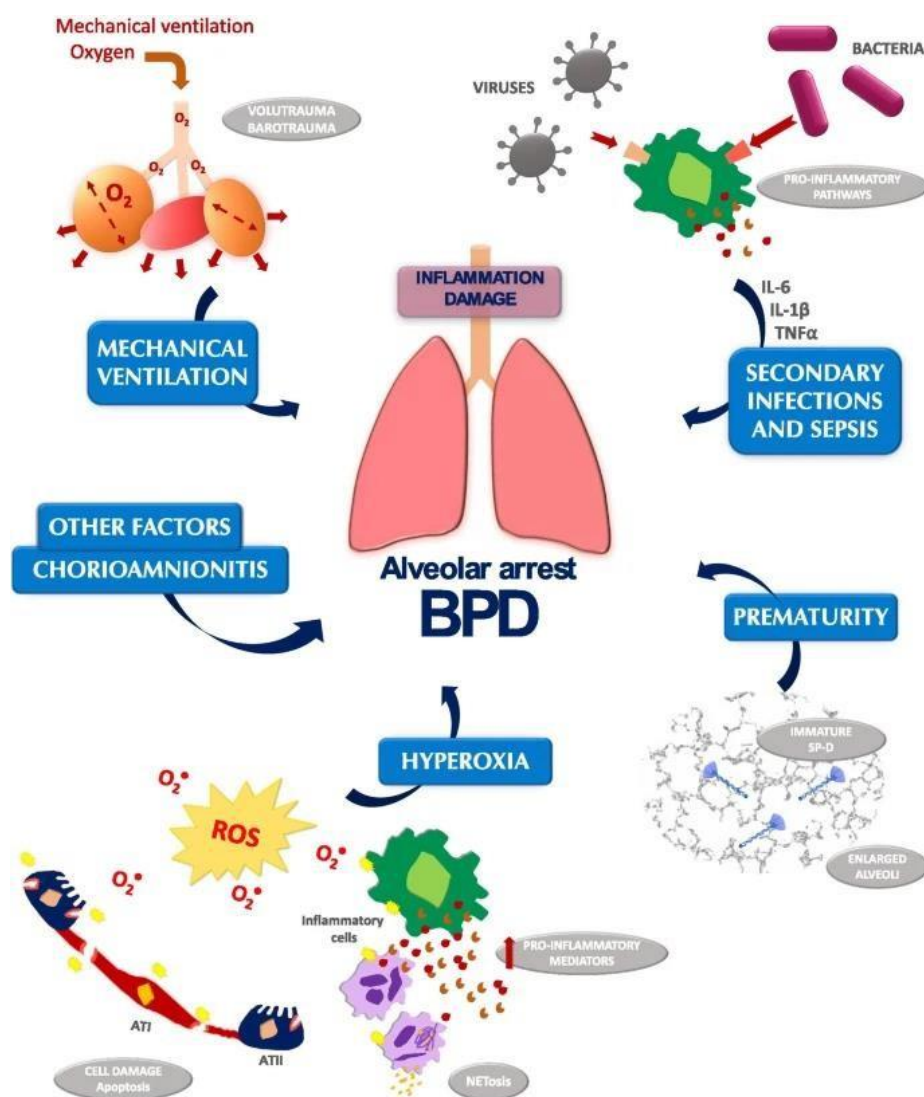


Figure 1.3. Factors that contribute to alveolar arrest in BPD.

The figure was published in Arroyo, R., Kingma, P.S. Surfactant protein D, and bronchopulmonary dysplasia: a new way to approach an old problem. *Respir Res* 22, 141 (2021).

- Chorioamnionitis is a significant risk factor for very premature births. However, evaluating its association with BPD is challenging because of the varying diagnostic criteria. Moreover, chorioamnionitis can disrupt

typical lung development and growth, potentially influencing the onset of BPD (Been, J. V. and Zimmermann, L. J. I, 2009).

- Fetal growth restriction, which is characterized by a birth weight below the median, is linked to a higher likelihood of BPD in preterm babies (Bose, C. et al, 2009).
- Mechanical ventilation involves the application of positive pressure, which can result in lung injury caused by the ventilator itself (**Figure 1.3**). With the introduction of surfactant therapy, a significant number of extremely premature infants have required mandatory mechanical ventilation after receiving surfactant replacement treatment (Doyle, L. W. et al, 2017).
- In many cases, infants are first exposed to extra oxygen right after birth, often in the delivery room. This additional oxygen is considered a possible threat to the developing lungs and brain (Carlo, W. A. et al, 2010). Infants needing high levels of oxygen may already have issues with gas exchange at the alveolar level because of their illness, but oxygen can also cause damage to capillary, endothelial, and alveolar membranes through oxidative injury (**Figure 1.3**).
- Sepsis and widespread inflammatory reactions increase BPD risk in preterm infants (**Figure 1.3**). Various microorganisms, such as *Ureaplasma urealyticum*, cytomegalovirus, and adenovirus have been linked to BPD development. Although the precise contribution of these pathogens to BPD remains uncertain, they are believed to be connected to the overall inflammatory response within the body.

A majority of individuals with pulmonary conditions exhibit heightened susceptibility to respiratory infections, as certain viral infections have the potential to exacerbate the progression of these diseases (Britto, C. L. et al, 2016). It has been suggested that respiratory viruses contribute meaningfully to the development of chronic obstructive pulmonary disease (COPD) (Mallia, P. et al., 2007, Wedzicha, J.A., 2004). Those viruses include rhinovirus, influenza, adenovirus, metapneumovirus, coronavirus, and respiratory syncytial virus (RSV). Wheezing episodes resemble asthma manifestations linked to the organism's viral infections (Sigurs, N. et al, 2000).

Different viruses have the potential to induce localized respiratory tract illnesses through the expulsion of aerosols contained in mucus or saliva when an individual

coughs, sneezes, or talks. Preterm-born babies are more susceptible to viral or bacterial infections due to the innate and adaptive immune systems' developmental immaturity and problems with the functional interaction between those two systems (Townsi, N., et al., 2018). The immune systems of preterm infants produce fewer monocytes and neutrophils, and these cells have an altered ability to kill pathogens. The association between immaturity, prenatal circumstances, and postnatal exposure oxygen toxicity is correlated with an imbalance in pro- and anti-inflammatory regulatory networks. Under these circumstances, the release of cytokines, protease activity, and prolonged presence of innate immune cells in the lung contribute to pathological processes, thereby contributing to lung injury (Heydarian, M. et al, 2022). Also, a lower production of cytokines was described, thus, the antiviral defense is defective compared to term infants (Jacqueline M. Melville and Timothy J. M. Moss, 2013). Commonly used antenatal corticosteroid treatment is supposed to prevent newborn respiratory disease, at the same moment it has immunosuppressive effects, suppressing lymphocyte proliferation and cytokine production and thereby increasing the risk of infection.

The risk of severe respiratory syncytal virus – acute lower respiratory tract infection, defined by the measured hospitalization risk, intensive care unit admission, need for oxygen supplementation, was higher among BPD patients compared with non-BPD (Chaw, P. S. et al, 2019). The coexistence of primary structural and functional issues characteristic of BPD with intercurrent respiratory infections (**Figure 1.4.**) may be encouraging the conditions for morbidity and mortality in infants who initially exhibited positive developmental progress (Taylor, J. B. et al, 2013).

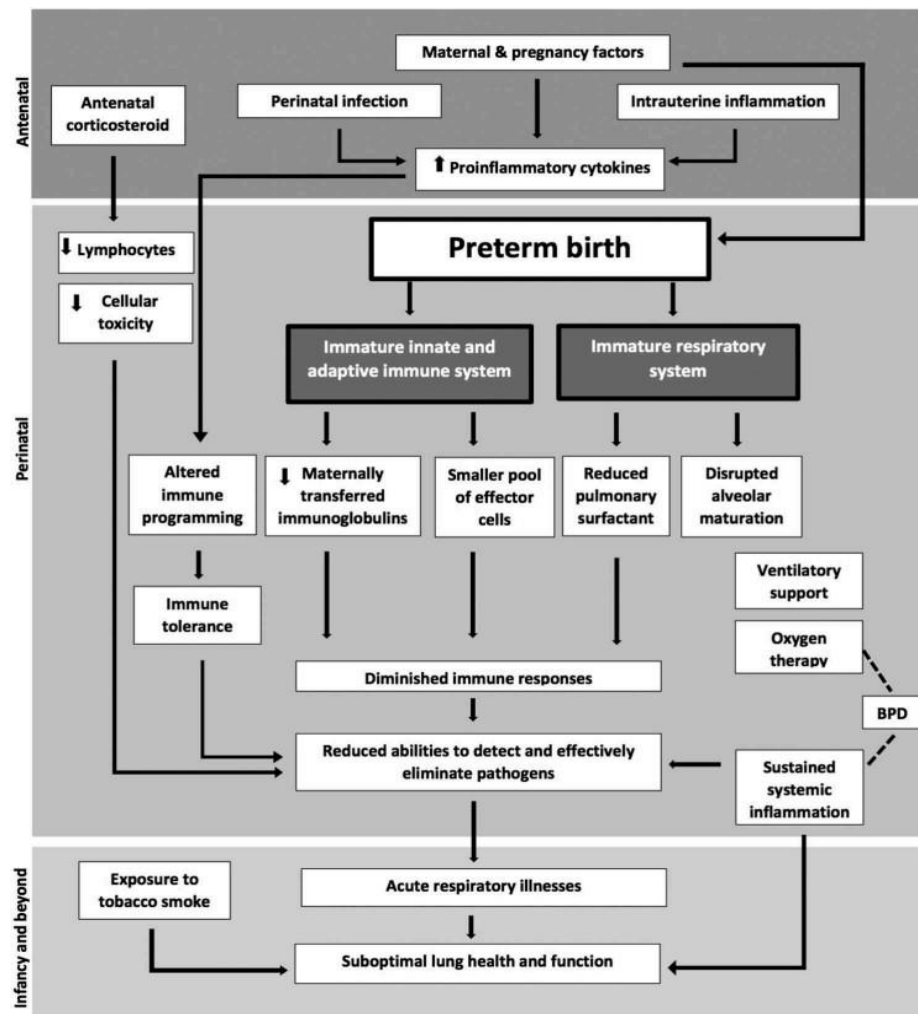


Figure 1.4. A schematic diagram showing that pathways associated with preterm birth may result in diminished immune responses and increased susceptibility to acute respiratory infection.

The figure was published in Nada Townsi, Ingrid A. Laing, Graham L. Hall & Shannon J. Simpson, The impact of respiratory viruses on lung health after preterm birth, *European Clinical Respiratory Journal* (2018).

Preterm babies have a three times higher risk of re-hospitalization with a respiratory infection during the first year of life than term infants (Pramana I. A. et al., 2011). Approximately 1% of children with RSV require hospitalization, whereas infected preterm babies' hospitalization ranges from 10 to 19% during the first year. About 50 to 73% of preterm babies with BPD were re-hospitalized at least once with an acute respiratory infection during the first three years of life, which is approximately two times bigger numbers than the cases of re-hospitalization among those without BPD (Smith VC, Zupancic JA, McCormick, et al., 2004). Common viral infections, such as RSV or influenza, can trigger the

risk of hospitalization in patients with BPD because of complicated respiratory episodes (Thébaud et al., 2019).

Influenza A infection is one of the most investigated viruses in experimental BPD development studies. Neonatal mice are exposed to 40 – 85% oxygen and infected with influenza A virus (IAV) infection. Those investigations revealed decreased pulmonary function in infected mice and stiffer lung structure after double-hit exposure – oxygen and virus infection (Dylag, A. M. et al., 2021).

Table 3 provides a summary of re-hospitalization rates reported in various populations of premature infants as documented in selected studies.

Table 3. Assessment of RSV-related re-hospitalizations in preterm infants with and without BPD from selected references.

Population	Number of patients	Study years	RSV re-hospitalization rate (%)
BPD	30	1985-1986	59.0
BPD	124	1992-1994	14.5
BPD	149	1994-1995	17.4
BPD	53	1998-1999	7.4
BPD	53	1998-1999	15.0
BPD	108	1999-2000	5.6
PT12	584	1998-1999	13.4
PT12	1029	1992-1996	11.2
PT12	1249	1994-1999	6.6
PT12	717	1998-2000	5.2
PT6	510	1994-1995	8.1
PT6	740	1996-1997	8.1
PT6	801	2001-2003	4.5

RSV: respiratory syncytial virus; BPD: bronchopulmonary dysplasia; PT: preterm (infants); PT12: <12 months of chronological age; PT6: <6 months of chronological age.

Table adapted from (Resch B. et al., 2016).

One of the most worldwide spread and common human virus groups is the Herpesvirus family (Sharma, B. et al., 2016). Among the over 100 recognized herpesviruses, only eight specifically target humans. These include herpes

simplex virus types 1 and 2, varicella-zoster virus, cytomegalovirus, Epstein-Barr virus, human herpesvirus 6 (variants A and B), human herpesvirus 7, and Kaposi's sarcoma virus, also known as human herpesvirus 8 (Whitley, R. J., *Medical Microbiology*, 4th edition). The Herpesvirus family encompasses significant human pathogenic strains that lead to various incurable diseases. Notably, the presence of Epstein–Barr virus DNA is more prevalent in the respiratory tract of patients with chronic obstructive pulmonary disease (COPD) compared to unaffected smokers. This viral DNA is detectable in both exacerbation and stable phases, indicating a persistent infection. Notably, individuals who smoke but do not develop COPD seldom exhibit Epstein–Barr virus in their sputum (McManus, T. E. et al, 2008).

BPD patients demonstrated the presence of fibrotic tissue within the lung parenchyma, contributing to the restructuring of lung architecture. The development of BPD follows a complex pathway, marked by progressive lung injury due to prolonged exposure to hyperoxia within the context of existing prenatal determinants. In this intricate process, dysregulated immune responses and faulty tissue repair mechanisms manifest in preterm infants, ultimately resulting in compromised alveolarization and impaired vascular development (Sahni, M. and Bhandari, V., 2021). The occurrence of pulmonary hypertension (PH) in individuals with idiopathic pulmonary fibrosis (IPF) could potentially be influenced by herpesviral infections, as suggested by a body of evidence (Calabrese, F. et al, 2013; Duckworth, A. et al, 2021). The increased susceptibility to idiopathic pulmonary fibrosis is prominently linked to the existence of persistent or chronic viral infections, particularly Epstein–Barr virus (EBV), cytomegalovirus (CMV), human herpesvirus-7 (HHV-7), and human herpesvirus-8 (HHV-8). It is essential to emphasize that this elevated risk is particularly linked to chronic viral infections and not acute infections. A fundamental characteristic of all known herpesviruses is the establishment of persistent infections in the natural hosts, enduring throughout the host's lifetime and remaining resistant to complete clearance. These findings collectively suggest that persistent viral infections may constitute a significant risk factor in the etiology of lung fibrosis (Sheng, G. et al, 2020).

1.5. MHV-68

A significant challenge in investigating human gammaherpesviruses stems from the absence of a reliable small animal model suitable for exploring fundamental aspects of viral pathogenesis. This difficulty arises due to the limited host tropism exhibited by both Epstein–Barr virus and Kaposi's sarcoma-associated herpesvirus. Murine gammaherpesvirus 68 (MHV-68) is a naturally occurring virus genetically related to the human gammaherpesviruses, Epstein-Barr virus, and Kaposi sarcoma-associated herpesvirus. MHV68 efficiently infects mice, initiating a persistent infection that is sustained throughout the lifespan of the host (Barton, E. et al, 2011). Since bronchopulmonary dysplasia (BPD) persists into adulthood in preterm babies, it is essential to study virus infections that can establish lifelong conditions in the host organism. Following intranasal infection of mice, MHV-68 undergoes acute infection in the lungs and nasal epithelium. It establishes latency, a nonproductive, silent condition characterized by minimal viral gene expression and maintenance of the viral genome in the spleen and blood cells (Weed, D. J., and Damania, B., 2019).

MHV-68 infection in mice manifests in diverse pathologies resembling Epstein-Barr virus-associated diseases. Notably, this infection induces elevated levels of oxidative stress and reactive oxygen species in cultured murine fibroblasts, as demonstrated by Bortz et al. in 2018. Furthermore, MHV-68 infection in mice serves as a valuable model for investigating macrophage dynamics and the induction of fibrosis, as highlighted by the research conducted by Gangadharan et al. in 2008. Moreover, mice subjected to chronic MHV-68 infection exhibit conditions akin to those seen in individuals infected with EBV (Dong, J. et al., 2017). Additionally, MHV-68 infection triggers systemic inflammation, exacerbates autoimmune encephalomyelitis, and impacts the development of various other pathologies (Peacock, J. W. et al., 2003).

Ultimately, MHV-68 is a natural pathogen of murid rodents, very well-characterized, and can easily infect very young mice via intranasal inoculation (Kudelova, M., and Stibraniova, I., 2018). Given that BPD is a persistent and chronic condition, characterized by the hallmark feature of fibrosis, the use of MHV-68 as a mouse model becomes particularly pertinent. MHV-68, owing to its capacity to establish latency within the host organism and induce fibrotic processes, mirrors the characteristics of human gammaherpesvirus infection.

Consequently, the usage of MHV-68 infection as a model system provides a valuable opportunity to investigate the impact of viral infections on the developmental trajectory of neonatal lungs and the manifestation of BPD.

1.6. Experimental *in vitro* BPD models

In the examination of BPD, *in vitro* experimental models play a pivotal role, enabling researchers to analyze distinct cellular and molecular mechanisms integral to the disease's pathogenesis. One of the key factors contributing to BPD development is exposure to elevated concentrations of oxygen. The precise oxygen concentration employed to induce BPD in *in vitro* experiments may differ depending on the study's specific objectives and the types of cells under investigation. However, researchers commonly use elevated levels of oxygen, often referred to as hyperoxia, to simulate the conditions observed in premature infants receiving oxygen therapy. The oxygen concentration employed in these experiments is typically higher than the atmospheric level (normoxia), which is around 21%. In many *in vitro* BPD models, researchers expose cells to levels of oxygen, ranging from 40% to 95%, depending on the specific experimental design.

Primary human lung fibroblasts and precision-cut lung slices derived from mouse pups (P4 – P7) underwent a 96-hour exposure to 70% oxygen, revealing a suppression of Wnt5a signaling associated with the BPD phenotype (Sucre, J. M. S. et al, 2020). Additionally, You, K. et al. (2019) explored the effects of moderate hyperoxia on senescence and autophagy in human primary fetal lung fibroblasts, subjecting them to 40% oxygen for 7 days. In a separate investigation, primary type II alveolar cells sourced from premature rats were exposed to 95% oxygen for 24 hours, resulting in an observed upregulation of anti-apoptotic factors (Wu, D. et al., 2018).

In conclusion, *in vitro* models provide a valuable experimental model to minimize the reliance on animal experimentation while serving as an accessible platform for elucidating the molecular consequences of hyperoxia, a complex phenomenon central to conditions such as BPD. These studies contribute to a deeper understanding of the complex cellular responses under hyperoxic conditions.

1.7. Experimental *in vivo* BPD models

This research mainly focuses on elucidating alterations in lung structure during the saccular and alveolar stages of development. These stages encompass the formation and maturation of gas exchange regions in the lung, specifically involving changes in alveolar size and quantity. **Table 4** demonstrates a notable correlation between the latter two stages of human lung development and the mouse lung at postnatal days one to twenty-one. Consequently, it is recommended to precisely age mice between five to eight days, aligning with comparable lung developmental milestones in humans.

The lung development in mice at postnatal day five closely aligns with the growth status observed in human lungs at approximately week 36 of gestation. This alignment allows for the characterization of these mouse pups as models for prematurely born lungs. This precise age selection facilitates a meaningful comparison between murine lung development and the corresponding stages in human lung development.

Table 4 delineates the stages of lung development in animals, employed for the examination of lung morphogenesis and the modeling of bronchopulmonary dysplasia in comparison to humans.

Animal	Term	Embryonic	Pseudoglandular	Canalicular	Saccular	Alveolar
Mouse	20	E9.5–E12	E12–E16.5	E16.5–17.5	E17.5–P4	P4–P21
Rat	21–24	E11–E13	E13–E18.5	E18.5–E20	E21–P4	P4–P21
Rabbit	32	Up to E18	E21–E24	E24–E27	From E27	From E30
Human	280	Up to E42	E52–E112	E112–E168	From E168	From E252

Table adapted from (Surate Solaligue D. E. et al., 2017).

There are different ways to mimic BPD in mice and study the disease's consequences. The examination of animal models exhibits variability across species, oxygen concentration levels, exposure durations, and metrics employed to assess lung injury. Research findings spanning the years 2012 to 2015 documented 41 distinct oxygen exposure protocols employed to induce lung

damage in animal models. Specifically, exposing mice at postnatal day 1 (PN1) to 75% oxygen for a duration of 14 days has proven sufficient to induce alveolar simplification and septal thickening, resembling the lung pathology observed in premature infants with bronchopulmonary dysplasia (BPD) (Giusto, K. et al., 2021). Another study conducted by Nardiello, C. et al. involved exposing C57BL/6 mouse pups to 85% oxygen for a similar duration, employing design-based stereology for lung tissue analysis. This level of hyperoxia effectively replicated BPD features, leading to significant alveolar simplification.

However, it's noteworthy that while exposure to 85% oxygen successfully induced a BPD phenotype in mouse pups, it may not be clinically relevant. In light of this, Nardiello et al. recommend a reduction in oxygen concentration to 60% for evaluating interventions, especially if the intervention under consideration struggles to reverse the damage caused by 85% oxygen exposure. This approach aims to provide a more clear understanding of cellular changes under conditions that closely align with potential clinical applications.

Moreover, it is essential to tailor the oxygen concentrations and exposure durations to suit the clinical environment. Hence, it becomes imperative to utilize models that involve moderate hyperoxia concentrations ($FiO_2 < 0.5$) and shorter exposure durations (24 hours) to faithfully mirror the clinical context (Andresen & Saugstad, 2020; Torres-Cuevas et al., 2017; Thébaud et al., 2019; Askie et al., 2003; Tracy & Berkelhamer, 2019).

1.8. Mouse models of BPD combined with virus infection

Elevated oxygen concentrations over an extended period can induce a severe form of bronchopulmonary dysplasia (BPD) in mice, potentially complicating double-hit studies that involve virus infection. Nevertheless, certain investigations have employed high oxygen levels followed by viral infection in mice. As an illustration, a research conducted by O'Reilly, M. A. et al. in 2008 exposed newborn C57BL/6J mice to either room air or 100% oxygen from postnatal day 1 to day 4, followed by influenza A virus infection. The investigators suggested that hyperoxia not only interrupts neonatal lung development but also alters crucial innate immunoregulatory pathways, leading to intensified pathology and reduced resistance to respiratory viral infections—characteristics often observed in individuals with BPD. In contrast, recent investigations by O'Reilly, M. A. et al. in

2021 introduced a new low-dose hyperoxia mouse model (40% oxygen for 8 days; referred to as 40×8) followed by Influenza A infection. This model induces a temporary alteration in lung function that resolves over time, resulting in adult animals exposed to 40×8 being functionally indistinguishable from those in room air controls. The researchers proposed that this model more accurately mirrors the respiratory challenges observed in contemporary preterm infants after discharge from the neonatal intensive care unit (NICU) without a BPD diagnosis. The 40×8 hyperoxia model, when combined with virus infection, demonstrates an airway-specific phenotype at baseline and leads to increased respiratory challenges following infection.

1.9. Aim of the project

There is not so much known about the mutual influence of moderate hyperoxia exposure and gammaherpesvirus infection on the lung development of neonatal mice. This doctoral research aims to comprehensively investigate the impact of the murine gammaherpesvirus 68 (MHV-68) model, on the development of neonatal mouse lungs and its potential correlation with bronchopulmonary dysplasia (BPD). To address this knowledge gap, this study is focused on the investigations of the morphological changes in lungs, apoptosis and necrosis processes in neonatal primary mouse lung fibroblasts, and key developmental genes expression like *Pfgrα*, *Hif1a*, *Wnt5a*, etc.

This study will perform the following specific objectives:

1. Establishment of long-term *in vivo* experimental model: develop and optimize *in vitro* and *in vivo* experimental models that are conducive to long-term studies, ensuring the sustainability required for investigating life-long diseases influenced by gammaherpesvirus infection and BPD development in the mouse lungs and primary fibroblasts.
2. Characterization of viral infection and hyperoxia exposure influence on mouse neonatal lung development: thoroughly characterize the impact of MHV-68 on the morphological changes of neonatal mouse lungs, such as Radial Alveolar Count, septal thickness, alveoli number, vessels formation. This includes assessing cellular alterations and molecular responses over an extended period.
3. Investigation of sex-dependent changes in lungs and primary fibroblasts in response to double-hit model.

By achieving these objectives, this research will contribute valuable insights into the complicated interplay between gammaherpesviruses, lung development in neonatal mice, and the potential connection to bronchopulmonary dysplasia. The established models will serve as essential tools for studying life-long diseases, providing a foundation for future research and potential therapeutic interventions in this critical domain.

2. Materials.

2.1. Primary antibodies

<i>Antigen</i>	<i>Product number</i>	<i>Host Type</i>	<i>Application</i>	<i>Dilution</i>	<i>Manufacturer</i>
<i>p44/42 MAPK</i>	9102	Rabbit	WB	1:1000	Cell signaling
<i>B-Actin-HRP</i>	ab49900	Rabbit	WB	1:20000	Abcam
<i>PCNA</i>	ab29	Mouse	WB	1:1000	Abcam
<i>CD11b V450</i>	560455	Rat	FACS	1:100	BD Biosciences
<i>CD90.2 APC</i>	561974	Rat	FACS	1:100	BD Biosciences
<i>CD 105 PE</i>	130-102-548	Rat	FACS	1:100	Myltenyic Biotec

2.2. Secondary antibodies

<i>Antigen</i>	<i>Product number</i>	<i>Host Type</i>	<i>Application</i>	<i>Dilution</i>	<i>Manufacturer</i>
Anti-rabbit IgG-HRP	sc-2357	Mouse	WB	1:1000	Santa Cruz
m-IgGk BP-HRP	sc-516102	-	WB	1:1000	Santa Cruz

2.3. Primers

The primers employed for quantitative real-time polymerase chain reaction (qRT-PCR) were procured from Eurofins, a company located in Luxembourg.

<i>NCBI Gene Symbol</i>	<i>Organism</i>	<i>Forward sequence</i>	<i>Reverse sequence</i>
<i>Pdgfra</i>	Mouse	AGGTATGTATCCACAC ATGCGT	AGTTCCTGTTGGTTTCAT CTCG

<i>Pcna</i>	Mouse	TTTGAGGCACGCCTGA TCC	GGAGACGTGAGACGAGT CCAT
<i>Gapdh</i>	Mouse	AGGTCGGTGTGAACGG ATTTG	TGTAGACCATGTAGTTGA GGTCA
<i>Acta2</i>	Mouse	GTCCCAGACATCAGGG AGTAA	TCGGATACTTCAGCGTCA GGA
<i>Wnt5a</i>	Mouse	GACTCCGCAGCCCTGC TTTG	CCAATGGGCTTCTTCATG GCGAG
<i>HIF-1</i>	Mouse	TATAAACCTGGCAATGT CTCC	GATGCCTTAGCAGTGGT CGT
α -SMA	Mouse	GTGACTACTGCCGAGC GTG	ATAGGTGGTTTCGTGGAT GC
<i>VEGF</i>	Mouse	CAGGCTGCTCTAACGA TGAA	CAGGAATCCCAGAAACA ACC
<i>VE Cadherin</i>	Mouse	CTTCCAGCGACACTTC TACC	TTCCCTGCTTGGTTATTC GG
<i>Caspase 3</i>	Mouse	GAA TGT CAG CTC GCA ATG GTA C	AGT AGT CGC CTC TGA AGA AAC TAG
<i>L8</i>	Mouse	GATCCCTTTGGAGGTG GTA	CATCTCTTCGGATGGTG GA
<i>gB</i>	Mouse	GGCCCAAATTCAATTTG CCT	CCCTGGACAACCTCCTCAA GC

2.4. Cell culture

2.4.1. Cell lines

CCL-206 Mouse Neonatal Lung Fibroblasts (Mlg 2908)

BHK-21 Baby hamster kidney fibroblasts (ATCC CRL-1658)

MPF Mouse Primary Fibroblasts

2.4.2. Media formulations

Cell type	Culture Medium	Catalog Number	Manufacturer
CCL-206	DMEM F-12	11320033	Thermo Fischer Scientific
	20% FBS	P30-3702	Pan Biotech
	2 mM L-Glutamine	25030149	Gibco
	100 U/mL Penicillin/Streptomycin	15140122	Gibco

MPF	DMEM-1	11320033	Thermo Fischer Scientific
	10% FBS	P30-3702	Pan Biotech
	2 mM L-Glutamine	25030149	Gibco
	100 U/mL Penicillin/Streptomycin	15140122	Gibco
BHK-21	GMEM	11710035	Thermo Fischer Scientific
	100 U/mL Penicillin/Streptomycin	15140122	Gibco
	5% FBS	P30-3702	Pan Biotech
	5% tryptose phosphate broth	T8159	Sigma
	2 mM L-Glutamine	25030149	Gibco

2.4.3. Reagents and chemicals

Reagent	Manufacturer
Dithiothreitol (DTT)	AppliChem AppliChem, Darmstadt, Germany
DNase I	AppliChem AppliChem, Darmstadt, Germany
Ethanol	AppliChem AppliChem, Darmstadt, Germany
Methanol	AppliChem AppliChem, Darmstadt, Germany
Non-fat fried milk powder	AppliChem AppliChem, Darmstadt, Germany
Ripa buffer	Life Technologies, Darmstadt, Germany
NuPAGE® LDS Sample Buffer (4X)	Life Technologies, Darmstadt, Germany
NuPAGE® Reducing Agent (10X)	Life Technologies, Darmstadt, Germany
NuPAGE® 4-12% Bis-Tris gels	Life Technologies, Darmstadt, Germany
NuPAGE® 3-8% Tris-acetate gels	Life Technologies, Darmstadt, Germany
Nitrocellulose/Filter Paper, catalog #LC2006, Life Technologies	Life Technologies, Darmstadt, Germany
Eosin G-solution 1% in water	Carl Roth, Karlsruhe, Germany

0.05% trypsin-EDTA	Thermo Fisher Scientific, Schwerte, Germany
0.25% trypsin-EDTA	Thermo Fisher Scientific, Schwerte, Germany
Tween 20	Sigma-Aldrich, Taufkirchen, Germany
Dimethyl sulfoxide (DMSO)	Carl Roth, Karlsruhe, Germany
Desoxyribonucleotides mix (dNTPs)	Thermo Fisher Scientific, Germany
Fetal bovine serum (FBS, Sera Plus)	PAA, GE Healthcare
Complete® Mini without EDTA (Protease inhibitor)	Roche Diagnostics, Mannheim, Germany
Light Cycler 480 SybrGreen I Master Mix	Roche Diagnostics, Mannheim, Germany
Bovine serum albumin (BSA)	Sigma-Aldrich, Taufkirchen, Germany
Ponceau S solution	Sigma-Aldrich, Taufkirchen, Germany
Restore Plus Western Blot Stripping	Thermo Fisher Scientific, Schwerte, Germany
Methylcellulose	Sigma-Aldrich, Taufkirchen, Germany
Crystal Violet	Sigma-Aldrich, Taufkirchen, Germany

2.4.4. Buffer formulations

Buffer	Reagents
Laemmli loading buffer (6x)	SDS 12% (w/v) Glycerol (87%) 60% (v/v) Bromophenol blue 0.06% (w/v) Tris/HCl, pH 6.8 375 mM DTT 600 mM
RIPA (radio-immunoprecipitation assay) buffer	Tris-Cl pH 7.4 50 mM NaCl 150 mM NP40 1% (v/v) Na-deoxycholate 0.25% (v/v)

Transfer buffer (10x)	Tris/HCl 250 mM Glycine 1.92 M
TBS (Tris-buffered saline) (10x)	Tris/HCl pH 7.4 10 mM NaCl 150 mM
TBS-T (TBS with TWEEN®20)	TBS (10x) 10% (v/v) Tween®20 0.1% (v/v) Millipore-H ₂ O 89.99% (v/v)
PBST washing buffer	NaCl 137 mM KCl 2.7 mM Na ₂ HPO ₄ 10 mM KH ₂ PO ₄ 2 mM Tween-20 1 % (v/v)
1X BSA (Bovine Serum Albumin)	Bovine serum albumin-5g 20% Triton X-100-2.5ml 10X PBS-50ml
5% Milk Blocking Solution	5 gm Skim Milk powder/100ml 1X TBS-T
PBS (Phosphatate buffered saline) pH 7.4	NaCl 1.37 M KCl 27 mM Na ₂ HPO ₄ 100 mM KH ₂ PO ₄ 20 mM NaCl 1.37 M
4% PFA in PBS	37% Formaldehyde PBS

2.5. Kits

Kit	Catalog number	Manufacturer
Caspase-Glo® 3/7 Assay System	G8090	Promega
Pierce™ BCA Protein Assay Kit	23227	Thermo Fisher
QIAamp DNA Mini Kit	51304	Qiagen
CytoSelect 96-well Cell Migration Assay Kit	ab235673	Cell Biolabs
EZCell™ Cell Migration/Chemotaxis Assay Kit	K906-100	BioVision
RealTime-Glo™ Annexin V Apoptosis and Necrosis Assay	JA1011	Promega
NucleoSpin RNA plus kit	740955.50	Macherey Nagel
Applied Biosystems™ High-Capacity cDNA Reverse Transcription Kit	4368814	Thermo Fisher

2.6. Consumables

Consumable	Manufacturer
96-well imaging plates, Falcon®	Corning, Thermo Fisher Scientific, Schwerte, Germany
Cell culture dishes	Corning, Thermo Fisher Scientific, Schwerte, Germany
Cell culture multi-well plates	TPP Techno Plastic Producers, Trasadingen, Switzerland
Combitips advanced®	Eppendorf, Hamburg, Germany
Cryovials 1.5 ml	Greiner Bio-One, Frickenhausen, Germany

Falcon Tube (15 ml, 50 ml)	BD Bioscience, Heidelberg, Germany
Filter Tips	Biozym Scientific, Hessisch Oldendorf, Germany
Glas Pasteur pipettes	VWR International, Darmstadt, Germany
Measuring pipettes, sterile, single-use (5 ml, 10 ml, 25 ml, 50 ml)	VWR International, Darmstadt, Germany
Microscope slides	Thermo Fisher Scientific, Darmstadt, Germany
PCR plates, 96-well plate	Kisker Biotech, Steinfurt, Germany
Western Blot Running gels	Thermo Fisher Scientific, Darmstadt, Germany
Nitrocellulose 40 µm membranes	Thermo Fisher Scientific, Darmstadt, Germany
PVDF membrane	Merck Millipore, Darmstadt, Germany
Reaction tubes (0.5 ml, 1.5 ml, 2 ml)	Eppendorf, Hamburg, Germany
Sealing foils for PCR plates	Kisker Biotech, Steinfurt, Germany
Sterical cannulas	BD Biosciences, Heidelberg, Germany
Syringes	Neolab, Heidelberg, Germany
Tips	Eppendorf, Hamburg, Germany
white 96-well microplates	Berthold Technologies, Bad Wildbad, Germany

2.7. Laboratory equipment and software

Laboratory equipment	Manufacturer
-20°C freezer MediLine LGex 410	Liebherr, Biberach, Germany
-80°C freezer U570 HEF	New Brunswick, Hamburg, Germany

Cell culture workbench	Thermo Fisher Scientific, Darmstadt, Germany
Centrifuge MiniSpin plus	Eppendorf, Hamburg, Germany
Centrifuge Rotina 420R	Hettich, Tuttlingen, Germany
Centrifuge 5415D Digital	Eppendorf, Hamburg, Germany
Centrifuge 5417R	Eppendorf, Hamburg, Germany
Centrifuge with cooling, Micro200R	Hettich, Tuttlingen, Germany
Centrifuge Rotina 35 R	Hettich, Tuttlingen, Germany
CO2 Cell Incubator BBD6620	Thermo Fisher Scientific, Darmstadt, Germany
CO2 Cell incubator HERAcell 150	Thermo Fisher Scientific, Darmstadt, Germany
Confocal microscope LSM 710	Zeiss, Jena, Germany
Confocal microscope Telaval 31	Zeiss, Jena, Germany
Fisher Science Education™ 4-Way Microtube Racks	Thermo Fisher Scientific, Darmstadt, Germany
Fridge MediLine LKv 3912	Liebherr, Biberach, Germany
Fridge	Bosch, Weissach, Germany
Gel image system ChemiDoc XRS+	Biorad, Hercules, USA
GloMax® Explorer Multimode Microplate Reader	Promega, Madison, USA
Oxygen controller ProOx110, Biospherix	Parish, NY
Homogenizer FastPrep-24	MP Biomedicals, Eschwege, Germany
Light Cycler LC480II	Roche Diagnostic, Mannheim, Germany

Liquid nitrogen cell tank BioSafe 420SC	Cryotherm, Kirchen/Sieg, Germany
LSR II	BD Biosciences, NJ, USA
Magnetic Stirrer MR 3001	Heidolph Instruments, Schwabach, Germany
Multipette stream	Eppendorf, Hamburg, Germany
Nalgene® Freezing Container (Mr. Frosty)	Omnilab, Munich, Germany
Thermo Labtop Cooler 12 Places 5115-0012	Thermo Fisher Scientific, Darmstadt, Germany
NanoDrop	Thermo Fisher Scientific, Darmstadt, Germany
Plate centrifuge 5430	Eppendorf, Hamburg, Germany
Plate reader Sunrise	Tecan, Crailsheim, Germany
Roll mixer	VWR International, Darmstadt, Germany
Shaker Duomax 1030	Heidolph, Schwabach, Germany
Syringe pump	AL-1000, World precision instruments, USA
Scale Mettler PE3000	Mettler TOLEDO, Ohio, United States
Thermomixer compact	Eppendorf, Hamburg, Germany
Ultra-pure water supply MilliQ Advantage A10	Merck Millipore, Darmstadt, Germany
Vortex Mixer	IKA, Staufen, Germany
Gloves, eco nitrile PF 250	SHIELD Scientific, Bennekom, Netherlands
VWR® Tube Rotator and Rotisseries	VWR International, Darmstadt, Germany

Water bath Aqua Line AL 12	Lauda, Lauda-Königshofen, Germany
Water Bath 1002	GFL technology, Burgwedel, Netherlands

Software	Manufacturer
GraphPad Prism 5	GraphPad Software, La Jolla, USA
Image J	NIH, Wisconsin, USA
LightCycler® 480 SW 1.5	Roche Diagnostics, Mannheim, Germany
Magellan Software	Tecan, Crailsheim, Germany
Microsoft Office Professional Plus 2016	Microsoft, Redmond, USA
BD FACS Diva v8.0.1	BD Biosciences, Germany
ChemiDoc Imaging Systems	Bio-Rad, Germany

3. Methods.

3.1. Cells

3.1.1. *Mouse primary fibroblasts isolation from neonatal mouse lungs*

After administering a lethal dose of pentobarbital, lungs were retrieved from neonatal mice aged 5–7 days, regardless of gender. Subsequently, the lungs were carefully flushed with 1X PBS through the right ventricle, followed by excision of the sternum and extraction of the lungs. The lung lobes were then arranged in a 12-well plate containing ice-cold 1X PBS. Using a scalpel, the lung tissue was precisely sliced into 1 mm pieces, which were evenly distributed along the dish's surface with 500 uL of PBS. The dishes were allowed to air-dry at 37°C for approximately 15-20 minutes. Once the tissue fragments adhered to the dish's surface, 8 mL of DMEM-1 medium (Gibco, Darmstadt, Germany) supplemented with 10% fetal bovine serum (FBS), 1% Penicillin/Streptomycin, and 1% Gentamicin (Gibco, Darmstadt, Germany) were gently introduced. After three days, the medium and floating tissue fragments were discarded, and 10 mL of fresh medium was added. On the seventh day, any remaining tissue fragments were discarded, and 10 mL of new supplemented DMEM-1 medium was replenished. Experiments commenced once cell confluence reached 70 - 80%.

3.1.2. *Flow cytometry analysis*

To assess the purity of the isolated cell populations, flow cytometry was conducted using the following panel for fibroblast determination:

CD45 FITC

CD11b V450

CD90.2 APC

CD 105 PE

Myofibroblasts were characterized with a fluorescence-activated cell sorter (FACS LSRII) employing a multicolor staining technique. In brief, myofibroblasts were resuspended in FACS buffer (PBS + 2% FCS + 10 mM HEPES + 0.1% Na-Azide) and stained with CD90.2 APC FITC, CD 105 PE, CD45 FITC, and CD11b V450. After fixing to detect internal markers with 4% PFA, the myofibroblasts underwent permeabilization with 0.2% Triton X-100 and blocking with 1% BSA in PBS. Stained myofibroblasts were then acquired through BD TM LSR II utilizing BD FACSDiva™ software version 6.0 and analyzed using FlowJo version 9.6.1. The myofibroblast culture consisted of leukocytes ($14.6 \pm 5.11\%$ CD45+, $39.45 \pm 11\%$ CD11b), mesenchymal-like cells ($8.71 \pm 3.6\%$ CD105+, $0.15 \pm 0.04\%$ CD90+), and the remaining primary fibroblasts (Oak, P., Hilgendorff, A., 2017).

3.1.3. *Cell culture treatment*

3.1.3.1. *Hyperoxia exposure*

Seeded cells were treated with $\text{FiO}_2 = 0.4$ for 24 hours in a C-Chamber fitted with a ProOx 110 oxygen controller (Biospherix, Parish, NY).

3.1.3.2. *TGF β treatment*

Primary fibroblasts and CCL-206 cells were treated for 24 hours at 37° degrees with 5 ng/ml of TGF β (R&D Systems).

3.2. **MVH-68**

3.2.1. *Virus stock preparation*

The initial MHV-68 stock (clone G2.4) was sourced from J. Stewart and A. Nash at the University of Edinburgh, Edinburgh, United Kingdom (1). Subsequent working virus stocks were prepared using BHK-21 cells (ATCC CCL10), generously provided by J. Stewart and A. Nash. BHK-21 cells underwent infection with MHV-68 at a multiplicity of infection (MOI) of 0.1. After three days of cultivation, cells were subjected to two cycles of freezing and thawing to release

intracellular viruses. Centrifugation was applied to eliminate cellular debris, and the resulting supernatants were aliquoted and stored at -80°C . A plaque assay was executed to determine virus titer, and verification of the left viral genome presence was conducted through DNA extraction, PCR amplification, and agarose gel electrophoresis.

3.2.2. *Plaque assay (quantification of MHV-68)*

The plaque assay procedure was conducted according to the methodology described by Stewart et al. (2004). For virus titer assessment, BHK-21 cells were seeded at a specified density of 5×10^4 cells per well in 24-well plates (Corning, Germany), 24 hours prior to titration. Additionally, the overlay medium was prepared one day in advance: methylcellulose (Sigma Aldrich, Germany) was dissolved in the culture medium and stored at $+4^{\circ}\text{C}$. The virus aliquot was then serially diluted in the cell culture medium ($10^{-1} - 10^{-8}$).

The culture medium from the BHK-21 cells was aspirated, and 900 μl of each virus dilution was added, followed by a 90-minute incubation at 37°C . Subsequently, the infectious medium was removed, and pre-warmed overlay medium was applied. The plates were then incubated for 5 days at 37°C . After the incubation period, the overlay medium was discarded, and the adherent cell layer was stained using a 0.1% crystal violet solution. Plaques per well were determined under a microscope for plaque assay analysis.

$$\text{PFU/ml} = 1.1 \times \text{Dilution} \times \text{number of the plaques}$$

PFU/ml (plaque-forming unit) represents the unit for indicating the virus titer. The factor 1.1 adjusts the volume based on the 900 μl of infectious suspension added. Wells were examined for plaque presence during concentration calculations, starting from the lowest concentration (10^{-8}). Plaque numbers were determined in the first well where plaques were observed and in the subsequent one. The counts were then summed and divided by two to ensure calculation accuracy.

3.2.3. Cell infection

The viral solution was prepared in advance from the frozen virus stock (3.2.1), just before initiating the infection procedure. The formula for calculating the precise quantity of the viral solution was employed as follows:

$$\text{Virus solution, } \mu\text{l} = \frac{\text{desired MOI} \times \text{medium amount, ml} \times \text{number of cells} \times 1000}{\text{PFU/ml}}$$

The vial containing the virus stock with a known concentration was thawed at room temperature for approximately 3 - 5 minutes. The calculated amount of virus solution was then dissolved in the appropriate amount of media. Following treatment, cells were washed twice with 1xPBS and subsequently incubated with the virus solution for 1 hour at 37°C. The infectious medium was then replaced with an equivalent amount of fresh medium. Infected cells were further incubated at 37°C for 24 hours before either harvesting the cells or conducting functional analysis.

3.2.4. Determination of the number of infected cells

CCL-206 and mouse primary fibroblasts were subjected to infection with a recombinant MHV-68 expressing GFP, following the infection protocol outlined in section 3.2.3. Post a 24-hour incubation, the medium was discarded, and flasks/dishes were washed with 1X PBS. Subsequently, trypsinization was carried out using a pre-warmed 0.25% trypsin-EDTA (Gibco) solution for 5 minutes at 37°C. The cells were then centrifuged at 8000g for 5 minutes at 24°C, resuspended in 1xPBS, and centrifuged again. The resulting pellet was dissolved in 100 μl of 2% PFA in PBS and transferred to FACS tubes. Acquisition of infected cells was performed using BDTM LSRFortessa with BD FACSDiva™ software version 8.0, and subsequent analysis for GFP expression was conducted using Flowing Software 2.5.1.

3.2.5. Determination of viral replication

Cells treated with TGF β or exposed to hyperoxia were infected with 0.1 MOI MHV-68 and incubated at 37°C, 5% CO₂ for 0, 24, 48, 72, and 96 hours. The

infected cell cultures underwent three freeze-thaw cycles, followed by centrifugation for 15 minutes at 8000 x g at room temperature to eliminate cell debris. The supernatant was carefully collected, and virus titers were assessed through the plaque assay (3.2.2). Subsequently, a graph was constructed with $\log_{10}(\text{PFU/ml})$ on the Y-axis and time (hours) on the X-axis.

3.3. Functional assays

3.3.1. Trypan blue cell counting

After a 24-hour treatment and infection period at 37°C with 5% CO₂, cells were harvested using Trypsin-EDTA (Gibco). The collected medium, along with cells and trypsin, was carefully placed in the same tubes. Following centrifugation for 5 minutes at 8000 x g at room temperature, the supernatant was discarded, and the pellet was reconstituted in 1 ml of fresh medium. A 10 µl aliquot of this suspension was combined with 10 µl of Trypan Blue Solution 0.4% (Gibco), and 10 µl from this mixture was loaded into the Neubauer Hemocytometry Chamber (0.100 mm depth, 0.0025 mm²). Viable and nonviable cells were manually counted separately in the hemocytometer.

To determine the total number of viable cells per ml of the aliquot, the total count of viable cells was multiplied by 2 (the dilution factor for trypan blue). Additionally, to ascertain the total number of cells per ml of the aliquot, the combined count of viable and nonviable cells was summed and then multiplied by 2. The percentage of viable cells was calculated as follows:

$$\text{Viable cells (\%)} = \frac{\text{total number of viable cells per ml of aliquot}}{\text{total number of cells per ml of aliquot}} \times 100.$$

3.3.2. Wound healing "scratch" assay

For the scratch wound healing assay, cells were plated in 6-well plates. Following treatment with TGFβ or exposure to hyperoxia, cells underwent infection, and an artificial scratch was manually created using a 200 µl tip. Subsequently, the cells

were washed with 1X PBS to eliminate any cell fragments or detached cells, covered with culture medium, and an immediate microscope image was captured. The cells were then incubated for 24 hours (at 37°C, 5% CO₂), and another image was captured. Using the freely available software "ImageJ," the scratch area was quantified at each time point and under each condition. Subsequently, the wound closure was determined through the following calculation:

$$\text{Wound closure, \%} = \frac{(\text{initial scratch area, 0 hours} - \text{scratch area at 24 hours}) \times 100\%}{\text{initial scratch wound area, 0 hours}}$$

3.3.3. *Migration measurement assays*

3.3.3.1. *Cell Migration Assay*

The assay was conducted following the guidelines provided by the manufacturer, utilizing the CytoSelect 96-well Cell Migration Assay Kit, 8 µm, Fluorometric Format (ab235673). In the commercial migration assay, cells were seeded in 6-well plates, exposed to hyperoxia, treated with TGFβ, and infected with MHV-68 for 24 hours (incubated at 37°C, 5% CO₂). After this period, the culture medium was replaced with an equivalent volume of 1% FBS fresh medium. The chemoattractant-containing medium (10% FBS) was prepared beforehand. Following 24 hours of infection, cells were washed twice with 1xPBS, detached with Trypsin, and centrifuged for 5 minutes at 8000 x g at room temperature. The supernatant was discarded, and the pellet was reconstituted in 1 ml of medium.

The specialized 96-well migration plate from the commercial Cell Migration Assay Kit was equilibrated from -20°C to room temperature for 10 minutes. Cell counting was performed using a Neubauer chamber, and the cell suspension was diluted with medium to achieve a concentration of 1,000,000 cells per ml. In a sterile environment, the Migration Plate was carefully disassembled into three components: the top-plate cover, middle-membrane chamber, and bottom-feeder tray. A volume of 150 µl of medium with the specified chemoattractant was added to the wells of the feeder tray. Subsequently, the membrane chamber was precisely placed back into the feeder tray, and 100 µl of the cell suspension was

added to each well. The migration chamber was covered with the plate cover and incubated in the cell culture incubator for 24 hours (37°C, 5% CO₂).

After removing the cell and media from the upper side of the membrane chamber by aspiration, it was transferred to the Cell Harvesting Tray, and migrated cells were detached from the bottom of the membrane chamber by incubating in 150 µl of Cell Detachment Solution for 30 minutes at 37°C. A 4X Lysis Buffer/CyQuant GR® dye solution was prepared (1 part dye and 75 parts 4x Lysis Buffer) and added to each well in a volume of 50 µl. The tray was incubated for 20 minutes at room temperature, and 150 µl of the mixture was transferred to a suitable 96-well plate for fluorescence measurements. The fluorescence signal was detected using a GloMax® Explorer Multimode Microplate Reader (Promega) at 480 nm emission light / 520 nm excitation light.

3.3.3.2. *Cell Migration/Chemotaxis Assay*

The assay was conducted in accordance with the manufacturer's guidelines using the EZCell™ Cell Migration/Chemotaxis Assay Kit, 8 µm (# K906-100). All procedures were executed as outlined in section 3.3.1, with the exception of the cell detachment step. In this variant, cells were dislodged from the membrane chamber using a cotton swab. Subsequently, the chamber was disassembled from the migration plate, inverted, and set aside. The feeder tray was then sealed and centrifuged at 1,000 x g for 5 minutes at room temperature. Following this, the media was removed from the feeder tray, washed with 200 µl of wash buffer, and centrifuged at 1,000 x g for 5 minutes at room temperature. The Cell Dye Solution was prepared by combining 1 part Cell Dye and 10 parts Cell Dissociation Solution. Subsequently, 110 µl of this mixture was added to each well of the feeder tray. The cell migration chamber was reassembled and incubated at 37°C in a CO₂ incubator for 60 minutes. The top chamber was then removed, and the fluorescence signal was recorded using a GloMax® Explorer Multimode Microplate Reader (Promega) at 530 nm emission light / 590 nm excitation light.

3.3.4. Apoptosis measurement assays

3.3.4.1. Caspase-Glo 3/7 assay

The experiment was carried out following the guidelines provided by the manufacturer, Promega. Briefly, cells were seeded in 96-well imaging plates at a density of 10,000 cells/100 μ l. After various cell treatments, which included 24 hours of hyperoxia exposure or TGF β treatment, 1 hour of MHV-68 infection, and 24 hours of recovery in the incubator at 37°C with 5% CO₂, a mixture of 100 μ l of Caspase Glo® 3/7 Reagent (comprising buffer and lyophilized substrate) was added, and cells were incubated at room temperature for 60 minutes. The luminescence signal was then detected on the GloMax® Explorer Multimode Microplate Reader (Promega) using the built-in program.

3.3.4.2. RealTime-Glo Annexin V Apoptosis and Necrosis Assay

The experiment was conducted following the manufacturer's protocol (Promega). In summary, cells were seeded in 96-well imaging plates at a density of 10,000 cells/100 μ l. After cell treatment (24 hours of hyperoxia exposure or TGF β treatment, 1 hour of MHV-68 infection, 24 hours' recovery in the incubator at 37°C, 5% CO₂), 100 μ l of 2x Detection Reagent (24 μ l Annexin V-LgBiT, 24 μ l Annexin V-SmBiT, 24 μ l CaCl₂, 24 μ l Annexin V NanoBiT® Substrate, 24 μ l Necrosis Detection Reagent, 12 ml medium) was added and shaken for 30 sec at 500–700 rpm to mix. The luminescence and fluorescence signals were then detected on the GloMax® Explorer Multimode Microplate Reader (Promega) following the plate reader's built-in program at the time points 24 hours, 48 hours, and 72 hours after infection.

3.3.5. MTT Cell viability measurements

Cell viability assays utilizing XTT and MTT gauge the redox potential within metabolically active cells, converting tetrazolium-based salt reagents (MTT or XTT) into a vividly colored insoluble formazan product through NAD(P)H-dependent processes. Initially, a 5 mg/ml MTT solution was prepared by dissolving soluble MTT (Sigma) in 1X PBS, followed by vortexing, filter

sterilization, and storage at -20°C in darkness. Subsequently, the MTT solvent was created by combining 0.1% Triton-X-100 (Aplichem) in isopropanol. For the experiment, cells were seeded in a 96-well plate at a density of 10,000 cells in $100\ \mu\text{l}$ per well, and the treatment was administered. After 24 hours of infection, $20\ \mu\text{l}$ of the MTT solution was added to each well and incubated at 37°C for 4 hours. Wells with 0.1% DMSO and medium served as the negative control, while wells containing only media served as the blank control. The medium was then gently aspirated, and the formazan crystals formed were dissolved in $100\ \mu\text{l}$ of the MTT solvent. Subsequently, the absorbance of the plate was measured at 570 nm using a Tecan-ELISE-Reader (Life Sciences) according to the built-in program of the plate reader.

3.4. Analytical assays

3.4.1. Protein isolation from cells in 2D cell culture

Cells cultured in standard 6-well dishes were washed twice with sterile 1X PBS and then trypsinized with 0.25% Trypsin. Upon trypsinization, complete medium was added, followed by centrifugation at 450 rpm for 5 minutes at 4°C . After removing the supernatant, the pellet was reconstituted in $150\ \mu\text{l}$ of lysis buffer, which included RIPA buffer enriched with a Halt protease inhibitor cocktail (Thermo Fisher Scientific). The resulting cell lysates were carefully mixed by pipetting up and down, as well as vortexing. The lysates were then transferred to an Eppendorf tube, placed on ice, and incubated for 30 minutes. Subsequently, the lysates underwent centrifugation at 15,000 RPM for 15 minutes at 4°C to separate the supernatant (total protein) from the pellet (cell debris). Finally, the cell supernatants were pipetted into Eppendorf tubes and stored at -80°C for long-term preservation.

3.4.2. Bicinchoninic acid (BCA) assay

Protein concentrations in tissue and cell lysates were determined using the bicinchoninic acid assay (BCA assay) following the manufacturer's guidelines (Thermo Fisher Scientific). To establish protein concentrations, a standard curve was generated using known bovine serum albumin (BSA) concentrations to

create a concentration range of 0-2 $\mu\text{g}/\mu\text{l}$, diluted in RIPA Buffer. In a 96-well plate, cell lysates were mixed with RIPA buffer in a 1:4 or 1:10 ratio, with RIPA buffer serving as the blank. BSA standards and samples (10 $\mu\text{l}/\text{well}$) were pipetted into the same plate, and all samples were duplicated. Subsequently, 200 μl of the BCA reagent was added to each well. After incubation at 37 °C for 30 minutes, the absorbance was measured at 562 nm using a Sunrise TM plate reader (TECAN) to estimate protein concentrations.

3.4.3. SDS-PAGE and immunoblotting

Protein samples obtained from cell lysates were mixed with NuPAGE® Reducing Agent (10X), NuPAGE® LDS Sample Loading Buffer (4X), and deionized water. Electrophoresis was conducted using Tris-Acetate (Life Technologies), Tris-glycine (Life Technologies), or Bis-Tris (Life Technologies) gel at a voltage ranging from 80 to 120 V per gel. For the immunoblotting step, the proteins were transferred to Nitrocellulose membranes (Life Technologies) activated with transfer buffer at 30V for 90 to 100 minutes. After transfer, the membranes were blocked using 5% milk in 1xTBS-T (0.1% Tween®20 in TBS) for 120 minutes, followed by overnight incubation with primary antibodies at 4°C. The next day, after three 5-minute washes with 1xTBS-T, the membranes were exposed to HRP-conjugated secondary antibodies at room temperature for 2 hours. Following antibody incubation, the nitrocellulose membranes underwent three 5-minute washes with 1X TBST. Finally, protein visualization was achieved using Femto SuperSignal® western blot chemiluminescent substrates (Thermo Fisher), and the protein signal was detected using the Chemidoc XRS+ system from Bio-Rad. Specific details regarding the primary and secondary antibodies, including their dilutions, can be found in the materials section (1.1.).

3.4.4. RNA extraction from cells in 2D cell culture

RNA extraction from cells in 2D culture followed the protocol outlined by Qiagen's Nucleo Spin RNA plus mini kit (Macherey-Nagel Company). For mRNA isolation, 600 μl of RLT Lysis buffer (Qiagen) per well was added and incubated at room temperature for 5 minutes, followed by vortexing for 30 seconds. Subsequently, the samples were loaded into gDNA eliminator columns and centrifuged. The

resulting flowthrough was combined with 1200 μ l of 70% ethanol. Following this, the samples were introduced into RNeasy spin columns. In the ensuing steps, the samples underwent a series of washes: once with 700 μ l RW1 buffer, once with 600 μ l of RPE buffer, and another time with 600 μ l of RPE buffer (2 minutes). The final elution was performed using 35 μ l of RNase-free distilled water. The concentration of the isolated RNA was determined spectrophotometrically at a wavelength of 260 nm using the Nano-Drop 1000.

3.4.5. cDNA synthesis by Reverse Transcription

For cDNA synthesis, 1 μ g of the isolated mRNA was diluted with sterile nuclease-free water to achieve a total volume of 20 μ l. Subsequently, a master mix was created using the specified concentrations of the following reagents:

Reagents	Stock concentration	Final concentration	Final volume
RT-Puffer	10 X	2 X	2 μ l
dNTPs	25 X	1 X	0,8 μ l
Random Primer	10 X	1 X	2 μ l
Reverse Transcriptase	50 E/ μ l	5 E/ μ l	1 μ l
dd H ₂ O	-	-	4,2 μ l
Total volume master mix			10 μ l

For the reverse transcription reaction, 10 μ l of the MasterMix was mixed with the 10 μ l of the dissolved RNA solutions and incubated for 10 minutes at room temperature, then for 120 minutes at 37° degrees.

3.4.6. qRT-PCR

The SYBR Green LC480 (Roche) was used to perform the quantitative real-time RT-PCR. The master mix was prepared as follows:

Reagent	Stock concentration	Final concentration	Final volume (μl)
SYBR green I master	2X	1X	5
Forward / Reverse Primer mix	10 μM each	0.5 μM each	1
Dnase-free water	-	-	1.5

In a 96-well plate, 2.5 μl of cDNA sample per well were pipetted in duplicate, and 7.5 μl of the master mix were consistently added in duplicate. Prior to commencing measurements, the plates were centrifuged for 1.5 minutes at 1000 rpm. The reaction was carried out using the following program:

95°C for 5 minutes, followed by

45 cycles of 95°C for 5 seconds (denaturation),

59°C for 5 seconds (annealing),

72°C for 20 seconds (elongation),

60 – 95°C for 1 minute with continuous acquisition (melting curve).

Following data collection, the reference gene Glyceraldehyde 3-phosphate dehydrogenase (GAPDH) was utilized to standardize the expression of target genes (Reference Gene CT value - Target Gene CT value). Relative gene expression was determined using the $\Delta\Delta\text{CT}$ method.

3.5. Animal experiments

3.5.1. Hyperoxia exposure

Newborn mice of the C57BL/6 wild-type (WT) strain, aged between five to seven days and born at term gestation [with a body weight of 3.6 ± 0.3 g], were randomly assigned to two groups ($n = 6-8$ mice/group). The mice were either exposed to oxygen ($\text{FiO}_2 = 0.4$) using the A-Chamber (Oxygen controller ProOx110, Biospherix, Parish, NY) or received only room air (RA; $\text{FiO}_2 = 0.21$) for a duration of 24 hours (conducted as short-term experiments).

3.5.2. MHV-68 infection

Eight days after exposure to hyperoxia or room air, mice were anesthetized before being infected with 2.5 $\mu\text{l/g}$ of an antagonizable anesthetic solution containing 1 mg/ml Medetomidine, 5 mg/ml Midazolam, and 0.05 mg/ml Fentanyl. Subsequently, all mice were intranasally infected with 1×10^4 PFU in 10 μl of PBS. Following infection, anesthesia was reversed using 8.5 $\mu\text{l/g}$ of the corresponding antagonist solution (5 mg/ml Antipamezole, 0.1 mg/ml Flumazenil, and 0.4 mg/ml Naloxone). The mice were euthanized and analyzed at 3, 6, 10, 28 days, or 4 – 6 months post-infection (see Figure 3.5.1).

Animal experiments were approved by the Government of Upper Bavaria, #ROB-55.2-2532.Vet_02-19-105.

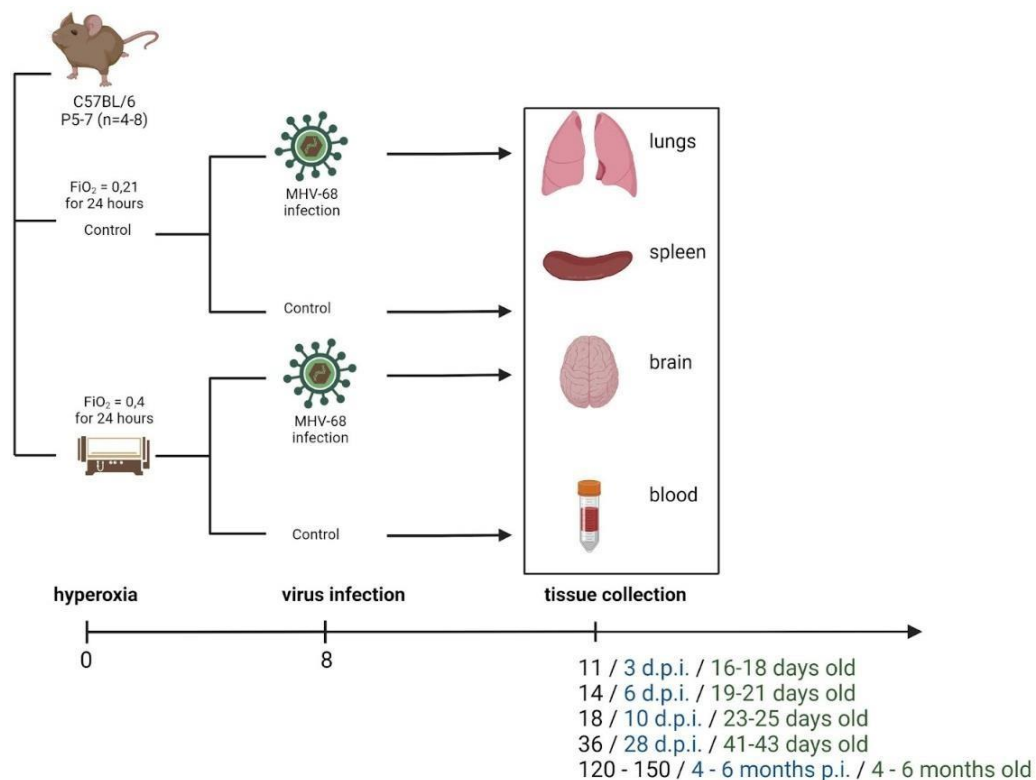


Figure 3.5.1. Double-hit model experimental design.

Mice pups at the age of 5-7 days were treated with $\text{FiO}_2 = 0.4 / 0.21$ for 24 hours and allowed to recover for 8 days before intranasal inoculation with MHV-68. Lungs were harvested from 4 - 6 mice at 3, 6, 10, and 28 days or 5 – 6 months post-infection.

3.5.3. Organs harvesting

The animals were humanely euthanized at designated time intervals post-infection through cervical dislocation. Subsequently, the spleens, lungs, and

brains were dissected, placed in sterile Eppendorf tubes, and stored at -80°C . Blood collection was carried out using a 1 ml syringe, followed by centrifugation at $10,000 \times g$ for 10 minutes. The resulting serum was then transferred to sterile Eppendorf tubes and stored at -80°C .

3.5.4. Brain and lung fixation and paraffin embedding

The animals were killed at defined time points post-infection via injection with a lethal dose of pentobarbital. Brains were fixed with 4% buffered PFA (24 hours), which then was replaced with the PBS solution for 3 – 5 days. Further, according to the manufacturer's protocol, brains were placed in the dehydrogenation machine for several hours. Lungs were placed into 4% buffered PFA (24 hours) and then placed into PBS solution for 3 – 5 days. The next step was the manual paraffinization process.

3.5.5. Haematoxylin Eosin staining

Formalin-fixed paraffin-embedded (FFPE) lung tissue sections from mice subjected to hyperoxia and controls, as well as those exposed to both hyperoxia and virus alongside controls, underwent an initial incubation at 60°C for one hour, followed by tissue deparaffinization. The slides containing the tissue sections then underwent a sequential process involving two incubations in Xylene for 5 minutes each, followed by incubations in 100%, 90%, 80%, and 70% ethanol for 2 minutes each. This was succeeded by a 5-minute incubation in 1xPBS. Subsequently, the slides were stained with Hematoxylin Mayer for 10 minutes. After rinsing with tap water, the slides were immersed in a 1% Eosin solution (Carl Roth) for 1 minute and then washed in VE water. The slides were then dehydrated through successive immersions in 80% ethanol, 90% ethanol, 100% ethanol, and Xylene (5 min each). Finally, coverslips were mounted using a Xylol-based Fast Mounting Medium (Biosystems). Following isotropic uniform, random (IUR) sectioning (Scherle, 1970), quantitative assessments of alveolar area and radial alveolar counts (≥ 30 fields of view; 400X magnification) were conducted on 2-3 independent random $4 \mu\text{m}$ H&E tissue sections per animal using CAST-Grid 2.1.5 (Olympus) (Emery & Mithal, 1960).

3.5.6. Homogenization of the lung or spleen tissue

To homogenize lung or spleen samples, the respective organs were placed in dedicated sterile homogenization tubes containing a small ceramic bullet and 350 µl of the lysis buffer (RLT plus buffer for RNA isolation), 500 µl of the RIPA buffer (for protein isolation), or BHK-21 cell line media (for Plaque assay). Homogenization was conducted using the FastPrep-24 instrument (MP Biomedicals) with the following parameters: lung samples were homogenized once at 4 m/s for 20 seconds. Subsequently, the homogenates were directly utilized for RNA or protein extraction.

3.5.7. Determination of lung viral titers

The MHV-68 titer was determined in the right lung lobe by plaque assay described in **3.2.2**. The right lobe was homogenized in BHK-21 media (described in point 5.10.).

3.5.8. Determination of viral load in spleens

Firstly, DNA was extracted from spleens, as was described in the QIAamp DNA Mini Kit protocol (Qiagen). The viral load in the spleens of infected mice was determined by qPCR with the TaqMan System. The principle is based on a standard PCR reaction which enables the quantification through the measurement of fluorescence, released by labeled probes that bind to the viral DNA. The probes used in this study were attached at the 5' end to the reporter FAM or HEX and at the 3' end to the quencher TAMRA or BHQ-1 (L8-1 Probe: Hex-ACCACCAGCACATTGGCAAACC-BHQ-1; Gb Probe: Fam-ACAAGCTGACCACCAGCGTCAACAAC-Tamra). Primers and a probe for the viral glycoprotein B (gB) and the cellular reference gene L8 were used. For each quantification reaction, a standard curve (10^1 to 10^8 copies) was used to correlate the Ct values to a corresponding quantity.

The spleen was cut manually into small pieces and added to the 180 µl of ATL buffer and 20 µl of proteinase K. The mixture was incubated overnight at the 56° heating block. The following day, the tube was centrifuged for a short time to get rid of the drops from the inside of the lid. 4 µl of RNase A was added, and the

solution was mixed by vortexing for 15 seconds and incubated at room temperature for 2 minutes. Then, 200 µl of AL Buffer was added, and the tube was vortexed again for 15 seconds and incubated at 70° for 10 minutes. The solution was placed on the QIAamp Mini Column and centrifuged for 1 min at 8,000 rpm. The supernatant was discarded, and the column was washed by AW1 and AW2 buffers. The collected DNA concentration was measured using the NanoDrop. The DNA amount was adjusted to 100 ng/sample.

To measure viral genomic load the following master mix was made:

Reagent	Volume per sample
gB Probe	1,5 µl
Primer gBRev	1,5 µl
Primer gBForward	1,5 µl
L8 Probe	1,5 µl
Primer L8Rev	1,5 µl
Primer L8Forward	1,5 µl
TaqMan Universal PCR Master Mix	12,5 µl

The DNA samples were dissolved to obtain 200 ng per 8 µl of each sample.

The measurements were performed in the 7300 Real-Time PCR System (Applied Biosystems), and the following 3-step program was applied:

1. Initial denaturation at 95°C for 10 min (1 cycle)
2. Denaturation at 95°C for 15 sec (40 cycles)
3. Hybridization and elongation at 60°C for 1 min (40 cycles)

For the analysis and determination of the viral load in the samples, the genome copies measured for the gB were normalized to the genome copies of L8 using the following formula:

$$\frac{\#(\text{gB}) * 1000}{\#(\text{L8})}$$

3.6. Statistical analysis

GraphPad Prism v9.0 (GraphPad Software) was used to perform statistical analysis. The data were presented as mean ± standard deviation (SD). Unpaired

and paired t-tests (two-tailed) or One-way ANOVA with Dunnett's multiple comparison test were applied for normally distributed data. In the case of non-normally distributed data, non-parametric tests such as Mann-Whitney U tests or the Wilcoxon signed-rank test for paired samples were employed. The Kruskal-Wallis test with Dunn's test for post hoc analysis was utilized for multiple comparison.

4. Results

4.1. ***Effects of in vitro infection of mouse primary fibroblasts and CCL-206 cells by MHV-68 in the presence or absence of hyperoxia or TGF- β pre-treatment***

4.1.1. *Effects of in vitro MHV-68 infection in mouse primary fibroblasts and CCL-206 cells*

Viral infections of the respiratory system in adults constitute a comprehensive area of research. Respiratory viral infections have been identified as a factor associated with chronic lung diseases, affecting both childhood asthma and adults grappling with severe asthma and chronic obstructive pulmonary disease (COPD) (Singanayagam, A. et al, 2012). Originally, the connection between viral infections and chronic lung disease in humans was primarily observed in cases of severe infections caused by respiratory syncytial virus (RSV). However, this association has since been broadened to include human metapneumovirus and human rhinovirus (HRV) (Keeler, S. P. et al, 2018). Among the other viruses, herpesviruses have exhibited potential implications in the pathogenesis of pulmonary disorders, particularly fibrosis, as elucidated by investigations conducted by Williams et al. in 2014. In certain investigations concerning MHV-68 infection, researchers have chosen to use adult mice, specifically those that are 12 months old, as elucidated in the study conducted by Mora A et al. in 2005. To study the relationship among murine gammaherpesvirus-68 (MHV-68) infection, oxidative stress, and cytokine expression, Bortz et al. (2018) conducted experiments using 12-week-old mice. Nevertheless, there is a notable scarcity of literature addressing infection in neonatal mice and its effects on lung development during the saccular stage.

To investigate the effect of MHV-68 in the developing lung, we adapted the experimental methodology for fibroblast cell line CCL-206, derived from mouse lungs, to determine whether this cell line was susceptible to MHV-68 infection.

Next, we used primary cell cultures consisting of neonatal mouse lung fibroblasts obtained from neonatal mice (with an equal gender distribution of three females and two to three males, aged between 5 and 7 days of life (DOL)). The infection rate in CCL-206 cells was assessed in the room air mode (normoxia, $FiO_2 = 0.21$) by infecting the cells with recombinant MHV-68 expressing GFP in different concentrations (0,1 MOI, 1 MOI, and 3 MOI) (**Figure 4.1. A**). The primary fibroblasts were exposed to MHV-68 expressing GFP, same in normoxia with MOI values of 0, 0.1, 1, and 3 (**Figure 4.1. B**). In both cell lines, 24 hours after infection, the number of GFP-positive cells was determined using flow cytometry. We observed a dose-dependent increase in infection rates in CCL-206 cells, with the 3 MOI dosage infecting 91-98% (**Figure 4.1. A**). In primary neonatal mouse lung fibroblasts, recombinant MHV-68 incubation for 24h resulted in a dose-dependent infection rate with 3 MOI in normoxia reaching an infection rate of approximately 30% in the cell population (**Figure 4.1. B**). No differences in GFP-signal obtained in female and male primary neonatal lung fibroblasts were revealed (**Figure 4.1. C and D**).

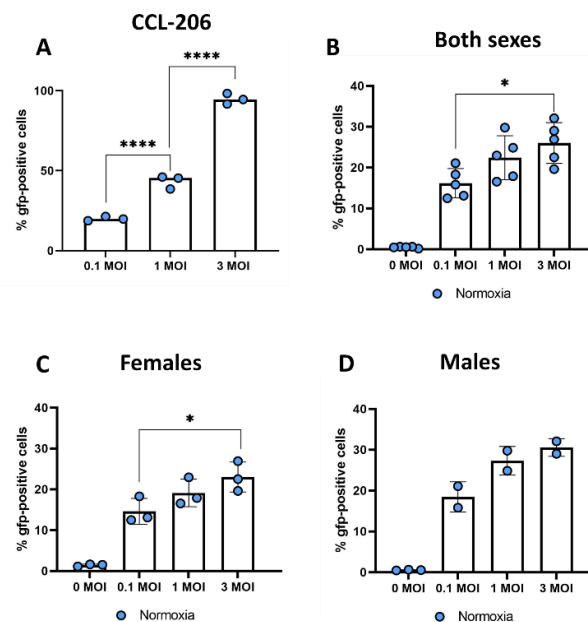


Figure 4.1. Recombinant MHV-68 expressing GFP infects CCL-206 and primary neonatal mouse lung fibroblasts.

MHV-68 infection rates in mouse primary lung fibroblasts in normoxia ($FiO_2 = 0.21$). A - MHV-68 infection rates in CCL-206 cells in normoxia, $n=3$ ($FiO_2 = 0.21$). Mouse primary fibroblasts were isolated from the lungs of $n=3$ female (C) and $n = 2 - 3$ male (D) newborn mice. In B, expression levels are combined for both sexes. One-way ANOVA test with multiple comparisons correction. * p -value < 0.05 , *** p -value < 0.001 , **** p -value < 0.0001 .

Damage to the lungs frequently exhibits heterogeneity, forcing diverse regenerative responses depending on the nature and extent of the injury. Given that pulmonary fibrosis is marked by the proliferation of fibroblasts and alterations in cell fate (Pardo and Selman, 2016), it is critical to comprehend the determinants of cell fate in CCL-206 cells and neonatal mouse primary fibroblasts to gain insights into the repercussions of viral infection on pulmonary damage. Cell fate decisions require a strict balance between cell metabolic activity, cell proliferation, and cell death. To explore whether virus infection affects these programs in CCL-206 cells and primary neonatal mouse lung fibroblasts, I assessed metabolic activity, apoptosis, necrosis as well as proliferation.

To determine the cellular viability or metabolic activity in CCL-206 cells and neonatal mouse lung primary fibroblasts, cells were infected with MHV-68 ($n = 3 - 5$) for 24 hours and checked for viability with the MTT assay (**Figure 4.2.**). CCL-206 exhibited no changes in metabolic activity upon exposure to virus infection (**Figure 4.2. A**). MHV-68 infection did not alter the metabolic activity in mouse primary fibroblasts. However, primary fibroblasts obtained from the lungs of female neonate mice after viral infection exhibited a trend of increased metabolic activity, while those from the lungs of infected male mice showed no significant impact on metabolic activity (**Figure 4.2. B, C, and D**).

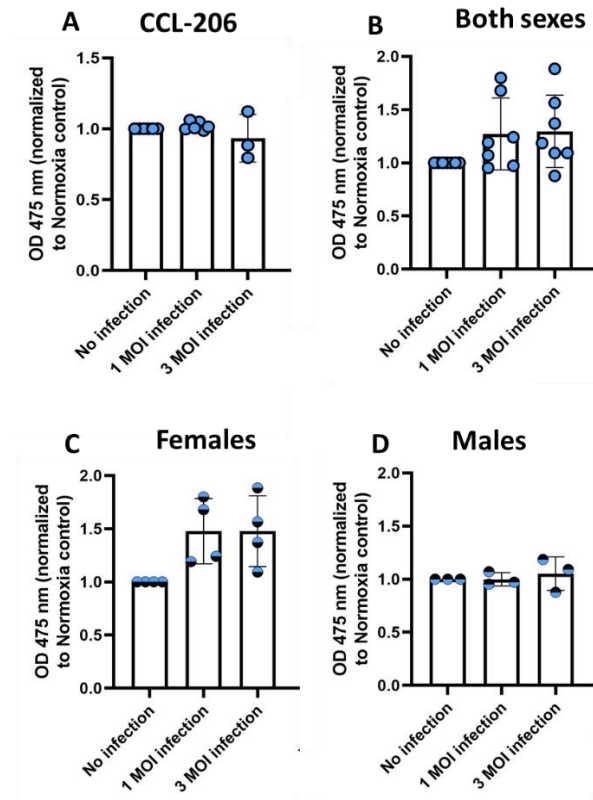


Figure 4.2. MHV-68 infection did not change metabolic activity in primary neonatal mouse lung fibroblasts.

Impact of MHV-68 infection on the metabolic activity of CCL-206 cells and mouse primary fibroblasts (A – CCL-206 (n=4), B – both sexes, C – females (n=4), D – males (n=5)). Mouse primary fibroblasts were isolated from the lungs of newborn mice. Statistical analysis: two-way ANOVA test for the continuous outcome variables of two nominal predictor variables, *p<0.05.

Following viral infection, apoptosis is also an important element of the cellular reaction to injury. Annexin V, which binds to the phospholipid phosphatidylserine (PS), serves as a marker of membrane disruption and PS exposure (Brauchle, E. et al., 2014). CCL-206 cells were not checked for Annexin V binding. I investigated Annexin V (RealTime-Glo™ Annexin V Apoptosis and Necrosis Assay) binding in mouse primary fibroblasts to assess the effects of MHV-68 infection throughout 24, 48, and 72 hours.

MHV-68 infection increased Annexin V binding in neonatal lung mouse primary fibroblasts at 24 and 48 h post-infection (**Figure 4.3. A**). Both female and male samples exhibited a statistically significant increase in Annexin V binding, with

females displaying a greater signal intensity. Notably, this elevation persisted even 72 h after infection (**Figure 4.3. B and C**).

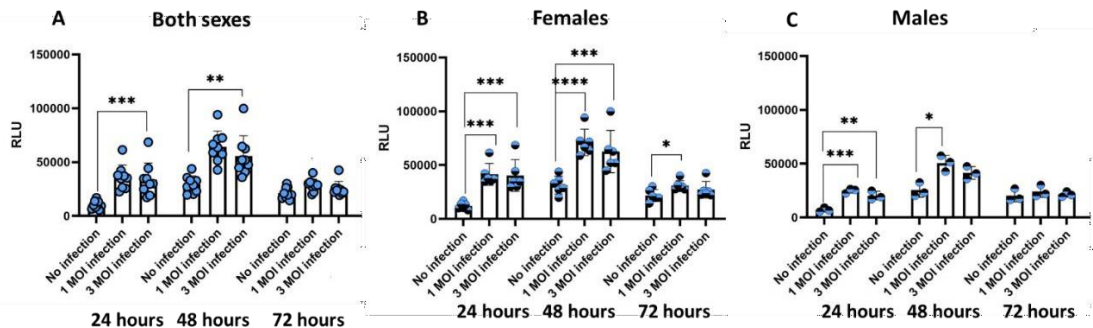


Figure 4.3. Annexin V binding after MHV-68 infection of primary neonatal mouse lung fibroblasts.

Mouse primary fibroblasts were isolated from the lungs of $n = 6$ female (B) and $n = 3$ male (C) newborn mice. In A, expression levels are combined for both sexes. RLU: relative luminescence units. Statistical analysis: one-way ANOVA test with correction for multiple comparisons. * $p < 0.05$, ** $p < 0.01$, *** $p < 0.001$, **** $p < 0.0001$. A one-way ANOVA test with Tukey's test for multiple comparison correction was used when comparing more than two groups.

Given Annexin V's ability to bind to apoptotic cells with intact plasma membranes, I investigated Caspase 3/7 activity in CCL-206 cells and mouse primary neonatal lung fibroblasts after 24 hours of MHV-68 infection (**Figure 4.4**). MHV-68 infection did not impact Caspase 3/7 activity after 24 hours of infection both in CCL-206 cells and mouse primary lung fibroblasts.

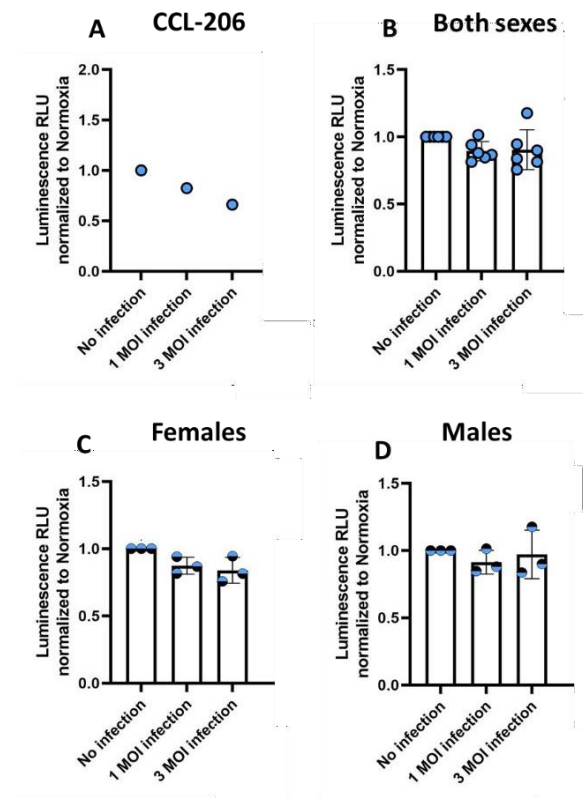


Figure 4.4. Caspase 3/7 activity after MHV-68 infection in primary neonatal mouse lung fibroblasts in normoxia ($FiO_2 = 0.21$).

(A) Activity of the Caspase 3/7 (Caspase Glo 3/7) in CCL-206 cells after MHV-68 infection ($n=1$). Mouse primary lung fibroblasts were isolated from $n = 3$ female (C) and $n = 3$ male (D) newborn mice. In B, measured Caspase 3/7 activities are combined for both sexes. Statistical analysis: one-way ANOVA test with correction for multiple comparisons. * $p < 0.05$, ** $p < 0.01$, *** $p < 0.001$, **** $p < 0.0001$. A one-way ANOVA test with Tukey's test for multiple comparison correction was used when comparing more than two groups.

Necrosis represents a mode of cell demise characterized by cellular swelling and rupture, often accompanied by inflammation. Random degradation of genomic DNA occurs in this process, which can be identified through the use of a luciferase substrate, calcium chloride, and a fluorogenic DNA dye impermeable to cells. While necrosis in CCL-206 cells was not examined, I specifically examined necrosis in primary neonatal mouse lung fibroblasts to evaluate the impact of MHV-68 infection over 24, 48, and 72 hours (RealTime-Glo™ Annexin V Apoptosis and Necrosis Assay). MHV-68 infection significantly increased necrotic processes in primary neonatal mouse lung fibroblasts (**Figure 4.5. A**). Male and female primary lung fibroblasts demonstrated the same necrosis level throughout the experiment (**Figure 4.5. B and C**).

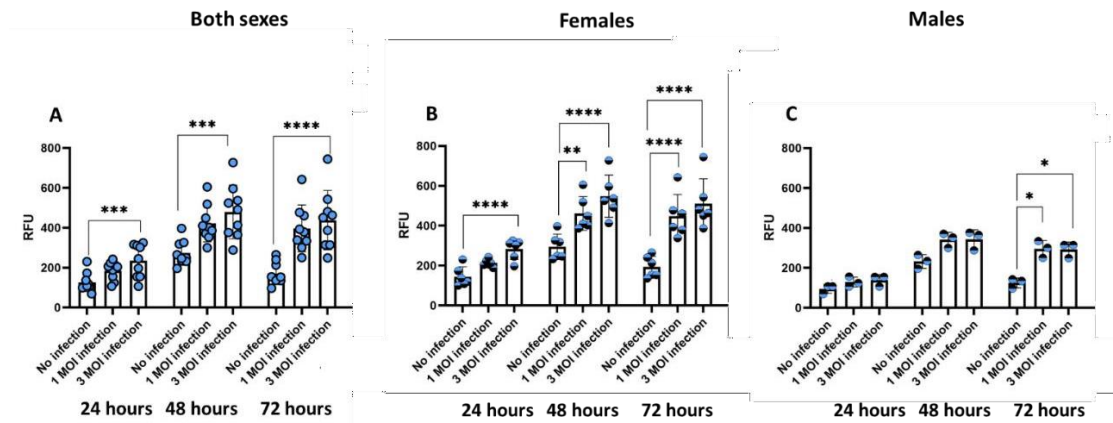


Figure 4.5. Necrosis after MHV-68 infection of primary neonatal mouse lung fibroblasts.

Mouse primary fibroblasts were isolated from the lungs of $n = 6$ female (B) and $n = 3$ male (C) newborn mice. In A, necrosis measurements are combined for both sexes. RFU: relative fluorescence units. One-way ANOVA test with multiple comparisons correction. * p -value < 0.05, ** p -value < 0.01, *** p -value < 0.001, **** p -value < 0.0001.

Cell proliferation and migration are critical processes in multicellular organisms. I investigated how MHV-68 infection can impact the proliferation and migration of primary neonatal mouse lung fibroblasts. Following MHV-68 infection, neonatal mice primary lung fibroblasts exhibited signs of damage (**Figure 4.6.**), with higher viral dosages leading to increased cell shrinkage and a reduction in the cell number.

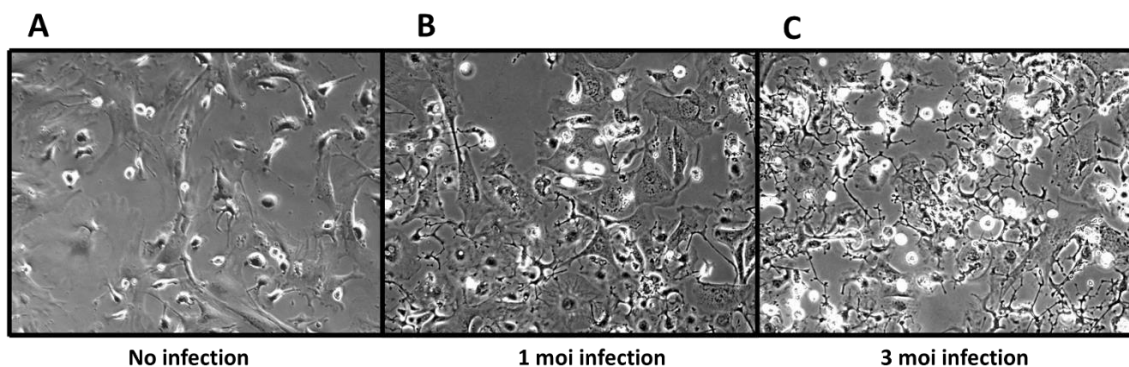


Figure 4.6. Images of primary neonatal mouse lung fibroblasts.

Mouse primary fibroblasts were isolated from the lungs of newborn mice. Normoxia conditions without infection (A), 24 hours of MHV-68 1 MOI infection (B), and 3 MOI infection (C).

A scratch wound-healing assay was used to investigate the ability of CCL-206 cells and primary neonatal mouse lung fibroblasts to proliferate and migrate (**Figure 4.7.** and **Figure 4.8.**). The assay is described in **Methods 3.3.2.** In normoxia and without virus infection ($\text{FiO}_2 = 0.21$), the wound area decreases over time, measurements of the wound closure show the percentage of area reduction. Infection with MHV-68 for 24 hours was found to significantly impair the ability of CCL-206 cells and neonatal mouse lung primary fibroblasts to close the wound, demonstrating a damaged ability of cells to proliferate and migrate after infection (**Figure 4.8.**). No difference between male and female primary neonatal mouse lung fibroblasts with regard to the proliferation and migration of cells was observed.

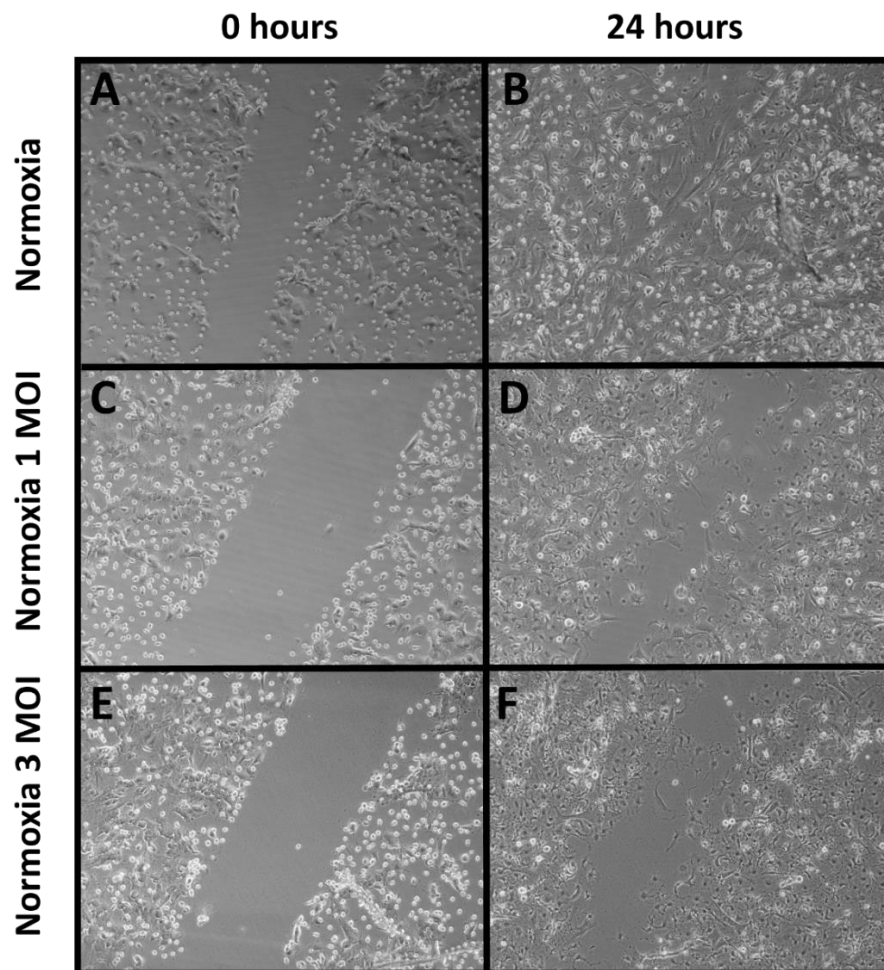


Figure 4.7. A wound healing “scratch” assay. Primary neonatal mouse lung fibroblasts.

Mouse primary fibroblasts were isolated from the lungs of newborn mice. Normoxia conditions without infection 0 h after scratch (A) and 24 hours after scratch (B), 0 hours after scratch (C) and 24 hours of MHV-68 1 MOI infection (D), 0 h after scratch (E) and 24 hours of MHV-68 3 MOI infection (F).

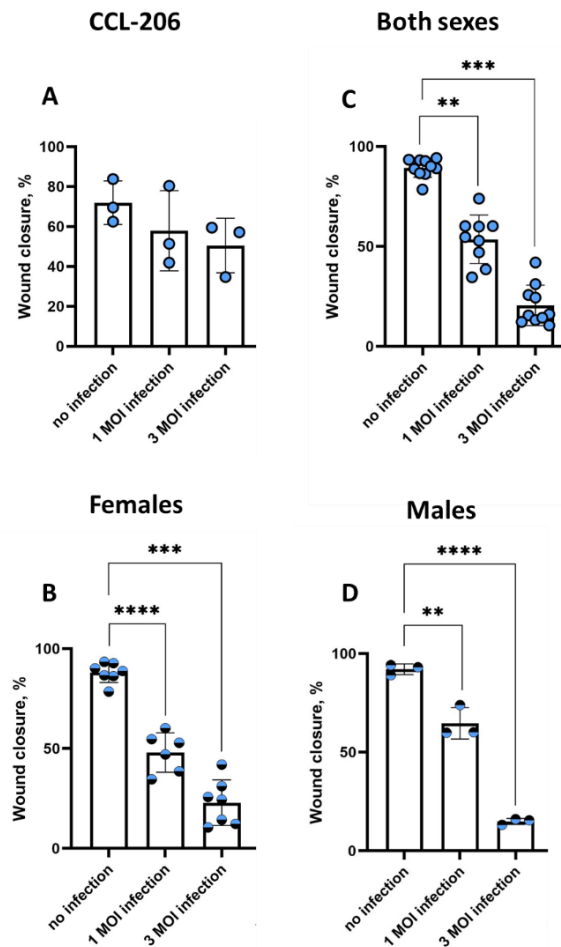


Figure 4.8. A wound healing “scratch” assay. Primary neonatal mouse lung fibroblasts.

MHV-68 infection of CCL-206 cells ($n=3$) (A) and mouse primary fibroblasts (B – both sexes, C – females ($n=3$), D – males ($n=4$)). Mouse primary fibroblasts were isolated from the lungs of newborn mice. In B, wound closure measurements are combined for both sexes. Statistical analysis: one-way ANOVA test with correction for multiple comparisons. * $p<0.05$, ** $p<0.01$, *** $p<0.001$, **** $p<0.0001$. A one-way ANOVA test with Tukey's test for multiple comparison correction was used when comparing more than two groups.

PCNA serves as a widely utilized indicator of cell proliferation due to its essential involvement in nucleic acid metabolism as part of the DNA replication and repair apparatus (de Oliveira, M. G. et al., 2008). I examined the expression of PCNA at both the mRNA and protein levels to evaluate changes in lung fibroblast proliferation. I performed immunoblotting analysis (Figure 4.9. A, C) and quantitative RT-PCR (qPCR) (Figure 4.9. D) on mouse primary fibroblasts after MHV-68 infection, but did not observe any statistically significant differences. These findings suggest that PCNA expression alone may not be sufficient to

estimate proliferation accurately due to the complexity of the regulating pathways involved. In addition, viability and proliferation of mouse primary lung fibroblasts were assessed using trypan blue staining (**Figure 4.9. B**) following MHV-68 infection. The results revealed a decrease in cell number after viral infection. No difference between female and male samples with regard to PCNA gene and protein expression and trypan blue staining was revealed.

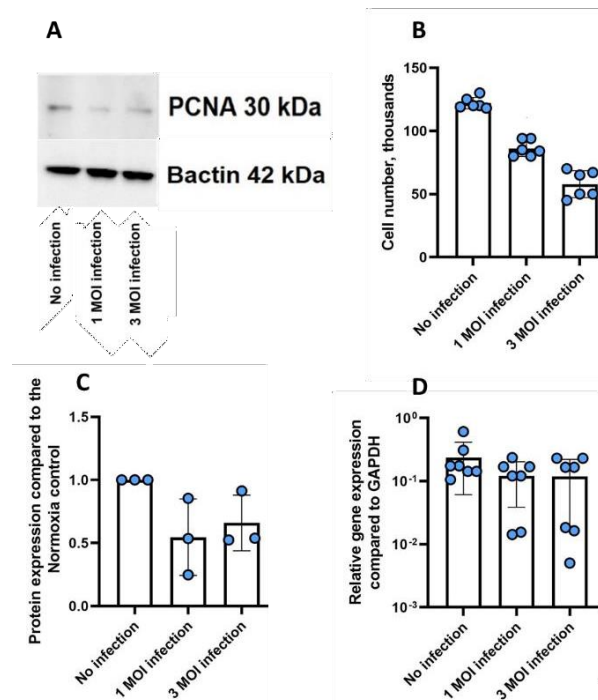


Figure 4.9. Cell number measurements and PCNA expression analysis in MHV-68 infected mouse primary fibroblasts.

Mouse primary fibroblasts were isolated from the lungs of newborn mice. A – immunoblot with PCNA and β actin antibodies, B – trypan blue analysis (n=6), C – quantification of Western Blot results (n = 3), D – PCNA gene expression (n=7). Representative immunoblot (A) and immunoblot analysis (C) were performed using protein lysates from mouse primary fibroblasts treated with room air ($\text{FiO}_2 = 0.21$) for 24 h and infected with MHV-68 for another 24 h. Trypan blue staining and manual counting (B) were performed to access the number of living cells. qPCR was used to estimate the mRNA expression of PCNA (D) - proliferating cell-nuclear antigen - in the whole cell lysates from mouse primary fibroblasts infected by MHV-68. Gapdh was used as a reference gene. One-way ANOVA test with multiple comparisons correction. *p-value < 0.05, ***p-value < 0.001.

Further, mouse primary fibroblast migration was evaluated using an *in vitro* migration assay (**Figure 4.10.**). Mouse primary fibroblasts in normoxia ($\text{FiO}_2 = 0.21$) infected with 3 MOI MHV-68 for 24 h were seeded onto special membranes. Chemoattractant, 10% FCS, was added to the lower compartment, whereas the

control wells had no FCS. Fluorescent measurements were taken 24 hours after infection.

Virus infection significantly decreased mouse primary lung fibroblast migration towards FCS (**Figure 4.10.**). No difference was revealed when comparing the migration of male and female primary neonatal mouse lung fibroblasts.

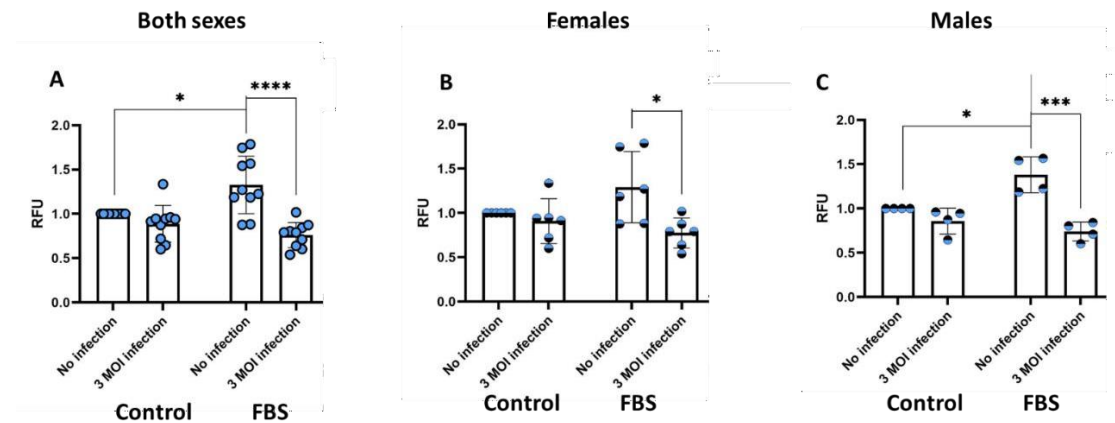


Figure 4.10. Quantitative analysis of infected mouse primary fibroblast migration.

Mouse primary fibroblasts were isolated from the lungs of $n = 6$ female (B) and $n = 4$ male (C) newborn mice. In A, migration measurements are combined for both sexes. One-way ANOVA test with multiple comparisons correction. *p-value < 0.05, **p-value < 0.01, ***p-value < 0.001, ****p-value < 0.0001.

Pulmonary fibrosis is a result of severe lung injury and is closely linked to inflammatory responses, particularly alveolar inflammation involving the contribution of alveolar macrophages (Wei Jie Huang & Xiao Xiao Tang, 2021). Viruses can induce pulmonary fibrosis through two pathways: i) Direct lung damage during viral infection activates the wound healing response, but persistent damage or abnormal healing can lead to fibrosis. ii) Viral infections can trigger immune-mediated injury, with inflammatory cells releasing various pro-inflammatory and pro-fibrotic factors, contributing to sustained lung damage and the development of pulmonary fibrosis. The myofibroblast marker *Acta2* is presented in pulmonary fibrosis and its gene expression is upregulated by HIV infection (Wei Jie Huang & Xiao Xiao Tang, 2021) and downregulated by SARS-CoV-2 infection (George, P. M. et al, 2022).

In the research of profibrotic genes, I studied *Acta2* gene expression in CCL-206 cells (**Figure 4.11. A**) and primary neonatal mouse lung fibroblasts (**Figure 4.11. B**). As revealed, CCL-206 cells and mouse primary fibroblasts

demonstrated the same *Acta2* gene expression level in the normoxia ($\text{FiO}_2 = 0.21$) with and without MHV-68 infection for 24 h. No difference in females and males with regard to *Acta2* gene expression was observed.

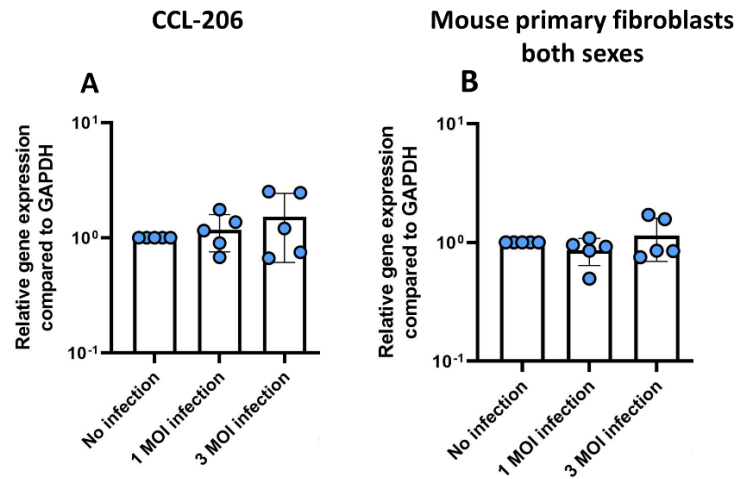


Figure 4.11. *Acta2* gene expression in CCL-206 (A) and primary neonatal mouse lung fibroblasts (B) after MHV-68 infection for 24 hours.

Mouse primary fibroblasts were isolated from the lungs of newborn mice ($n=5$), and expression levels were combined for both sexes. qPCR was used to quantify the mRNA expression of *Acta2* in mouse primary fibroblasts infected by MHV-68. One-way ANOVA test with multiple comparisons correction.

Animal studies have demonstrated that platelet-derived growth factor (PDGF) signaling is critical for normal alveolarization. *Pdgfra* gene expression is reduced in the lungs of Covid-19-infected human patient's (Islam, A. B. M. M. K. et al, 2020). Therefore, I investigated the impact of MHV-68 infection for 24 h in normoxia ($\text{FiO}_2 = 0.21$) on mRNA and protein expression of PDGF-R α in mouse primary fibroblasts (**Figure 4.12.**). MHV-68 infection with a MOI of 3 significantly decreased mRNA expression levels. Female and male samples did not show any difference between each other in PDGF-R α gene and protein expression.

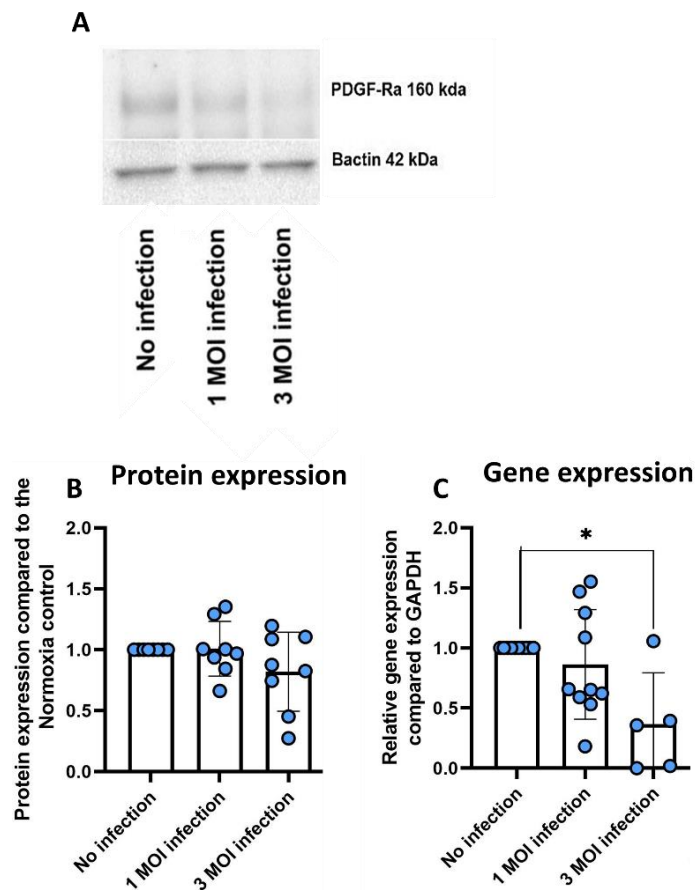


Figure 4.12. PDGF-R α protein expression (A, B) and *Pdgfra* gene expression (C) in primary neonatal mouse lung fibroblasts after MHV-68 infection.

Mouse primary fibroblasts were isolated from the lungs of newborn mice (n=5), and expression levels were combined for both sexes. Representative immunoblot (A) was performed using protein lysates from mouse primary fibroblasts infected by MHV-68 for 24 h. qPCR was used to quantify the mRNA expression of *Pdgfra* (n = 5 - 10/group) in mouse primary fibroblasts infected by MHV-68. One-way ANOVA test with multiple comparisons correction. *p-value < 0.05.

Vascular endothelial growth factor (VEGF) is crucial for vascular development and is generated by various cell types such as endothelial cells, fibroblasts, macrophages, smooth muscle cells, neutrophils, and platelets (Shams et al., 2022). VEGF-A specifically promotes angiogenesis and holds a vital role in lung development and homeostasis. The available data, which is both limited and controversial, indicates that VEGF might play dual roles in several lung diseases, such as pulmonary fibrosis, with both pathological and protective implications (Sergei P. Atamas, 2017).

To investigate the effects of MHV-68 infection under normoxia (FiO₂ = 0.21) conditions on *Vegf* gene expression in CCL-206 cells and mouse primary fibroblasts, the mRNA level of *Vegf* was analyzed (**Figure 4.13.**). The results

showed that viral infection increased *Vegf* expression in both CCL-206 and mouse primary lung fibroblasts. No sex-related differences in the *Vegf* gene expression in infected mouse primary fibroblasts were revealed.

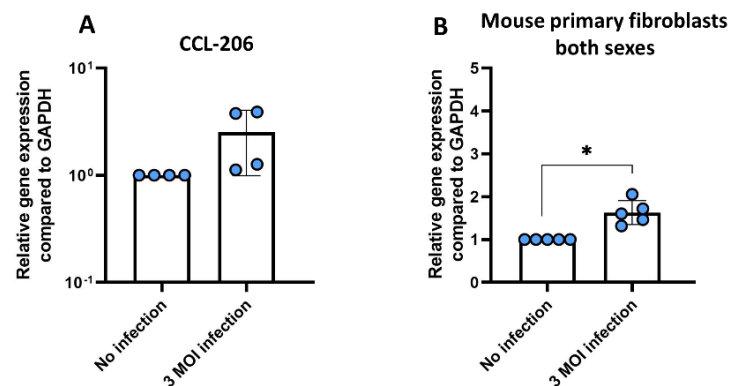


Figure 4.13. *Vegf* gene expression in CCL-206 (A) and primary neonatal mouse lung fibroblasts (B) after MHV-68 infection.

Mouse primary fibroblasts were isolated from the lungs of newborn mice (n=5), and expression levels were combined for both sexes. qPCR was used to quantify the mRNA expression of *Vegf* in mouse primary fibroblasts after MHV-68 infection. One-way ANOVA test with multiple comparisons correction.

4.1.2. Effects of in vitro MHV-68 infection in mouse primary fibroblasts and CCL-206 cells following pre-exposure with hyperoxia or pretreatment with TGF- β

The pathogenesis of bronchopulmonary dysplasia (BPD) results in persistent detrimental effects that may stay throughout an individual's life. Although viral infections are known to determine the long-term outcome of BPD, the impact of pre-existing hyperoxia conditions, simulating BPD conditions, on viral infection remains uncertain and requires further investigation.

Pathogenic viruses exhibit varying adaptability to oxygen levels to perform efficient host infection. The host immune response against viruses entails a coordinated effort between the innate and adaptive immune systems, which recognize diverse viral components and connect an effective defense against infection. Numerous investigations have previously confirmed that elevated oxygen levels are linked to harmful consequences, encompassing disruptions in immune responses, irregular metabolic function, and changes in both

hemodynamics and alveolar barrier function (Kumar, V. H. S. et al, 2017; Gan, E. S. and Ooi, E. E., 2020). Utilizing an increased amount of oxygen to address systemic hypoxia in individuals with severe COVID-19 pneumonia could potentially be linked to the deterioration of lung damage and the advancement toward the onset of severe Acute Respiratory Distress Syndrome (ARDS) (Dushianthanm A. et al, 2023).

To distinguish the unique impact of hyperoxia exposure, primary neonatal mouse lung fibroblasts derived from the pulmonary tissue of neonatal mice (comprising an equal gender distribution of three females and three males, with ages ranging from 5 to 7 DOL) were subjected to hyperoxia exposure ($FiO_2 = 0.4$) for 24 hours and infection with recombinant MHV-68 expressing GFP, at multiplicity of infection (MOI) values of 0, 0.1, 1, and 3 (**Figure 4.14.**) for another 24 hours. Infection of the hyperoxia-exposed primary neonatal lung fibroblasts with MHV-68 resulted in a dose-dependent increase of the GFP expression, indicating the increasing rate of virus infection. No sex-related differences concerning fibroblast infection in hyperoxia conditions were observed (**Figure 4.14. B and C**).

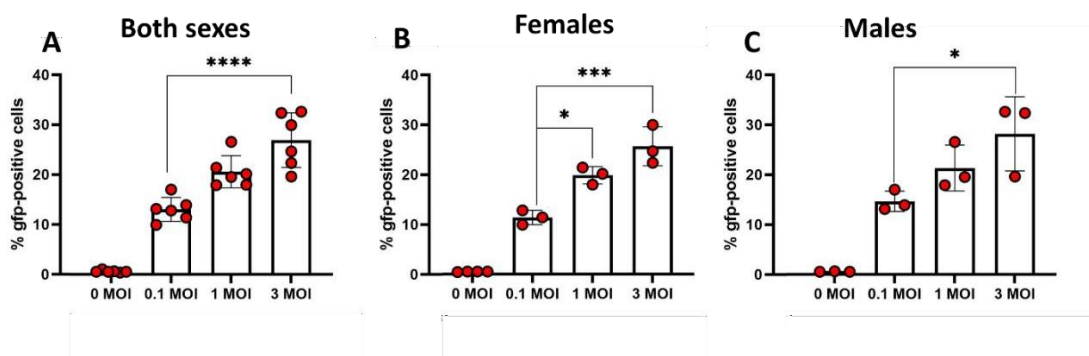


Figure 4.14. Recombinant MHV-68 expressing GFP infects primary neonatal mouse lung fibroblasts with prior hyperoxia exposure.

MHV-68 infection rates in mouse primary lung fibroblasts with prior exposure to hyperoxia ($FiO_2 = 0.4$) for 24 h. Mouse primary fibroblasts were isolated from the lungs of $n=3$ female (B) and $n=3$ male (C) newborn mice. In A, expression levels are combined for both sexes. One-way ANOVA test with multiple comparisons correction. * p -value < 0.05, *** p -value < 0.001, **** p -value < 0.0001.

To investigate whether hyperoxia exposure ($FiO_2 = 0.4$) for 24 hours influences viral replication in vitro, I infected hyperoxia-exposed primary neonatal mouse lung fibroblasts with MHV-68 (0,1 MOI). Cells and supernatants were frozen, thawed twice, and collected, centrifuged, and assessed for virus concentration

by plaque assay at 0 h, 24 h, 48 h, 72 h, and 96 h post-infection. The replication rate of the virus was determined by analysis of log₁₀-transformed PFU number measured in the samples after centrifugation (n = 5 – 6) plotted over time. Hyperoxia exposure for 24 h significantly diminished viral replication in primary neonatal lung fibroblasts compared with normoxia (FiO₂ = 0.21) (**Figure 4.15.**). No sex-related differences concerning changes in the virus replication curve were observed.

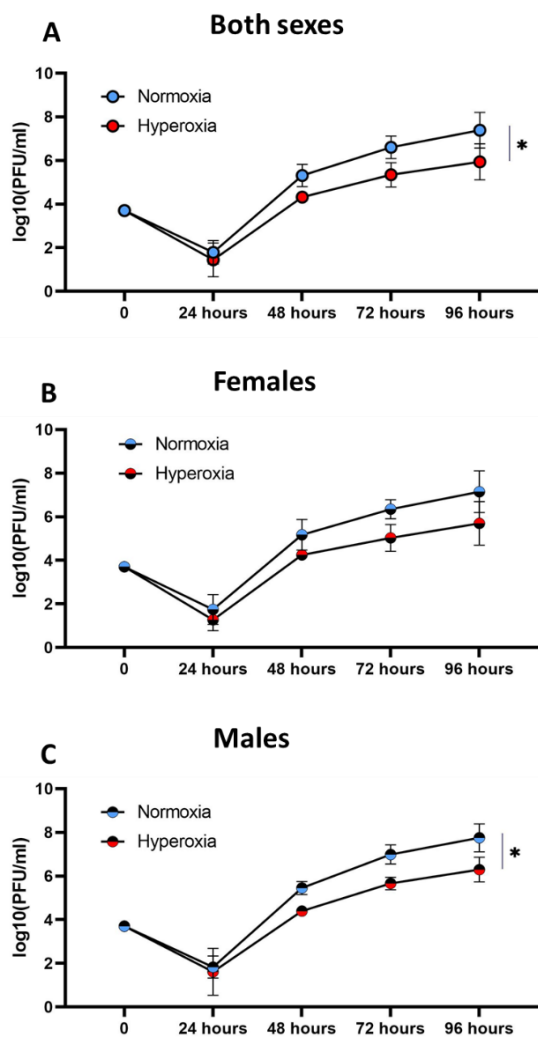


Figure 4.15. MHV-68 replication in primary neonatal mouse lung fibroblasts under hyperoxia exposure (FiO₂ = 0.4).

Mouse primary fibroblasts were isolated from the lungs of n = 5 – 6 female (B) and n = 5 – 6 male (C) newborn mice. In A, replication curves are combined for both sexes. The replication rate of the virus was determined by analysis of log₁₀-transformed PFU number measured in the samples after centrifugation and plotted over time. Normoxia served as a control for hyperoxia exposure. One-way ANOVA test with multiple comparisons correction. *p-value < 0.05.

Hyperoxia exposure ($\text{FiO}_2 = 0,4$) did not induce a change in the metabolic activity of CCL-206 cells (**Figure 4.16. A**), however, MHV-68 infection (MOI of 3) of the hyperoxia exposed CCL-206 cells led to a significant decrease compared with infected samples under normoxia ($\text{FiO}_2 = 0.21$) conditions. Mouse primary fibroblasts demonstrated no changes in metabolic activity in female and male samples when exposed to hyperoxia with or without following MHV-68 infection (**Figure 4.16. B, C, and D**).

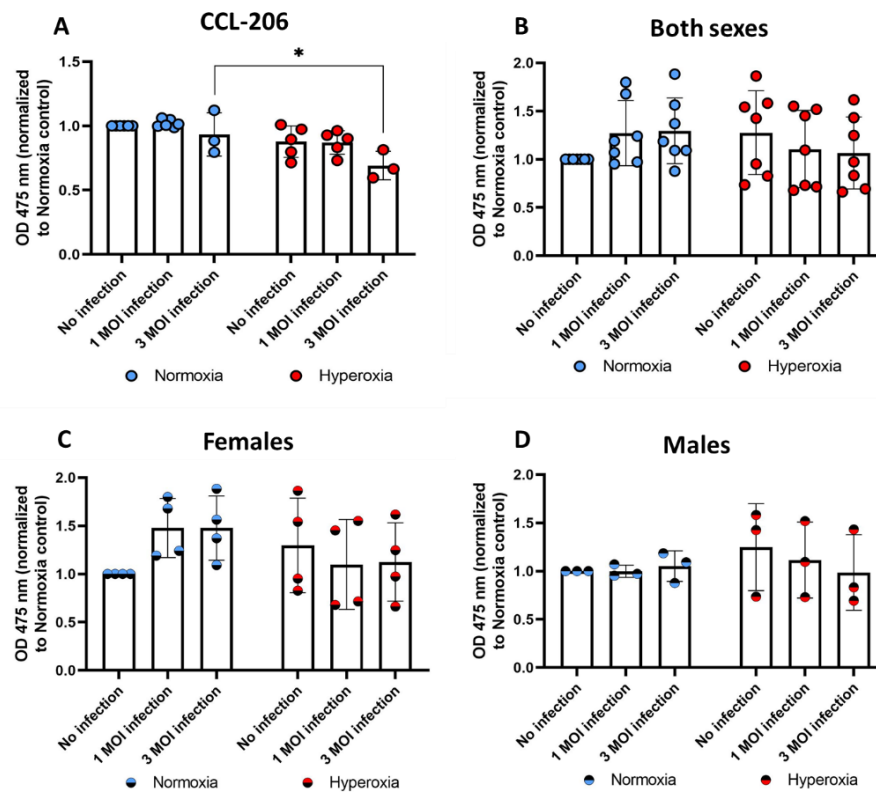


Figure 4.16. MHV-68 infection and hyperoxia exposure did not change metabolic activity in the primary neonatal mouse lung fibroblasts.

Impact of MHV-68 infection on the metabolic activity of CCL-206 cells and mouse primary fibroblasts after hyperoxia exposure ($\text{FiO}_2 = 0.4$) (A – CCL-206 ($n=4$), B – both sexes, C – females ($n=4$), D – males ($n=5$)). Mouse primary fibroblasts were isolated from the lungs of female (C) and male (D) newborn mice. In B, metabolic activities are combined for both sexes. Normoxia served as a control for hyperoxia exposure. One-way ANOVA test with multiple comparisons correction. * p -value < 0.05 .

Mouse primary fibroblasts exposed to hyperoxia for 24 hours did not show alterations in early apoptotic processes. However, subsequent MHV-68 infection (MOI of 1) of primary fibroblasts led to a significant increase in Annexin V binding 72 hours after infection, indicating the mutual reinforcement of hyperoxia

exposure and virus infection (**Figure 4.17. A**). Primary lung fibroblasts obtained from female mice consistently exhibited a higher signal intensity after hyperoxia exposure for 24 hours with following MHV-68 infection than primary lung fibroblasts obtained from male mice (**Figure 4.17. B and C**).

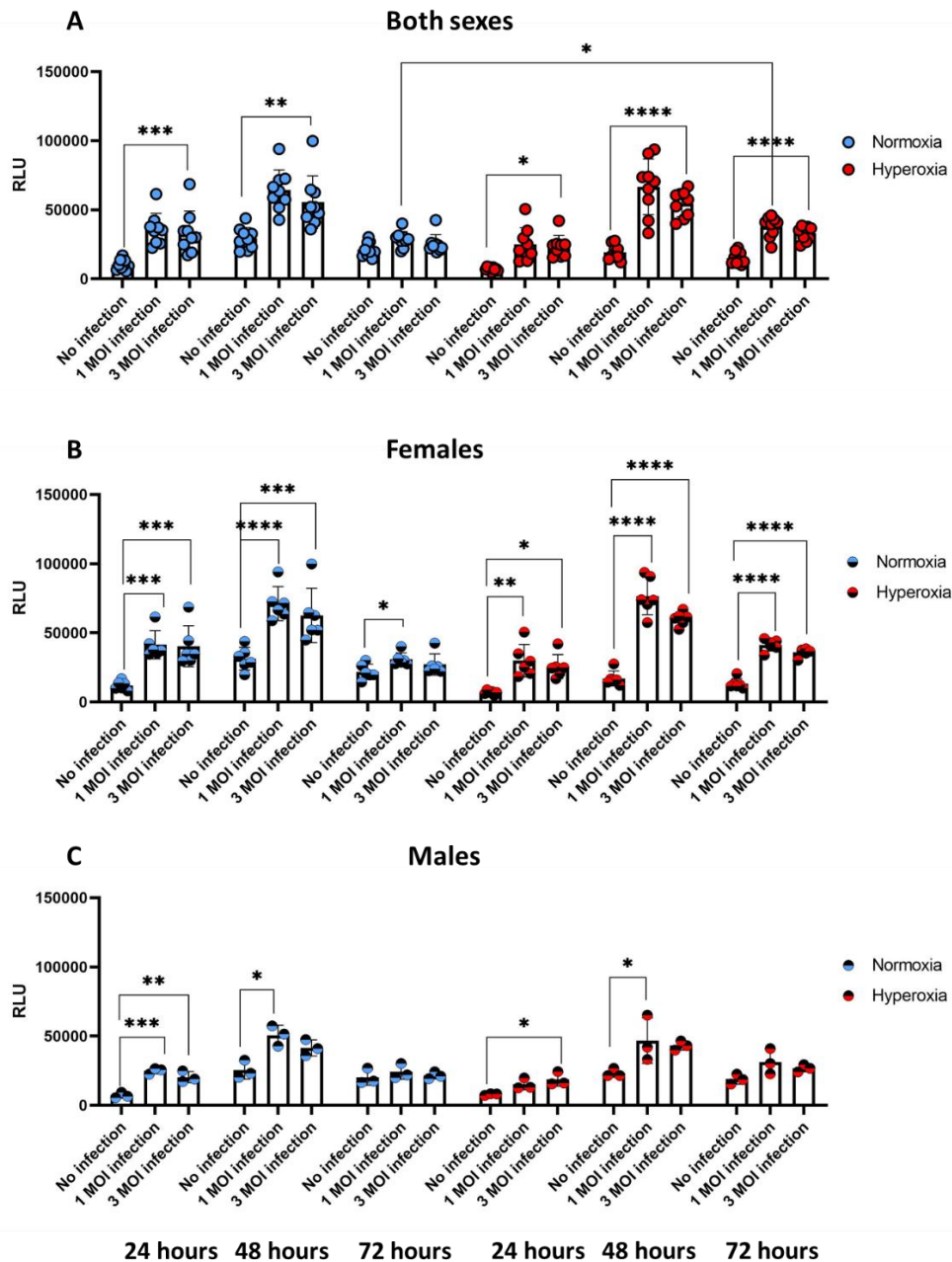


Figure 4.17. Annexin V binding after MHV-68 infection with or without primary exposure to hyperoxia of primary neonatal mouse lung fibroblasts.

Mouse primary fibroblasts were isolated from the lungs of $n = 6$ female (B) and $n = 3$ male (C) newborn mice. In A, expression levels are combined for both sexes. Normoxia served as a control for hyperoxia exposure. RLU: relative luminescence units. One-way ANOVA test with multiple comparisons correction. *p-value < 0.05, **p-value < 0.01, ***p-value < 0.001, ****p-value < 0.0001.

I also investigated Caspase 3/7 activity in mouse primary neonatal lung fibroblasts after hyperoxia exposure ($\text{FiO}_2 = 0.4$) for 24 hours, with or without following MHV-68 infection for 24 hours (**Figure 4.18. B, C, and D**).

Hyperoxia exposure alone increased Caspase 3/7 activity in CCL-206 cells (**Figure 4.18. A**), but significantly reduced it in mouse primary fibroblasts from both female and male samples (**Figure 4.18. C and D**). The combined effect of hyperoxia exposure and MHV-68 infection caused similar effects as hyperoxia exposure alone in both CCL-206 and mouse primary fibroblasts. No sex-related differences with regard to Caspase 3/7 activity were observed.

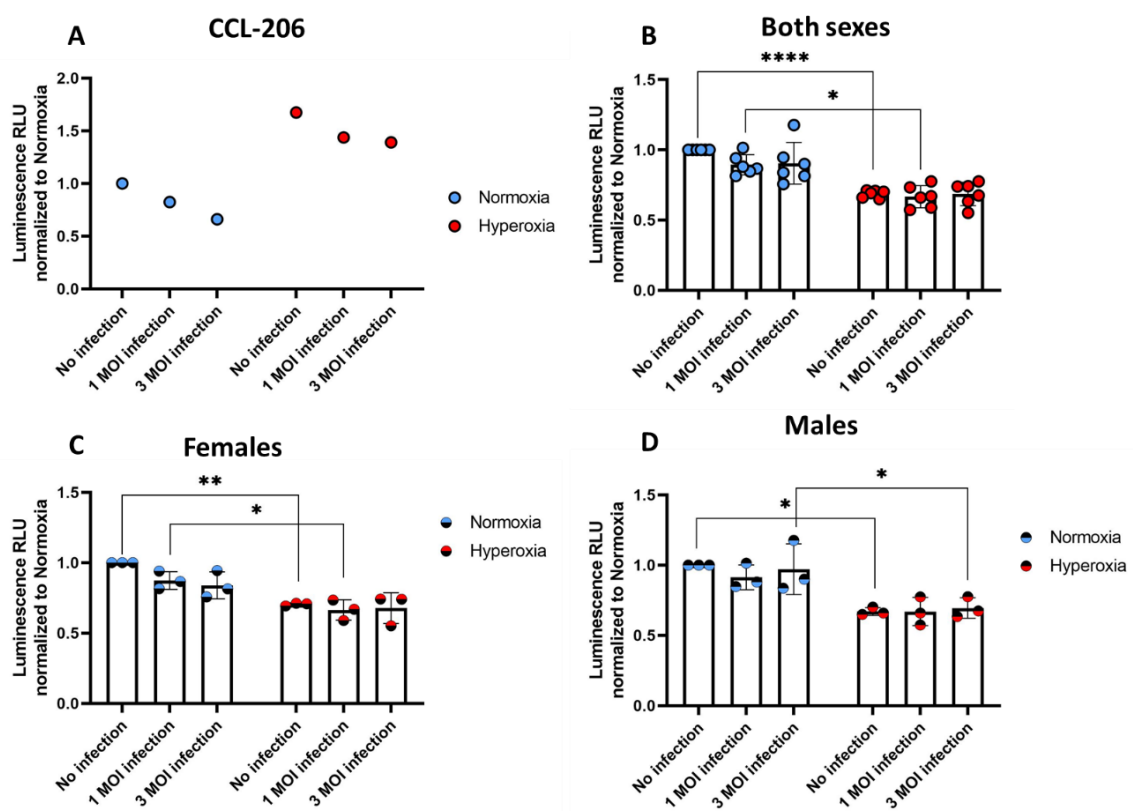


Figure 4.18. Caspase 3/7 activity after MHV-68 infection in primary neonatal mouse lung fibroblasts in normoxia ($\text{FiO}_2 = 0.21$) or hyperoxia ($\text{FiO}_2 = 0.4$).

(A) Activity of the Caspase 3/7 (Caspase Glo 3/7) in CCL-206 cells after hyperoxia exposure and MHV-68 infection ($n=1$). Mouse primary lung fibroblasts were isolated from $n = 3$ female (C) and $n = 3$ male (D) newborn mice. In B, measured Caspase 3/7 activities are combined for both sexes. Normoxia served as a control for hyperoxia exposure. One-way ANOVA test with multiple comparisons correction. *p-value < 0.05, **p-value < 0.01, ***p-value < 0.001, ****p-value < 0.0001.

Hyperoxia exposure ($\text{FiO}_2 = 0.4$) with or without following MHV-68 infection significantly reduced the intensity of mouse primary fibroblasts necrosis after 24

hours compared to normoxia ($\text{FiO}_2 = 0.21$) (**Figure 4.19.**). However, at the other time points, infected samples demonstrated significant increase in the necrosis level. Male and female primary lung fibroblasts demonstrated the same necrosis level throughout the experiment.

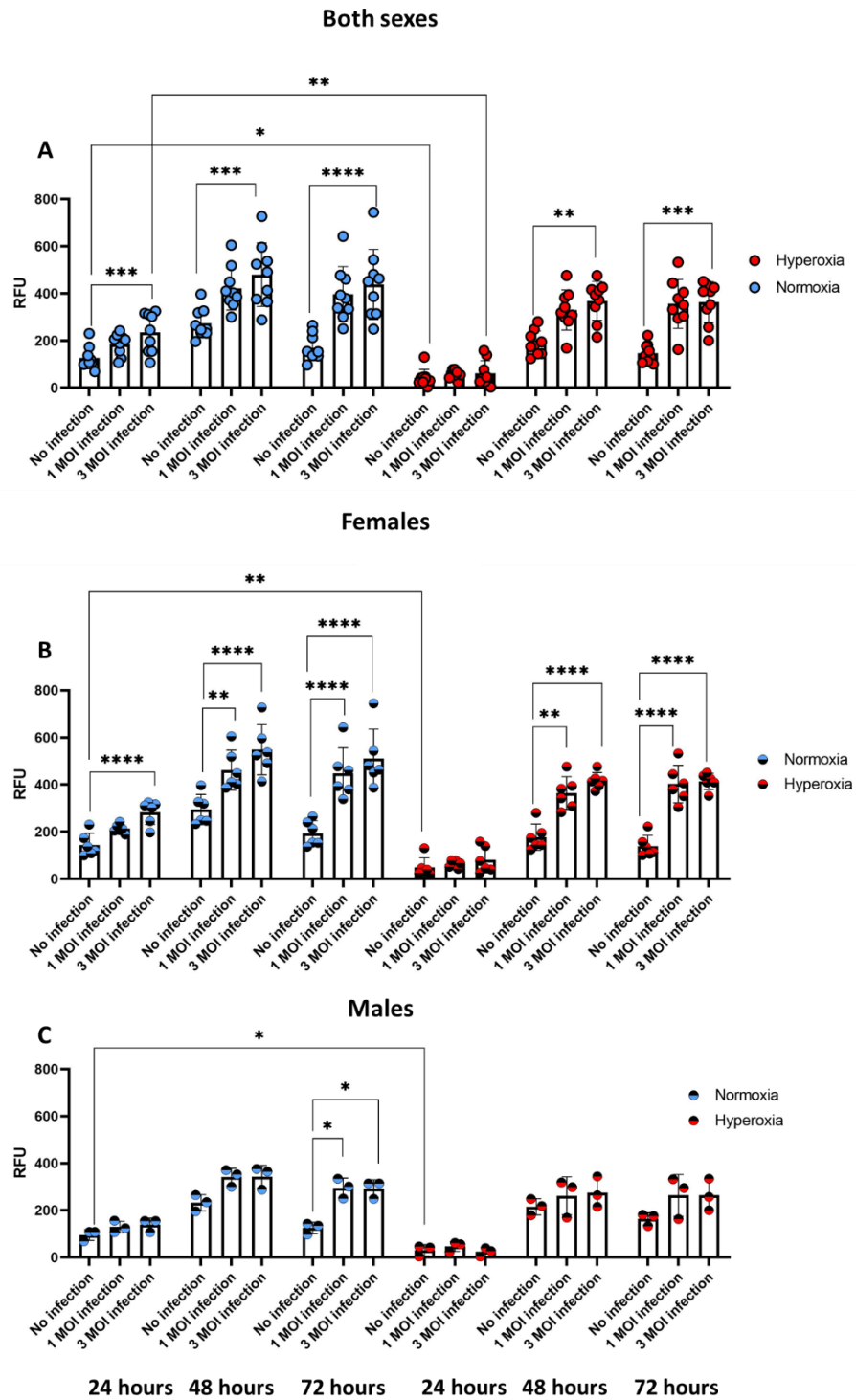


Figure 4.19. Necrosis after hyperoxia exposure ($\text{FiO}_2 = 0.4$) for 24 hours and MHV-68 infection for 24 hours of primary neonatal mouse lung fibroblasts.

Mouse primary fibroblasts were isolated from the lungs of $n = 6$ female (B) and $n = 3$ male (C) newborn mice. In A, necrosis measurements are combined for both sexes. Normoxia served as a control for hyperoxia exposure. RFU: relative fluorescence units. One-way ANOVA test with multiple comparisons correction. * p -value < 0.05 , ** p -value < 0.01 , *** p -value < 0.001 , **** p -value < 0.0001 .

Next, I investigated how hyperoxia exposure for 24 hours with or without following MHV-68 infection can impact the proliferation and migration of primary neonatal mouse lung fibroblasts. **Figure 4.20.** displayed neonatal mouse primary fibroblasts after MHV-68 infection with or without prior hyperoxia exposure ($\text{FiO}_2 = 0.4$) for 24 h. Hyperoxia exposure alone did not change the cell morphology. Visually cellular deformations in the double-hit model closely resembled those observed in the singular viral infection scenario.

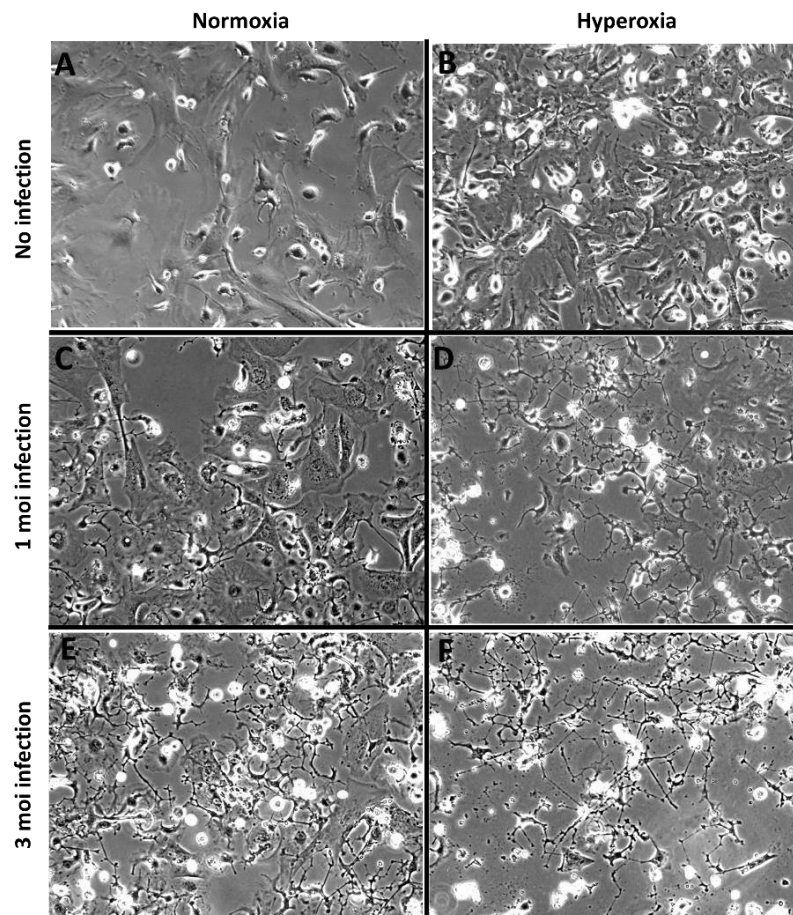


Figure 4.20. Images of primary neonatal mouse lung fibroblasts.

Mouse primary fibroblasts were isolated from the lungs of a newborn mouse. Normoxia served as a control for hyperoxia exposure. Normoxia conditions without infection (A), 24 hours of MHV-68 1 MOI infection (C), and 3 MOI infection (E). 24 hours of hyperoxia exposure ($\text{FiO}_2 = 0.4$) without infection (B), 24 hours of MHV-68 1 MOI infection (D), and 3 MOI infection (F).

Following exposure to hyperoxia with or without following MHV-68 infection, the ability of CCL-206 cells and primary fibroblasts to proliferate and migrate was observed to be the same as that of cells exposed to 21% oxygen conditions in the wound healing “scratch” assay (**Figure 4.21.** and **Figure 4.22.**). No difference was observed between male and female primary neonatal mouse lung fibroblasts with regard to the proliferation and migration of cells.

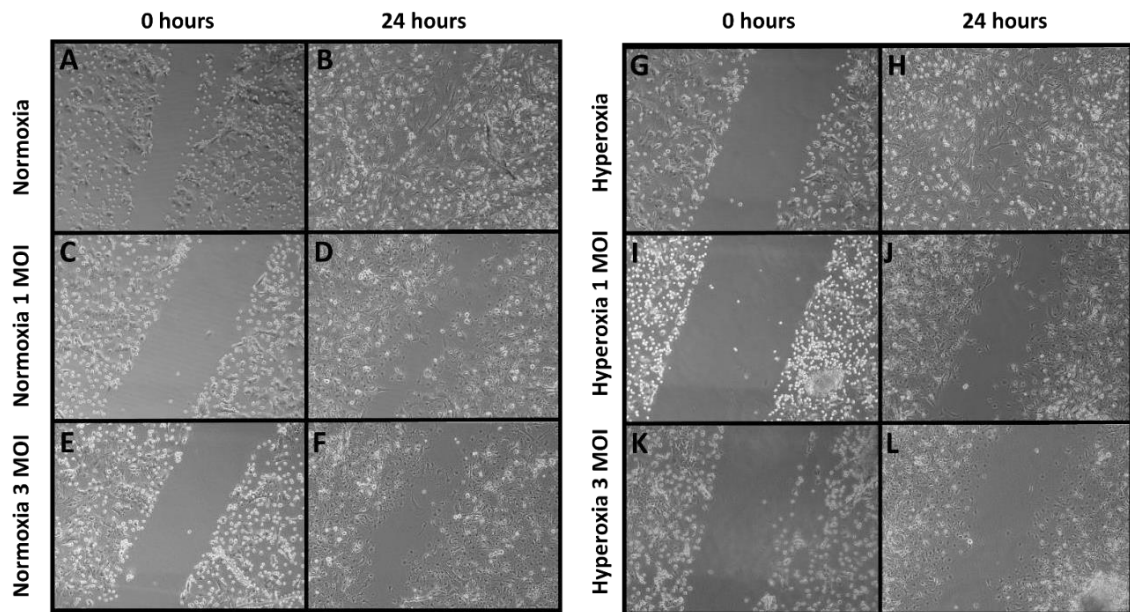


Figure 4.21. A wound healing “scratch” assay. Primary neonatal mouse lung fibroblasts.

Mouse primary fibroblasts were isolated from the lungs of a newborn mouse. Normoxia served as a control for hyperoxia exposure. Normoxia conditions without infection 0 h after scratch (A) and 24 h after scratch (B), 0 h after scratch (C) and 24 h of MHV-68 1 MOI infection (D), 0 h after scratch (E) and 24 h of MHV-68 3 MOI infection (F). 24 h of hyperoxia exposure ($FiO_2 = 0.4$) without infection 0 h after scratch (G) and 24 h after scratch (H), 0 h after scratch (I) and 24 h of MHV-68 1 MOI infection (J), 0 h after scratch (K) and 24 h of MHV-68 3 MOI infection (L).

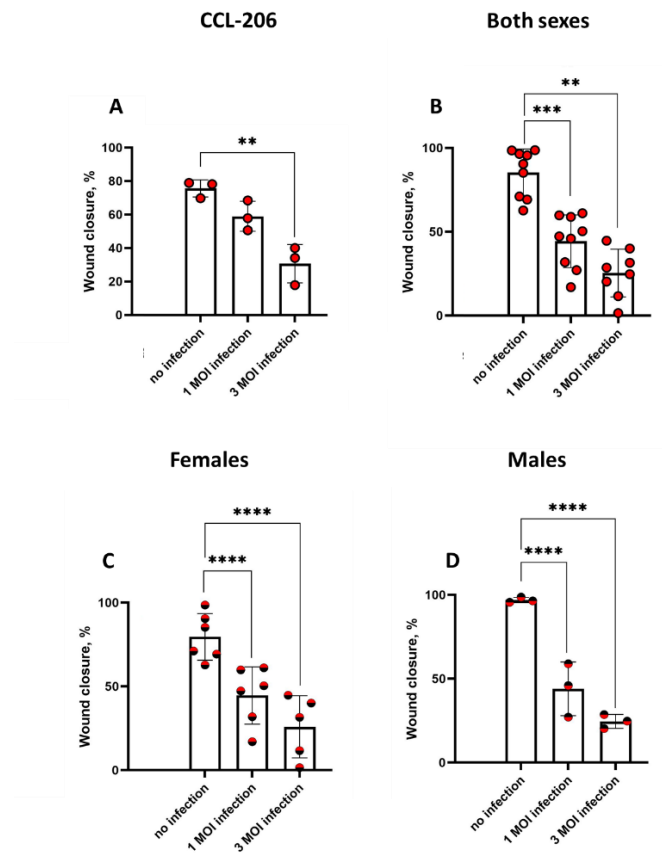


Figure 4.22. A wound healing “scratch” assay. Primary neonatal mouse lung fibroblasts.

MHV-68 infection in CCL-206 cells ($n=3$) (A) and mouse primary fibroblasts with prior hyperoxia exposure (B – both sexes are combined, C – females ($n=6$), D – males ($n=3$)). Mouse primary fibroblasts were isolated from the lungs of female (C) and male (D) newborn mice. In B, wound closure measurements are combined for both sexes. One-way ANOVA test with multiple comparisons correction. * p -value < 0.05, ** p -value < 0.01, *** p -value < 0.001, **** p -value < 0.0001.

I performed immunoblotting analysis (**Figure 4.23. A and C**) and quantitative RT-PCR (qPCR) (**Figure 4.23. D**) on mouse primary fibroblasts after hyperoxia exposure ($FiO_2 = 0.4$) for 24 hours and MHV-68 infection. Primary fibroblast viability and proliferation were assessed using trypan blue staining (**Figure 4.23. B**) with following MHV-68 infection. The results revealed a significant decrease in cell number after hyperoxia exposure, and both factors combined. No difference between female and male samples with regard to PCNA gene and protein expression and trypan blue counting was revealed.

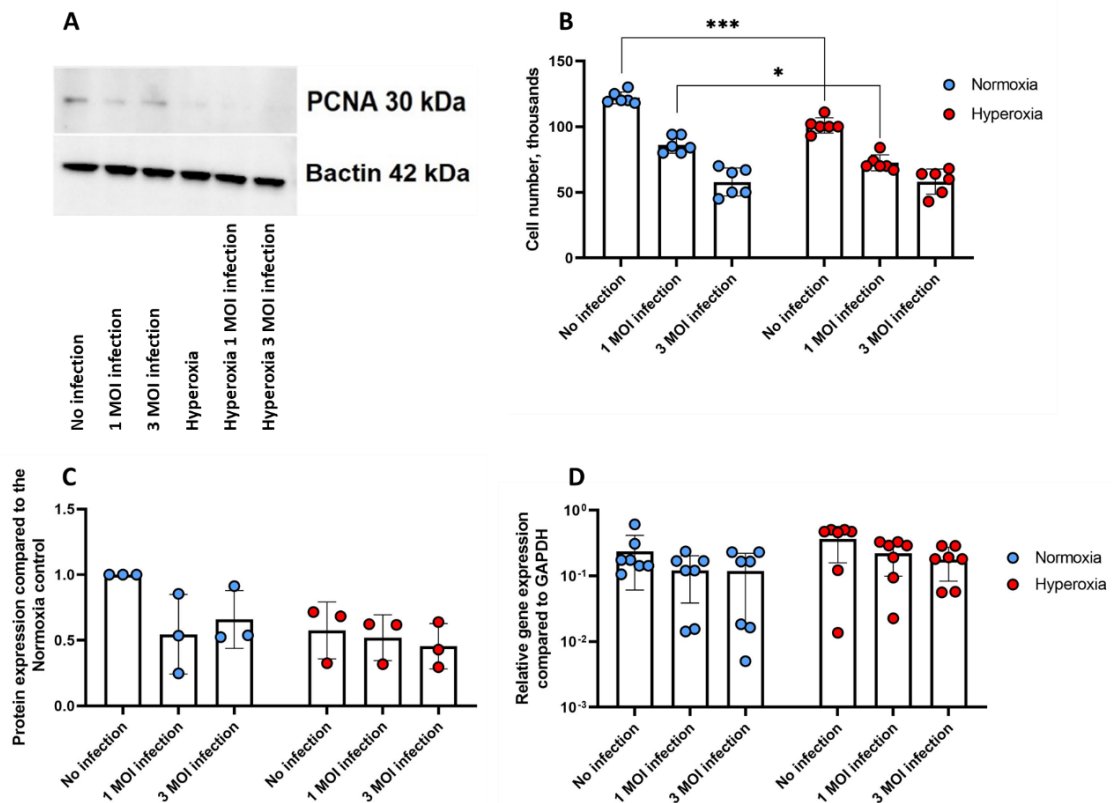


Figure 4.23. Cell number measurements and PCNA expression analysis in hyperoxia exposed mouse primary fibroblasts with or without following MHV-68 infection.

Mouse primary fibroblasts were isolated from the lungs of newborn mice. A – immunoblot with PCNA and β actin antibodies, B – trypan blue analysis (n=6), C – quantification of Western Blot results (n = 3), D – PCNA gene expression (n=7). Representative immunoblot (A) and immunoblot analysis (C) were performed using protein lysates from mouse primary fibroblasts treated with O_2 ($FiO_2 = 0.4$) or room air ($FiO_2 = 0.21$) for 24 hours. Trypan blue staining and manual counting (B) were performed to access the number of living cells. qPCR was used to estimate the mRNA expression of PCNA (D) - proliferating cell-nuclear antigen - in the whole cell lysates from mouse primary fibroblasts treated with oxygen and infected by MHV-68. Gapdh was used as a reference gene. Normoxia served as a control for hyperoxia exposure. One-way ANOVA test with multiple comparisons correction. *p-value < 0.05, ***p-value < 0.001, ****p-value < 0.0001.

Hyperoxia exposure ($FiO_2 = 0.4$) for 24 hours with following MHV-68 infection significantly decreased cell migration as measured by CytoSelect 96-well Cell Migration Assay Kit, whereas hyperoxia exposure alone did not change cell migration (**Figure 4.24.**). No difference was revealed when comparing the migration of male and female primary neonatal mouse lung fibroblasts.

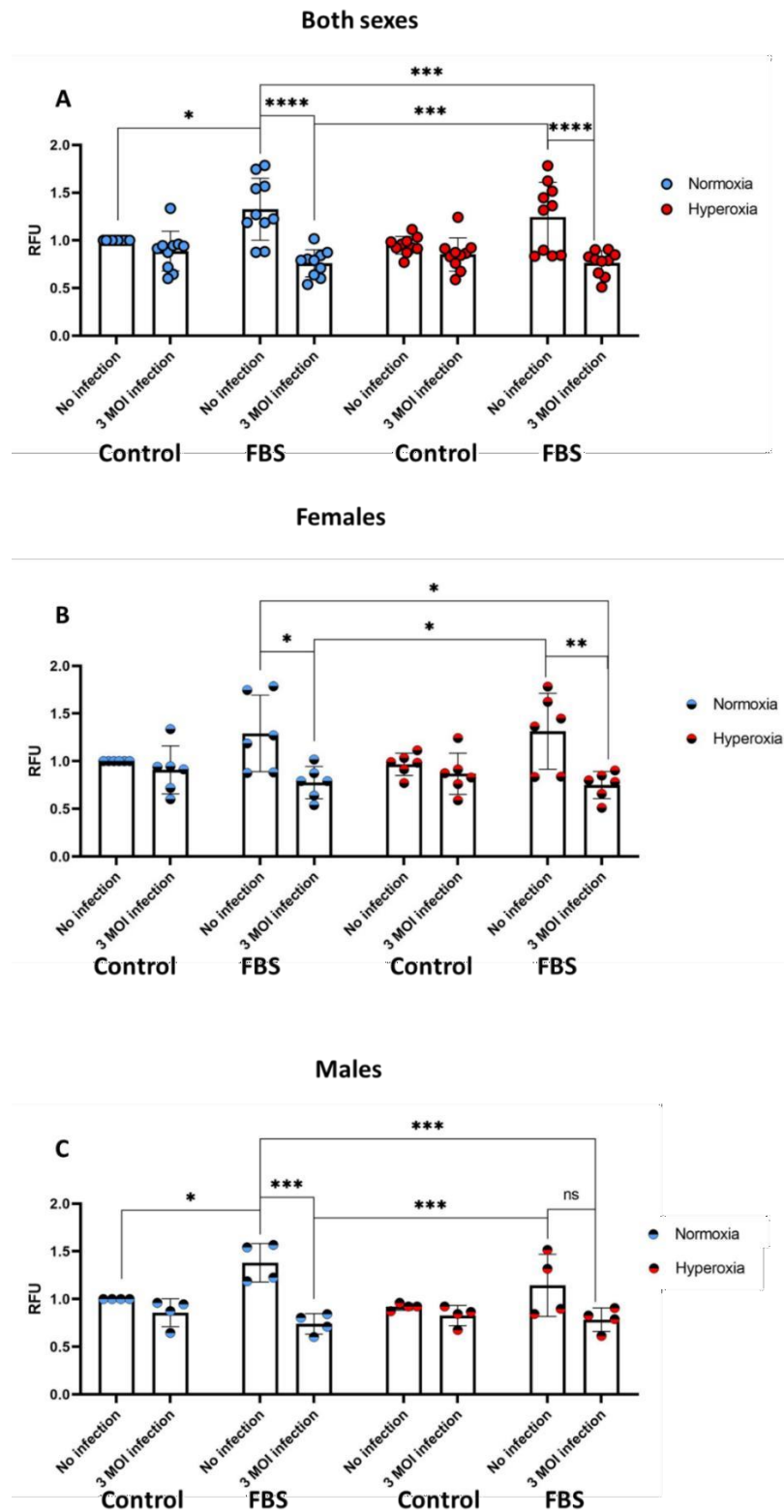


Figure 4.24. Quantitative analysis of hyperoxia exposed and infected mouse primary fibroblast migration.

Mouse primary fibroblasts were isolated from the lungs of $n = 6$ female (B) and $n = 4$ male (C) newborn mice. In A, migration measurements are combined for both sexes. Normoxia served as a control for hyperoxia exposure. One-way ANOVA test with multiple comparisons correction. * p -value < 0.05 , ** p -value < 0.01 , *** p -value < 0.001 , **** p -value < 0.0001 .

BPD is characterized by thickening of the alveolar septa, decreased secondary septal formation, and myofibroblast differentiation (Popova, A. P., 2013). Several studies have suggested myofibroblast investigation as a part of BPD research due to the changes in the fibroblast population during hyperoxia injury (Riccetti, M. R., et al., 2022). According to the literature, *Acta2* expression (myofibroblast marker) is upregulated in an *in vivo* hyperoxia mouse model (Sucre, J. M. S, et al., 2020).

In the research of profibrotic genes, I studied *Acta2* gene expression in CCL-206 cells (Figure 4.25. A) and primary neonatal mouse lung fibroblasts (Figure 4.25. B). As revealed, mouse primary fibroblasts and CCL-206 cells demonstrated the same *Acta2* gene expression level after normoxia and hyperoxia exposure with or without following MHV-68 infection. No difference in females and males concerning the *Acta2* gene expression was observed.

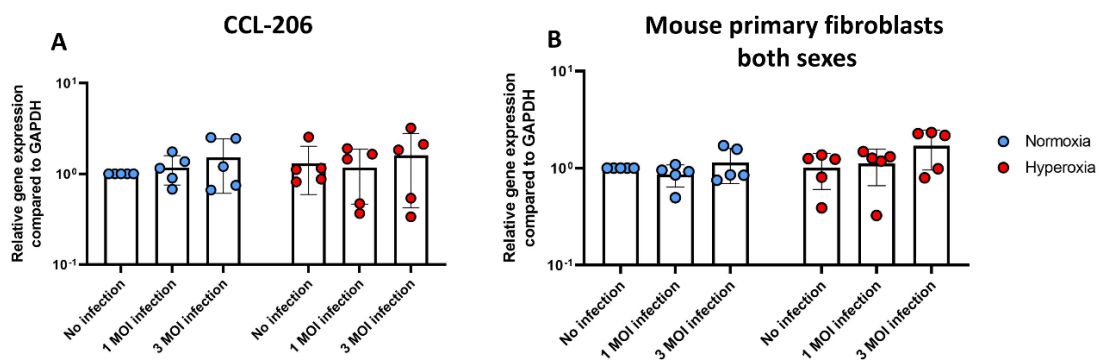


Figure 4.25. *Acta2* gene expression in CCL-206 (A) and primary neonatal mouse lung fibroblasts (B) after hyperoxia exposure and MHV-68 infection.

(A) *Acta2* gene expression in CCL-206 cells after hyperoxia exposure and MHV-68 infection (n=5). Mouse primary fibroblasts were isolated from the lungs of newborn mice (n=5), and expression levels were combined for both sexes (B). Normoxia served as a control for hyperoxia exposure. qPCR was used to quantify the mRNA expression of *Acta2* in mouse primary fibroblasts exposed to O₂ or RA. One-way ANOVA test with multiple comparisons correction.

Research involving animals has indicated the importance of platelet-derived growth factor (PDGF) signaling in normal alveolarization. It has been observed that the expression of PDGFR is diminished in mesenchymal stromal cells (MSCs) of neonatal lungs from infants who later develop bronchopulmonary dysplasia (Popova, A. P. et al., 2014). Moreover, exposure to severe hyperoxia

treatment ($\text{FiO}_2 > 0.7$) has been linked to a reduction in the population of fibroblasts expressing $\text{Pdgf-R}\alpha$ (Riccetti et al., 2022; Sucre et al., 2020).

Therefore, I investigated the impact of hyperoxia exposure with or without following MHV-68 infection on mRNA and protein expression of PDGF- $\text{R}\alpha$ in mouse primary fibroblasts (**Figure 4.26.**). Hyperoxia exposure impact on *Pdgfra* gene expression and PDGF- $\text{R}\alpha$ protein levels was insignificant. However, both hyperoxia exposure and viral infection together significantly decreased protein expression levels. Female and male samples did not show any difference in PDGF- $\text{R}\alpha$ gene and protein expression.

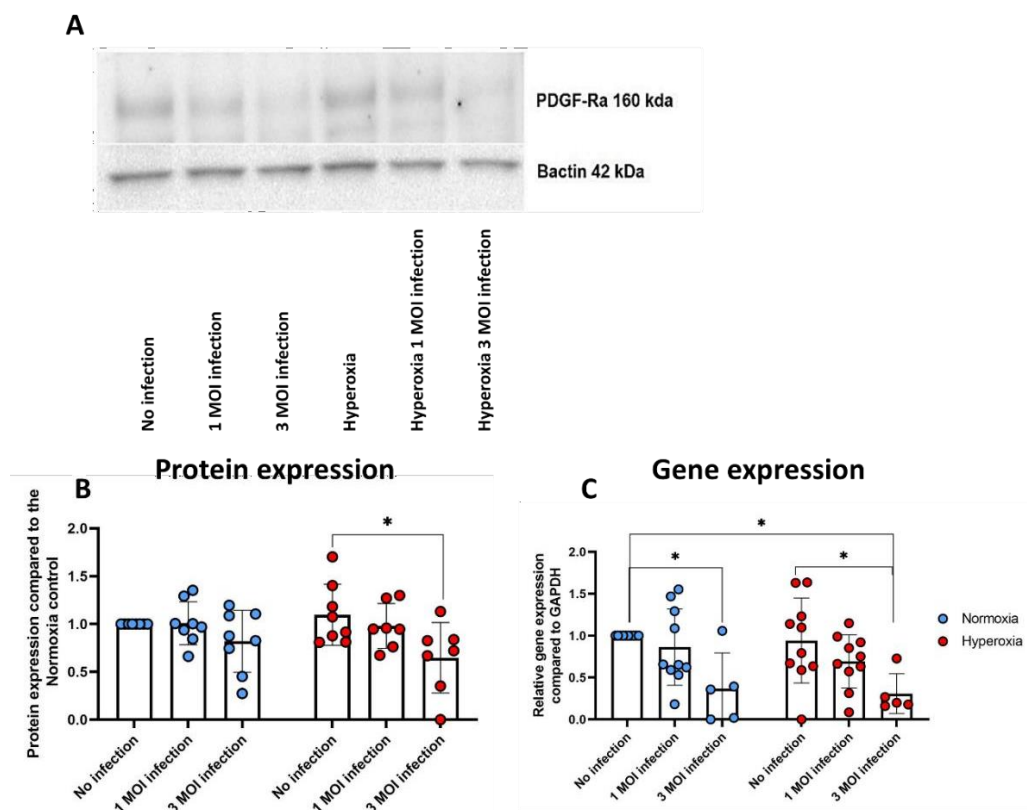


Figure 4.26. PDGF- $\text{R}\alpha$ protein expression (A) and PDGF- $\text{r}\alpha$ gene expression (B) in primary neonatal mouse lung fibroblasts after hyperoxia exposure and MHV-68 infection.

Mouse primary fibroblasts were isolated from the lungs of newborn mice ($n=5-10$), and expression levels were combined for both sexes. Normoxia served as a control for hyperoxia exposure. Representative immunoblot (A) was performed using protein lysates from mouse primary fibroblasts infected by MHV-68 and treated with O_2 ($\text{FiO}_2 = 0.4$) or room air (RA; $\text{FiO}_2 = 0.21$) for 24 h. Densitometry quantification (B) of PDGF- $\text{R}\alpha$ showed decreased expression in the O_2 group ($n = 7 - 8/\text{group}$) in infected samples. qPCR was used to quantify the mRNA expression of *Pdgfra* ($n = 5 - 10/\text{group}$) in mouse primary fibroblasts exposed to O_2 or RA. One-way ANOVA test with multiple comparisons correction. * p -value < 0.05 .

Studies have shown that patients with BPD have lower *Vegf* expression levels in the early stages of the disease (Meller, S. et al, 2012). To investigate the effects of hyperoxia exposure ($FiO_2 = 0.4$) for 24 hours with or without following MHV-68 infection on *Vegf* gene expression in CCL-206 cells and mouse primary fibroblasts, the mRNA level of *Vegf* was analyzed (**Figure 4.27. A and B**). The results showed that hyperoxia exposure and viral infection independently increased *Vegf* expression in both cell types. However, there was no synergistic effect when hyperoxia and virus infection were combined. Female and male samples did not show any difference in *Vegf* gene expression.

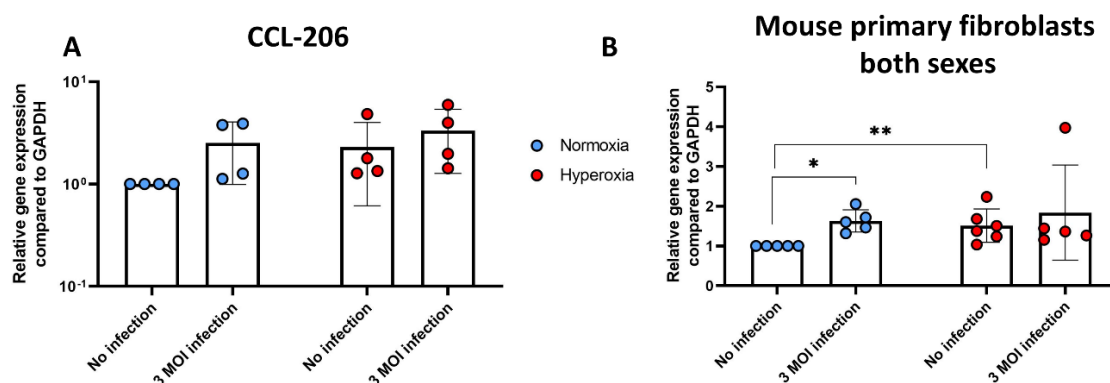


Figure 4.27. *Vegf* gene expression in CCL-206 cells (A) and primary neonatal mouse lung fibroblasts (B) after hyperoxia exposure and MHV-68 infection.

(A) *Vegf* gene expression in CCL-206 cells after hyperoxia exposure and MHV-68 infection (n=4). Mouse primary fibroblasts were isolated from the lungs of newborn mice (n=5), and expression levels were combined for both sexes (B). Normoxia served as a control for hyperoxia exposure. qPCR was used to quantify the mRNA expression of *Vegf* in mouse primary fibroblasts exposed to O₂ or RA. One-way ANOVA test with multiple comparisons correction.

In infected epithelial cells from bronchial brushings obtained from donors, TGF β treatment promotes Rhinovirus replication (Davies, D. E. et al., 2012) and increases HIV-1 replication (Unwalla, H. J. et al., 2019). Studies have demonstrated increased expression of TGF β in BPD experimental models (Bhandari V. et al., 2015, Prajakta Oak and Anne Hilgendorff, 2017). I, therefore, investigated whether TGF β stimulation for 24 hours prior to the infection with MHV-68 affects infection rates (**Figure 4.28.**). Primary neonatal mouse lung fibroblasts derived from the pulmonary tissue of neonatal mice (comprising an equal gender distribution of three females and three males, with ages ranging from 5 to 7 DOL) were subjected to infection with recombinant MHV-68

expressing GFP, at multiplicity of infection (MOI) values of 0, 0.1, 1, and 3 (Figure 4.28.). The infection was performed in cells with and without prior incubation with TGF β (5ng/ml).

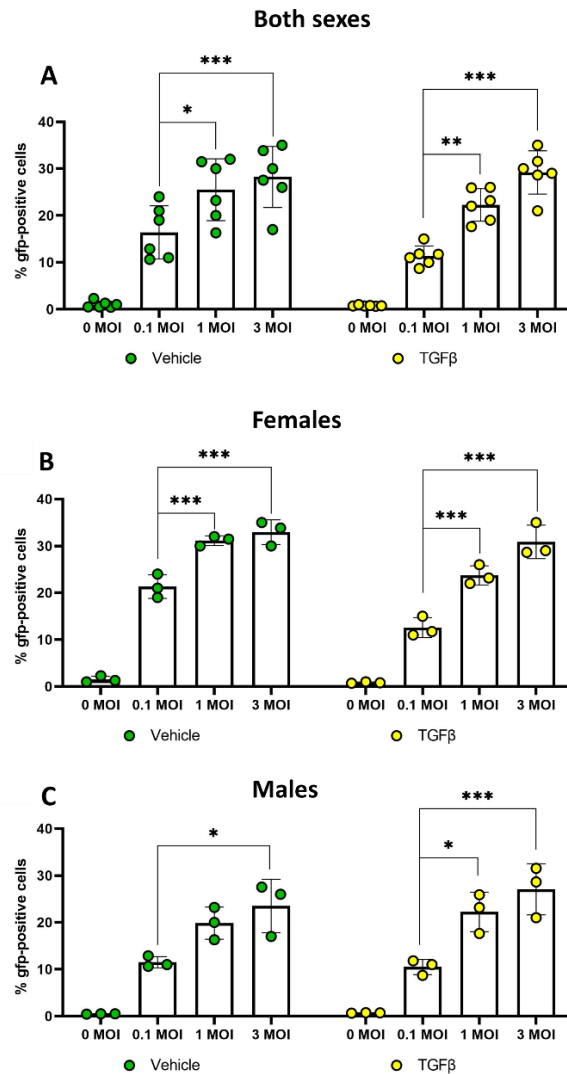


Figure 4.28. Recombinant MHV-68 expressing GFP infects primary neonatal mouse lung fibroblasts.

MHV-68 infection rates in mouse primary lung fibroblasts with or without prior incubation with TGF β for 24 hours. Mouse primary fibroblasts were isolated from the lungs of $n=3$ female (B) and $n=3$ male (C) newborn mice. In A, expression levels are combined for both sexes. Vehicle treatment served as a control for TGF β . One-way ANOVA test with multiple comparisons correction. * p -value < 0.05, *** p -value < 0.001, **** p -value < 0.0001.

Incubation of the primary neonatal lung fibroblasts with TGF β with following MHV-68 infection resulted in a dose-dependent increase of the GFP expression, indicating the increasing rate of virus infection. No sex-related differences concerning fibroblast infection were observed (Figure 4.28. A and B).

To investigate whether incubation for 24 h with TGF β (5 ng/ml) influences viral replication *in vitro*, I infected TGF β -treated primary neonatal mouse lung fibroblasts with MHV-68 (0,1 MOI) for 24 hours. TGF β treatment for 24 hours did not impact viral replication (**Figure 4.29.**). No sex-related differences in virus replication were observed.

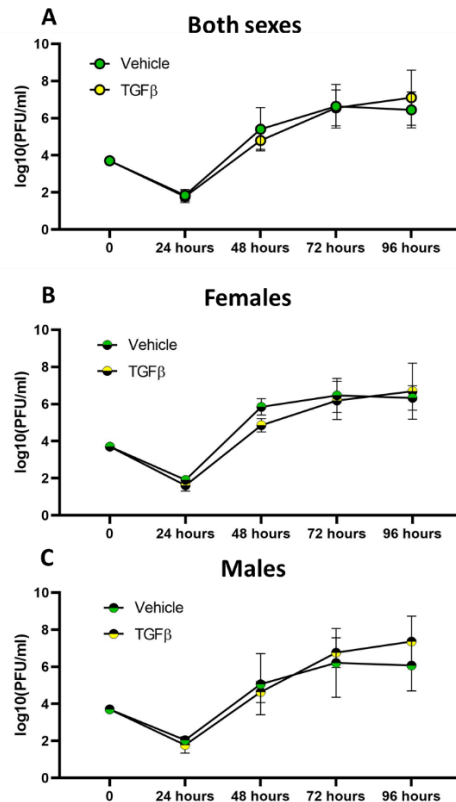


Figure 4.29. MHV-68 replication in primary neonatal mouse lung fibroblasts after TGF β treatment.

Mouse primary fibroblasts were isolated from the lungs of $n = 5 - 6$ female (B) and $n = 5 - 6$ male (C) newborn mice. In A, replication curves are combined for both sexes. The replication rate of the virus was determined by analysis of log₁₀-transformed PFU number measured in the supernatant of the cells and plotted over time. Vehicle treatment served as a control for TGF β treatment. One-way ANOVA test with multiple comparisons correction. * p -value < 0.05.

To understand how MHV-68 infection and TGF β treatment act on lung fibroblasts, I investigated the metabolic activity in CCL-206 cells and mouse primary fibroblasts undergoing MHV-68 infection after TGF β treatment (5 ng/ml, 24 h) in $n = 3 - 5$ independent experiments (**Figure 4.30.**).

TGF β treatment with or without prior virus infection did not change metabolic activity in CCL-206 cells (**Figure 4.30. A**). In primary neonatal mouse lung

fibroblasts, TGF β treatment for 24 h increased metabolic activity in female samples (**Figure 4.30. C**) but did not change it in males (**Figure 4.30. D**).

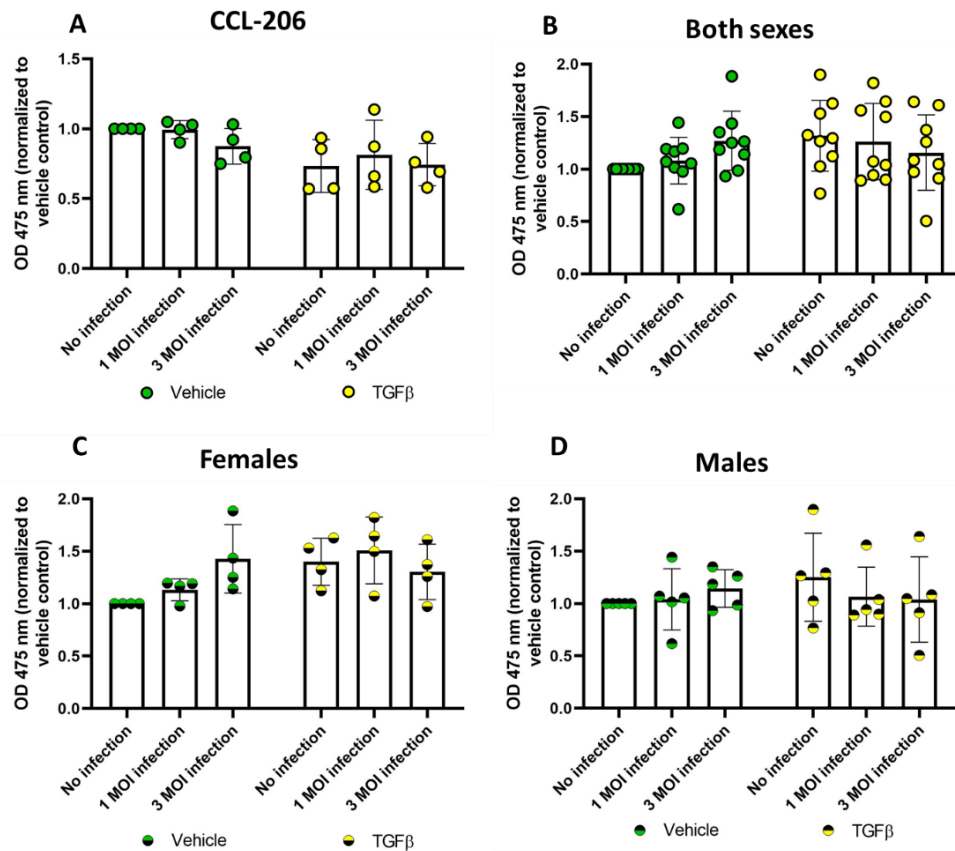


Figure 4.30. MHV-68 infection or TGF β treatment did not change or increase metabolic activity in the primary neonatal mouse lung fibroblasts.

Impact of MHV-68 infection on the metabolic activity of CCL-206 cells and mouse primary fibroblasts after TGF β treatment (A – CCL-206 (n = 3-5), B – both sexes, C – females (n = 4), D – males (n = 5)). Mouse primary fibroblasts were isolated from the lungs of female (C) and male (D) newborn mice. In B, metabolic activities are combined for both sexes. Vehicle treatment served as a control for TGF β treatment accordingly. One-way ANOVA test with multiple comparisons correction. *p-value < 0.05.

Next, I investigated Annexin V (RealTime-Glo™ Annexin V Apoptosis and Necrosis Assay) binding in mouse primary fibroblasts to assess the effects of MHV-68 infection and TGF β treatment throughout 24, 48, and 72 hours (**Figure 4.31.**).

TGF β treatment rendered distinct effects on Annexin V binding compared to hyperoxia exposure (**Figure 4.17.**). When administered alone, it resulted in a reduction of Annexin V binding in female mouse primary fibroblasts 72 hours post-treatment. Subsequent infection with MHV-68 induced a significant increase in Annexin V binding 24 hours post-infection. Remarkably, the combination of

TGFβ treatment and virus infection continued to amplify Annexin V binding in females, whereas, in the Vehicle control male samples, binding remained unchanged after infection. Furthermore, 72 hours post-infection, early apoptosis processes were significantly diminished in both treated and control samples, with no discernible sex-related differences in Annexin V binding changes. As TGFβ treatment demonstrated different effects on apoptosis when compared to hyperoxia exposure, its influence on the Caspase 3/7 pathway was not examined.

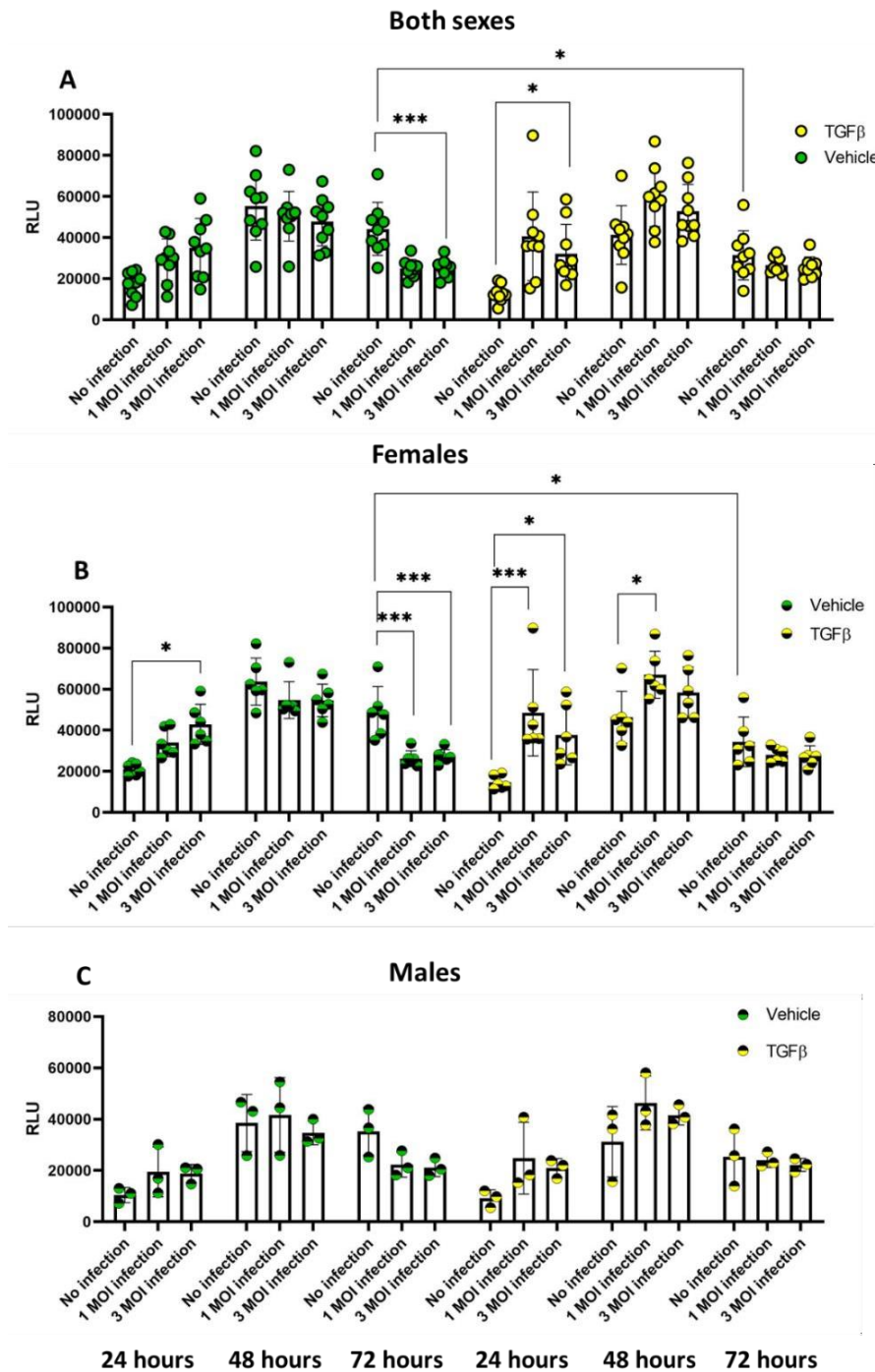


Figure 4.31. Annexin V binding after MHV-68 infection and TGF β treatment of primary neonatal mouse lung fibroblasts.

Mouse primary fibroblasts were isolated from the lungs of n = 6 female (B) and n = 3 male (C) newborn mice. In A, expression levels are combined for both sexes. Vehicle treatment served as a control for TGF β treatment. RLU: relative luminescence units. One-way ANOVA test with multiple comparisons correction. *p-value < 0.05, **p-value < 0.01, ***p-value < 0.001, ****p-value < 0.0001.

Next, I investigated necrosis (RealTime-Glo™ Annexin V Apoptosis and Necrosis Assay) in primary neonatal mouse lung fibroblasts to assess the effects of TGF β treatment and MHV-68 infection throughout 24, 48, and 72 hours. No significant influence of TGF β treatment on necrosis of mouse primary fibroblasts was observed (**Figure 4.32.**). At the same time, MHV-68 infection significantly increased necrosis in both Vehicle and TGF β treated samples. Male and female primary lung fibroblasts demonstrated the same necrosis level after TGF β treatment with or without following MHV-68 infection.

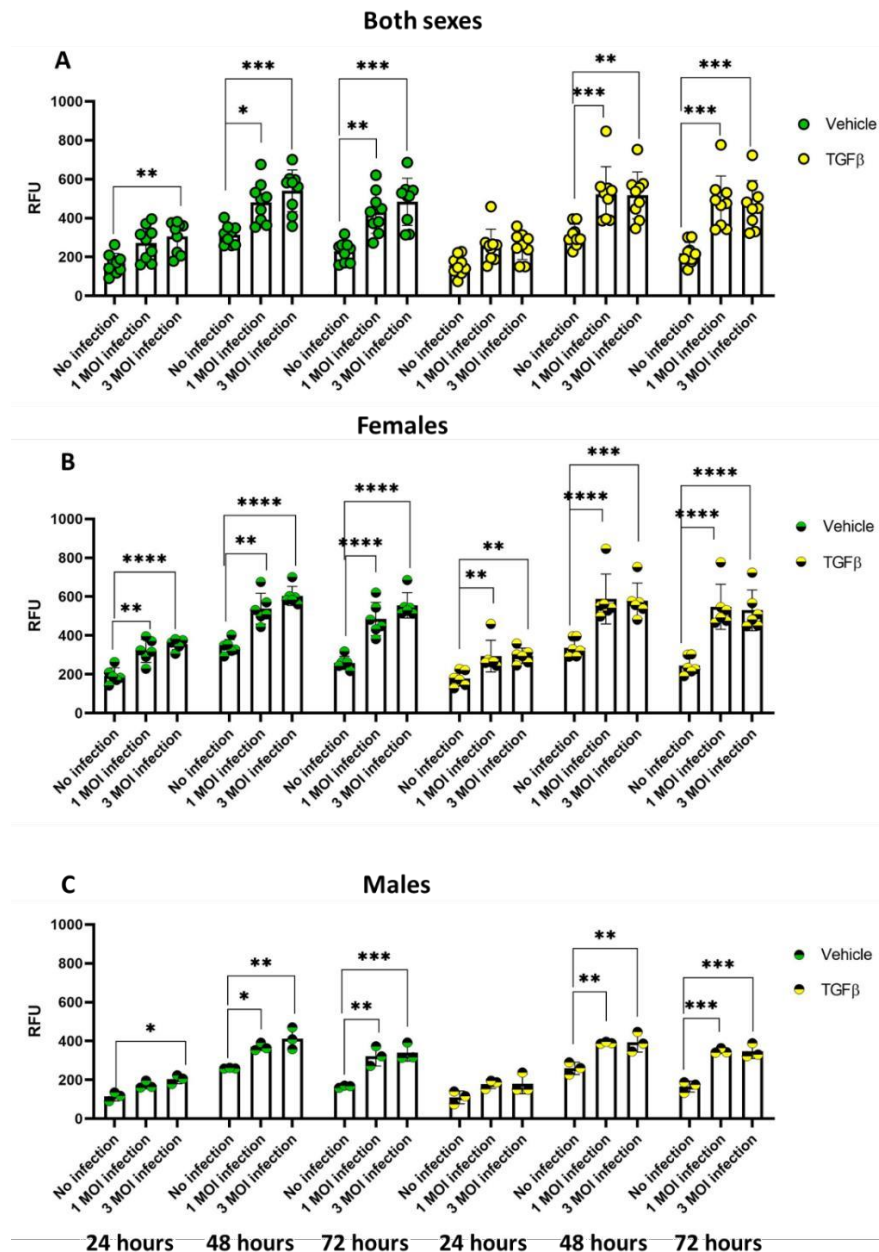


Figure 4.32. Necrosis after MHV-68 infection and TGFβ treatment of primary neonatal mouse lung fibroblasts.

Mouse primary fibroblasts were isolated from the lungs of $n = 6$ female (B) and $n = 3$ male (C) newborn mice. In A, necrosis measurements are combined for both sexes. Vehicle treatment served as a control for TGFβ treatment. RFU: relative fluorescence units. One-way ANOVA test with multiple comparisons correction. * p -value < 0.05 , ** p -value < 0.01 , *** p -value < 0.001 , **** p -value < 0.0001 .

TGFβ treatment of mouse primary fibroblasts did not change cell proliferation and migration capability (**Figure 4.33.**). MHV-68 infection after TGFβ treatment did not change the wound healing process. No difference was observed between

male and female primary neonatal mouse lung fibroblasts concerning the proliferation and migration of cells.

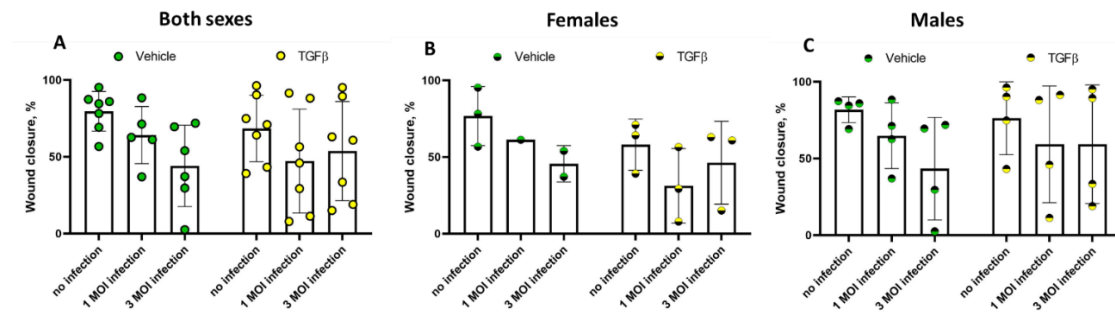


Figure 4.33. A wound healing “scratch” assay. Primary neonatal mouse lung fibroblasts.

MHV-68 infection of mouse primary fibroblasts after TGFβ treatment (A – both sexes, B – females (n=3), C – males (n=4)). Mouse primary fibroblasts were isolated from the lungs of female (B) and male (C) newborn mice. In A, wound closure measurements are combined for both sexes. Vehicle treatment served as a control for TGFβ treatment accordingly. Statistical analysis: one-way ANOVA test with correction for multiple comparisons. *p<0.05, **p<0.01, ***p<0.001, ****p<0.0001.

4.2. *In vivo* MHV-68 infection of C57BL/6J mice after exposure to hyperoxia

4.2.1. Establishment of a new *in vivo* experimental model to study viral infection and hyperoxia exposure

The *in vitro* experiments showed that primary neonatal mouse lung fibroblasts infected with MHV-68 with or without prior exposure to hyperoxia (FiO₂ = 0.4, 24 hours) demonstrated changed migration, apoptosis, proliferation, altered metabolic activity and *Pdgfra*, *Acta2* and *Pcna* gene expression. Therefore, I proposed that hyperoxia treatment impact on the neonatal lung structure, rendering it more susceptible to subsequent injury. To test this hypothesis, I exposed newborn mice to 40% O₂ for 24 hours at the age of 5 – 7 days (**first hit**) and then returned them to room air. After eight days of recovery, mice were randomly assigned to receive intranasal inoculation with MHV-68 (**second hit**) or did not receive any treatment as control. The mice were sacrificed on days 3, 6, 10, 28, and 4 – 6 months after the initial O₂ treatment (**Figure 4.34. A**).

First, I determined the body weight of all C57BL/6 mice on the day of analysis. The data illustrated that mice infected with MHV-68, whether exposed to hyperoxia or not, exhibited weights within the accepted range for their age, as depicted in **Figure 4.34. B and C**.

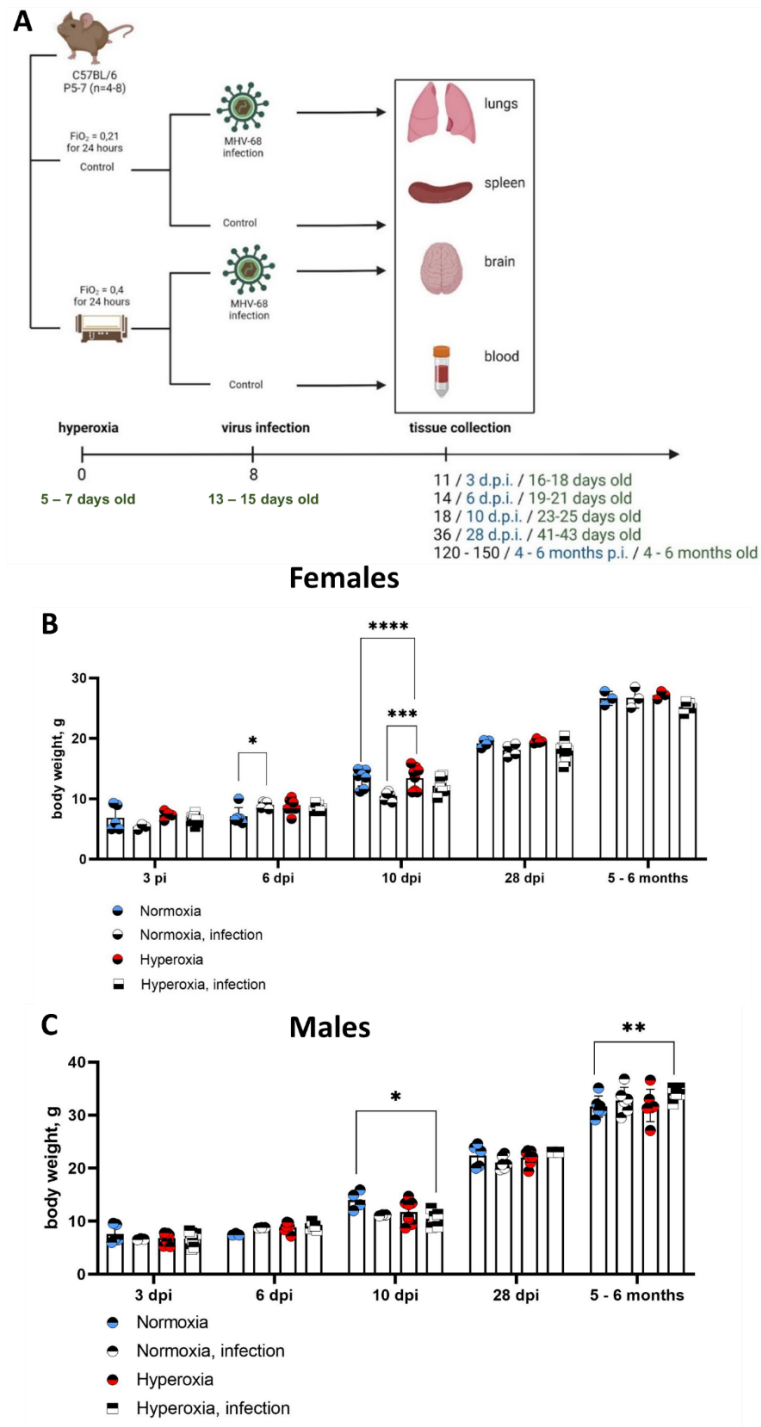


Figure 4.34. A mouse model of hyperoxia exposure and subsequent MHV-68 infection.

In vivo experimental design: 5-7 days-old mice pups were treated with O₂ (FiO₂ = 0.4) or room air (normoxia). Eight days after the first hit, the second hit was induced by infecting mice intranasally with MHV-68. Lungs, brains, spleens, and blood were harvested for analysis 3, 6, 10, 28 days, or 4 – 6 months after the second hit (A) (Picture was created with BioRender.com). Weight measurements were taken on the day of sacrifice, from n = 3 – 8 females (B) and n = 3 – 8 males (C) over time. One-way ANOVA test with multiple comparisons correction. *p-value < 0.05, **p-value < 0.01, ***p-value < 0.001, ****p-value < 0.0001.

4.2.2. Hyperoxia increased the lytic MHV-68 titer in the lungs but did not change the viral genomic load in the spleen.

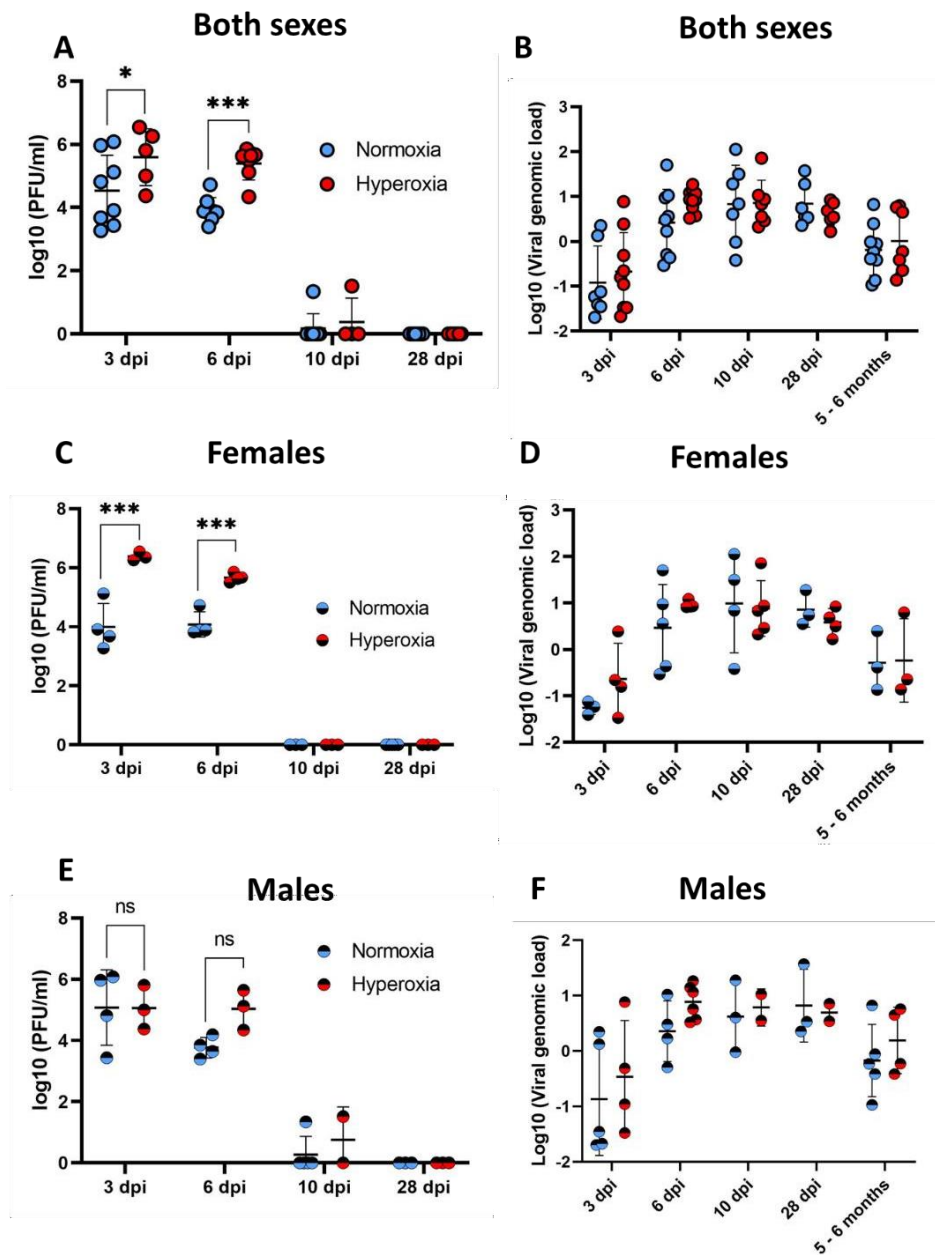


Figure 4.35. MHV-68 titer in the “right lung lobe” lysates (A, C, E) and viral genomic load in the spleen (B, D, F).

Virus titer measurements were made via the Plaque assay in the right lung lobe of the mice (A – both sexes, C – females (n=3-4), E – males (n=2-4)). For the viral genomic load, DNA was extracted from spleen pieces (B – both sexes, D – females (n=3-4), F – males (n=3-5)). Viral DNA was quantified by qPCR. One-way ANOVA test with multiple comparisons correction. *p-value < 0.05, **p-value < 0.01, ***p-value < 0.001, ****p-value < 0.0001.

The life cycle of MHV-68 involves distinct lytic and latent phases. Upon intranasal infection, the virus undergoes lytic replication in lung epithelial cells and

subsequently spreads the latent virus to lymphoid tissues, including the bone marrow, lymph nodes, and spleen. To investigate the impact of pre-exposure to hyperoxia on viral loads in the lung and spleen after mice were exposed to 40% oxygen and then infected with MHV-68, I initiated the following studies: lytic replication of MHV-68 in the lung was assessed using a plaque assay, while the viral genomic load in the spleen was examined through qPCR (**Figure 4.35.**).

In the context of the acute lytic phase of infection, a significant increase in virus titer was noted in the lungs of infected mice after exposure to hyperoxia (**Figure 4.35. A**). Female samples demonstrated significantly higher virus titers in the lungs after hyperoxia exposure on day 6 post-infection compared to males (**Figure 4.35. C and E**). The acute phase of MHV-68 infection varies between males and females, with additional oxygen treatment exerting an influence. Notably, both sexes exhibited similar establishment of MHV-68 latency, hyperoxia exposure did not affect this process (**Figure 4.35. B, D, and F**).

4.2.3. Histological changes in the lung

Mouse lung development after birth is a continuous process with no distinct endpoint. However, after approximately 35-36 days of age, the rate of lung development significantly slows down. As a result, once microvascular maturation concludes, the expansion of the gas-exchange region will occur through lung development rather than a substantial increase in new alveoli. Therefore, I expected to observe growth in alveolar numbers and alveoli size until a certain age point, and then the rise should be much slower (Sonja I. Mund, Marco Stampanoni, Johannes C. Schittny, 2008).

I conducted an assessment of lung morphology, as illustrated in **Figures 4.36.** and **4.37**. Lungs of mice exposed to hyperoxia and infected with MHV-68 were stained with H&E to see a comprehensive picture of the microanatomy of the lungs (**Figure 4.36.**). On day 10 post-infection, mice treated with $\text{FiO}_2 = 0.4$ displayed airway simplification and air space enlargement in comparison to mice raised under normoxic conditions ($\text{FiO}_2 = 0.21$). The latter group exhibited no peribronchial inflammation, and their pulmonary parenchymal architecture remained unaltered, as depicted in **Figure 4.36**. Images captured on day 28 and at the 5-6 month post-infection time points revealed a persistent hyperoxia-induced impact on lung development.

Conversely, the lung histology of mice infected with MHV-68 with or without previous hyperoxia exposure displayed severe injury regions, peribronchial and interstitial thickening of the alveolar walls on days 10 and 28 post-infection and moderate inflammation on 5-6 months post-infection (**Figure 4.36.**).

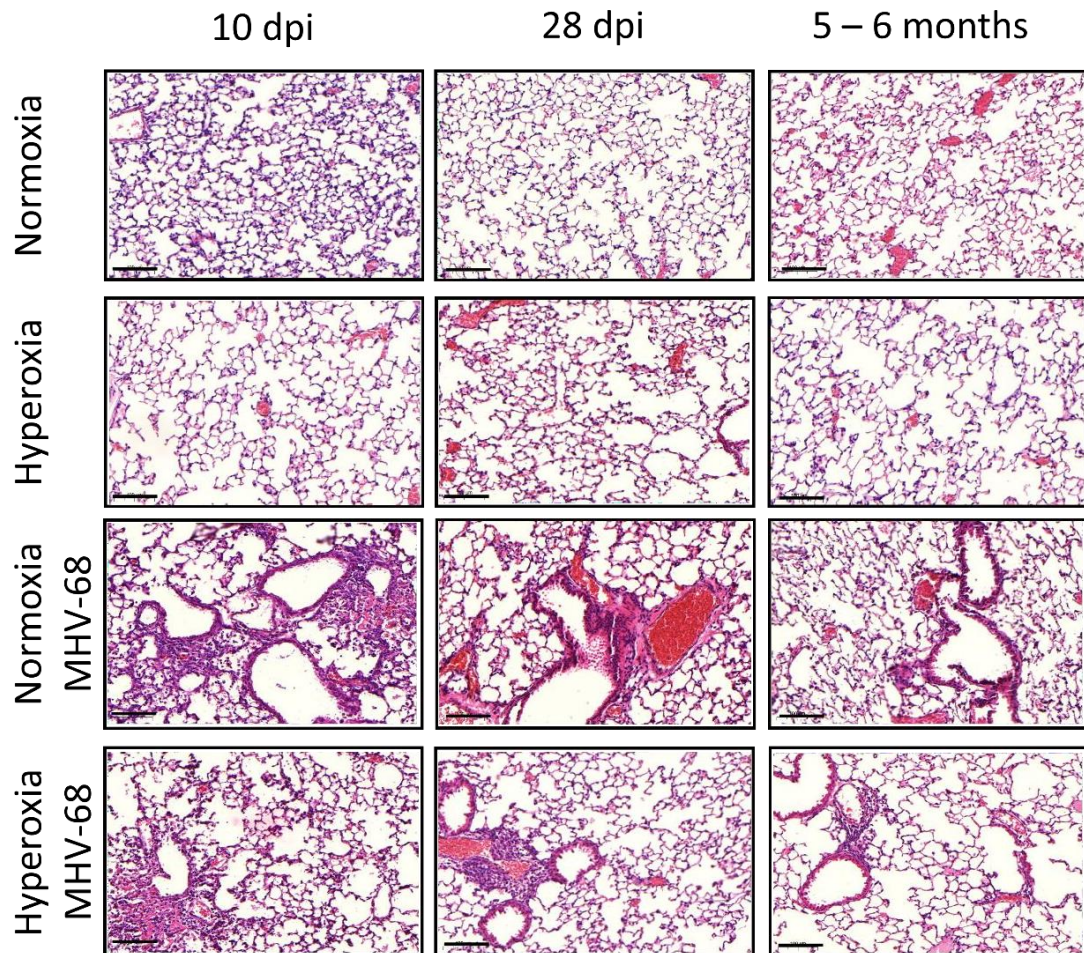


Figure 4.36. H&E staining of lung sections.

Normoxia control mice, hyperoxia-exposed mice, MHV-68-infected mice, and both Hyperoxia-exposed and MHV-68-infected mice on days 10, 28, and 5 – 6 months after infection. Scale bars: 100 μ m.

To assess the influence of hyperoxia exposure on the severity of MHV-68-induced inflammation, lungs stained with H&E were examined. For the assessment of lung damage on the slides, visual scoring method was used, where:

0 - normal - no lesions at all, clear alveoli and walls

1 - minimal - purple area, less than 25% of the total area OR one or several (up to 10) small dark purple areas

2 - moderate - purple area, less than 50% of the total area OR a lot of small dark purple areas (more than 10) OR one or two big dark purple areas

3 - severe - purple area, more than 50% of the total area OR a lot of big dark purple areas

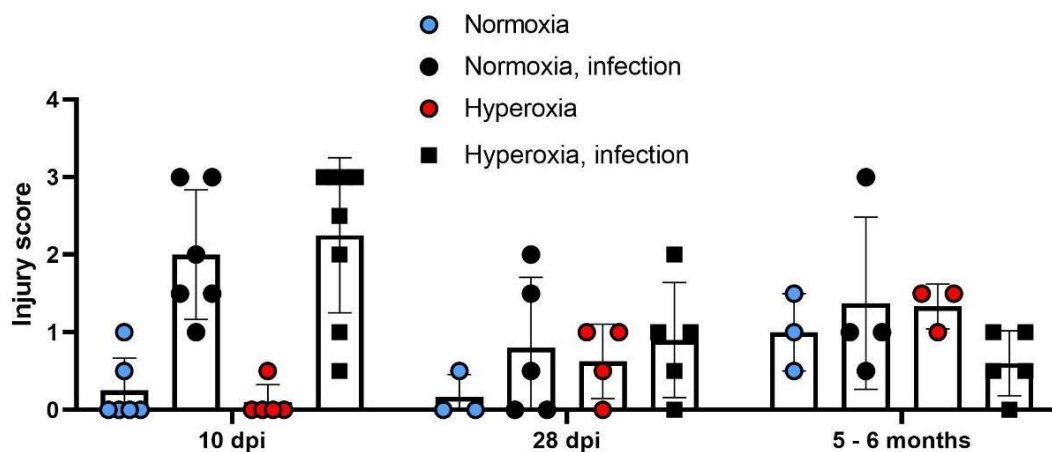


Figure 4.37. Assessment of inflammation in H&E-stained lung tissue sections.

A total lung inflammation score was determined for 3 - 6 mice in each group and graded on a scale of 0 (normal) to 3 (severe). A single section from all lung lobes was viewed and scored as a consensus by two scientists blinded to the groups.

Initial exposure to hyperoxia influenced viral infection and may be responsible for the altered consequences of the MHV-68 lytic phase in adult lungs.

4.2.4. MHV-68 infection and hyperoxia exposure in the first month of life significantly changed lung morphology in adults

Next, I investigated the potential impact of MHV-68 infection with or without prior hyperoxia exposure on lung development. To accomplish this, I analyzed the size and quantity of alveoli in mouse lungs. One of the most commonly evaluated lung morphology indicators is the average size of the alveoli (Shawn E. Soutiere and Wayne Mitzner, 2005), which I calculated by determining the ratio between the overall alveolar area and the number of alveoli (**Figure 4.38.**)

In the normoxia conditions ($FiO_2 = 0.21$), no significant differences in lung architecture were observed at 28 days and 5 - 6 months post-infection after the

MHV-68 infection. A comparison between the infected and uninfected samples revealed increased alveolar sizes on day 10 post-infection.

Interestingly, mice exposed to hyperoxia ($\text{FiO}_2 = 0.4$) in the early life demonstrated no changes in the alveolar size. Simultaneous viral infection, however, resulted in a significant reduction in alveolar size compared with hyperoxia exposure alone on day 10 post-infection. In addition, the combination of MHV-68 infection and hyperoxia exposure in the early stages of development significantly increased the average alveolar size in adults (5 – 6 months post-infection) in comparison with the day 10 post-infection.

Male and female mice did not demonstrate any significant difference in the average alveoli size.

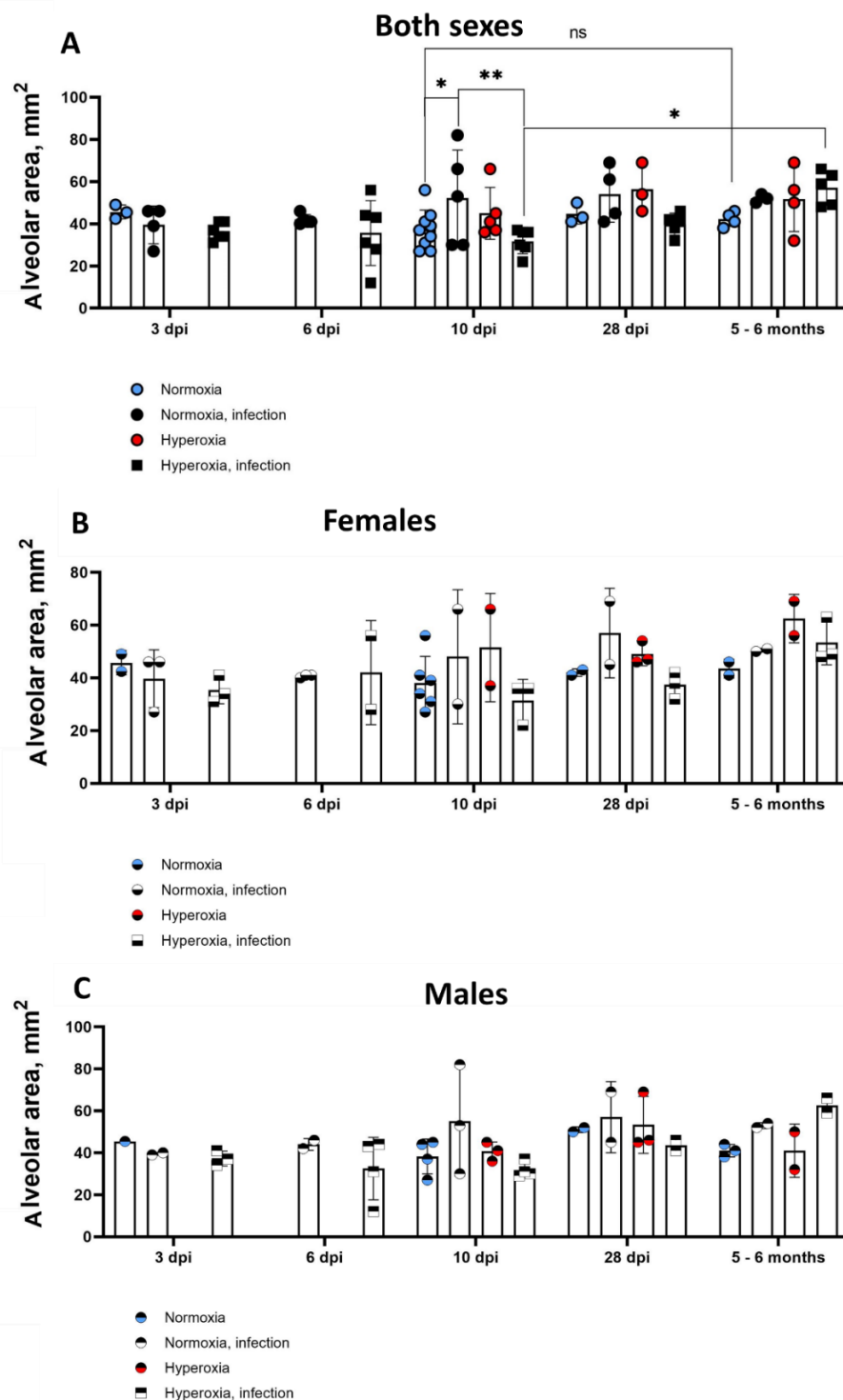


Figure 4.38. Alveolar size measured in adult mice after hyperoxia exposure and MHV-68 infection in childhood.

A – both sexes, B – female mice (n=2-6), C – male mice (n=1-4). H&E-stained lung histology slice images were converted into Bioquant software images. Three to four nonoverlapping 100 μ m fields were sampled from each section, intentionally avoiding the large airways and blood vessels. All the alveoli were counted and measured with the help of software. Hyperoxia exposure samples, 3 dpi, 6 dpi, and normoxia control 6 dpi were not performed. Two-way ANOVA test with multiple comparisons corrections. *p-value < 0.05, **p-value < 0.01.

Simplification of the alveolar structure and changes in alveolar size can result in a different average number of alveoli. Radial Alveolar Count (RAC) (**Figure 4.39.**) was calculated as the number of alveoli intersected by a line drawn from the center of a respiratory bronchiole to the closest definitive connective tissue septum (Owais R. Tisekar and Ajith Kumar AK, 2022). RAC is directly proportional to the number of intact tissue septa and is expected to diminish as alveolar walls undergo degradation. The study by Jaramillo-Rangel et al. in 2023 observed a decline in RAC numbers in aged mice until it reached a plateau.

Sole viral infection did not exert an impact on alveolar growth comparable to the influence observed with exposure to hyperoxia (**Figure 4.39.**). However, the combination of viral infection and oxygen supply led to a significant increase in RAC in adult mice of both sexes (days 10, 28, and 5 – 6 months post-infection).

Interestingly, in the acute phase of virus infection (day 3 post-infection), RAC in female lungs was significantly higher than RAC in the double-hit samples. Conversely, in male lungs, the effect was the opposite; RAC was significantly higher after the combination of hyperoxia exposure and virus infection compared with infected samples alone. By day 10 post-infection, female samples again exhibited a significant increase in RAC in the double-hit condition, whereas male lungs showed consistent RAC in the uninfected and infected mice with or without prior hyperoxia exposure.

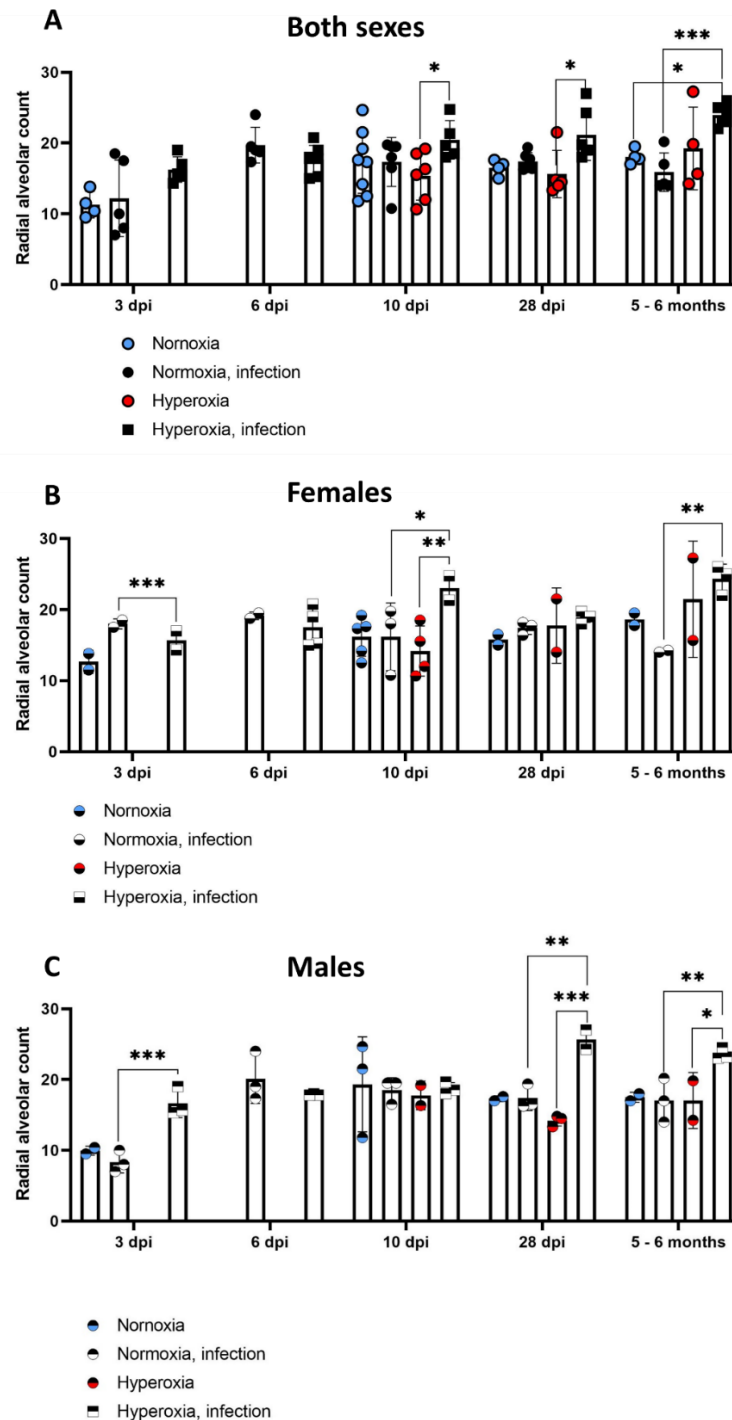


Figure 4.39. RAC measurements in adult mice after hyperoxia exposure and MHV-68 infection in childhood.

A – both sexes, B – female mice (n=2-6), C – male mice (n=1-3). H&E-stained lung histology slice images were converted into Bioquant software images. Only terminal bronchioles visible within a 10x view from a pleural surface or a connective tissue septum were included to obtain an accurate count. The counting was performed on 3-4 mice per condition, and each slide was examined to make 15-20 counts, ensuring a reliable distribution. Hyperoxia exposure samples, 3 dpi, 6 dpi, and normoxia control 6 dpi were not performed. Two-way ANOVA test with multiple comparisons corrections. *p-value < 0.05, **p-value < 0.01, ***p-value < 0.001.

According to Wickramasinghe et al. (2021), the thickening of the septal wall is often seen as an indication of a "new" BPD in the literature. In the human patients with COVID-19, significant septal thickening was revealed (Wu, J. et al, 2020). Therefore, to explore the potential association between changes in the septal wall and an increase in the number and size of alveoli, tissue and airspace areas were measured (**Figure 4.40.**).

The measurement of septal wall thickness involves calculating the ratio between tissue area and airspace area, where a higher ratio signifies an increased thickness. MHV-68 infection did not alter wall thickness, as well as hyperoxia exposure ($FiO_2 = 0.4$) did not result in statistically significant alterations in the parameter (**Figure 4.40. A**). However, when combined, viral infection and hyperoxia exposure significantly decreased wall thickness in adults (5 – 6 months post-infection). At the beginning of the infection, both sexes looked the same. Interestingly, on day 28 post-infection, a difference between male and female samples was also clearly visible: male samples demonstrated no changes, and wall thickness in females was significantly higher in the double-hit exposure model (**Figure 4.40. B and C**).

MHV-68 infection and hyperoxia exposure together changed lung architecture, resulting in thinner septal walls and increased alveoli number and area in adulthood.

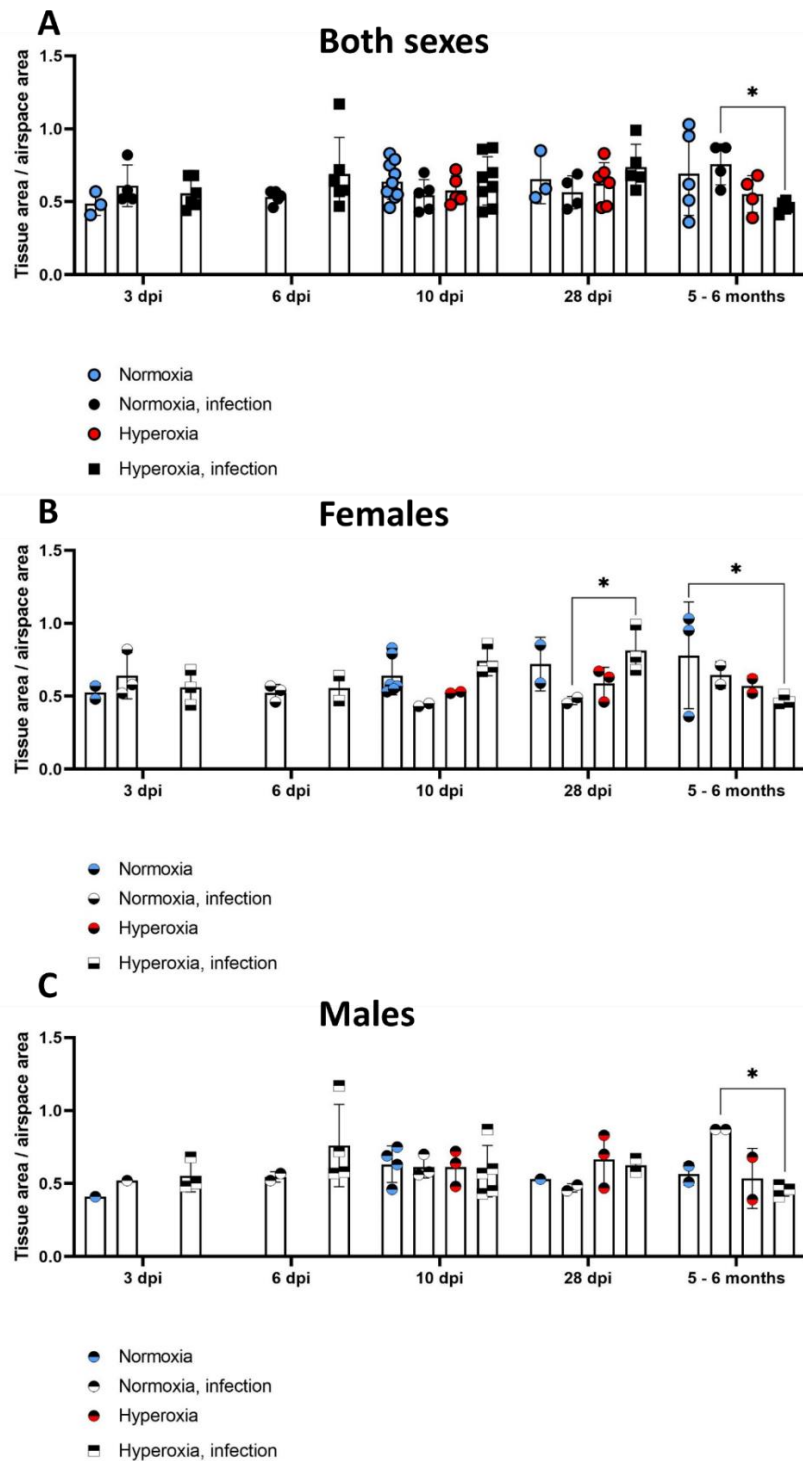


Figure 4.40. Septal wall thickness measured in adult mice after hyperoxia exposure and MHV-68 infection in childhood.

A – both sexes, B – female mice (n=2-6), C – male mice (n=1-3). H&E-stained lung histology slice images were converted into Bioquant software images. Three to four nonoverlapping 100 μ m fields were sampled from each section, intentionally avoiding the large airways and blood vessels. Using the software, tissue areas, and airspace areas were measured. Hyperoxia exposure samples, 3 dpi, 6 dpi, and normoxia control 6 dpi were not performed. Two-way ANOVA test with multiple comparisons corrections. *p-value < 0.05.

4.2.5. Vascular development in the lungs after double-hit injury

The pulmonary capillary network undergoes significant expansion after birth, growing 35-fold by the time an individual reaches adulthood. The development of airways and blood vessels in the lung is interdependent, with changes in one process affecting the other, resulting in widespread disruption of lung development. In addition, pulmonary vascular development continues proportionally to overall lung growth throughout all stages of development, making it susceptible to perturbations during both embryonic and postnatal life (Cristina M. Alvira, 2016).

Infants diagnosed with BPD exhibited decreased pulmonary microvascular density, as evidenced by an overall reduction in immunostaining for the endothelial-specific marker CD31 in their lungs (Bhatt, A. J. et al., 2011).

Mice infected with MHV-68 exhibited no discernible influence of the virus on pulmonary vascularization. Likewise, a 24-hour exposure to hyperoxia did not significantly alter vessel numbers in the lungs of exposed mice (**Figure 4.41. A**). Concurrent infection and exposure did not induce changes in pulmonary vessel formation. Female and male samples did not show any difference related to the vessel number in the lungs after MHV-68 infection with or without prior hyperoxia exposure.

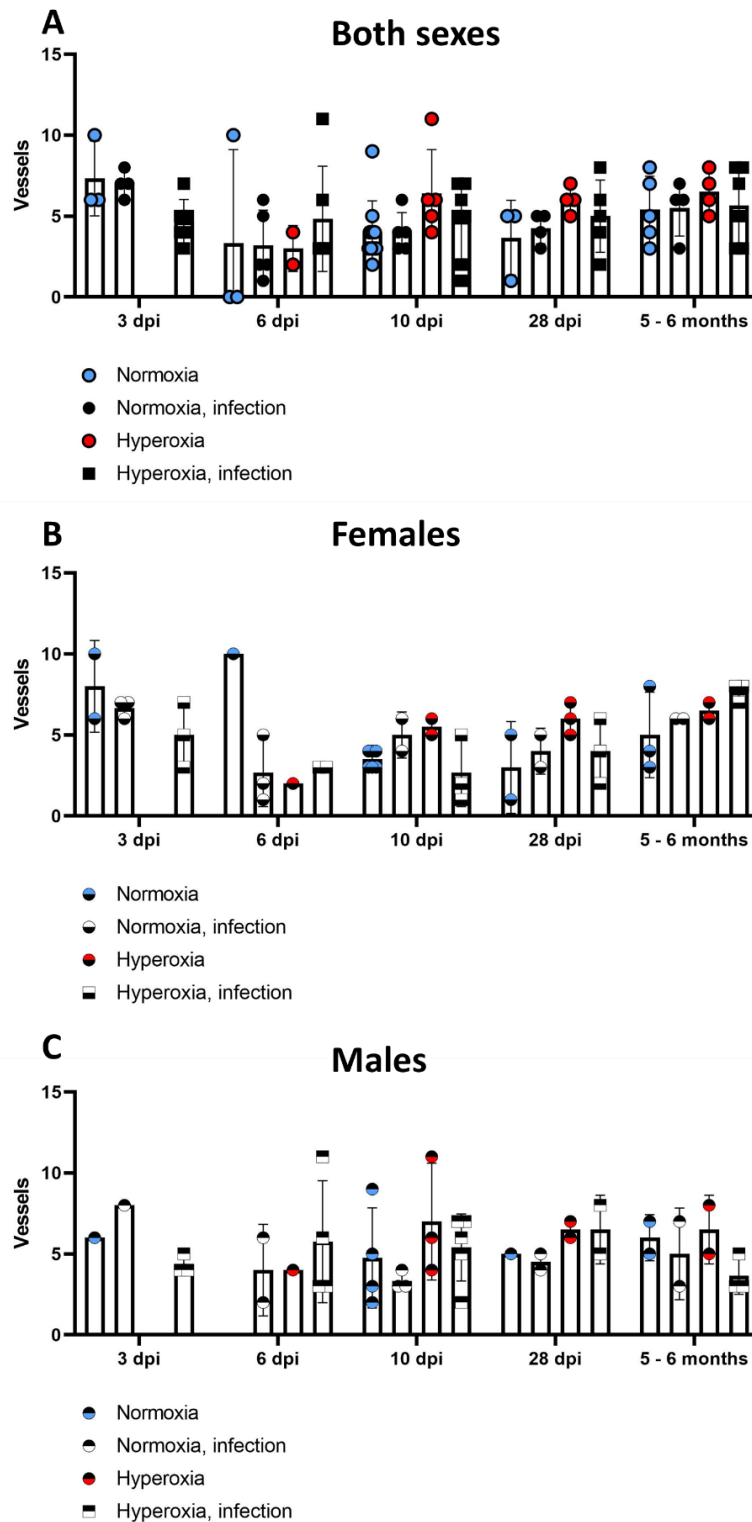


Figure 4.41. Vascularization development in adult mice after MHV-68 infection and hyperoxia exposure in childhood.

A – both sexes, B – female mice (n=2-6), C – male mice (n=1-3). H&E-stained lung histology slice images were converted into Bioquant software images. Three to four nonoverlapping 100 μ m fields were sampled from each section. Vessels were measured with the help of software. Hyperoxia exposure samples on 3 dpi were not performed. Two-way ANOVA test with multiple comparisons corrections.

4.2.6. *The impact of Hyperoxia treatment on the regulation of developmentally relevant genes following secondary MHV-68 infection*

In section 4.1.7, I showed that PDGF-R α protein and *Pdgfra* gene expression was significantly attenuated in mouse primary fibroblasts treated with FiO₂ = 0.4 for 24 hours and infected with MHV-68. However, hyperoxia exposure alone did not affect PDGF-R α protein or *Pdgfra* gene expression.

Therefore I aimed to investigate the transcriptional regulation of the *Pdgfra* gene *in vivo* at specific time points post-infection, namely days 10, 28, and 5-6 months, as these time points correspond to the period of most remarkable morphological changes. I found no significant differences in the mRNA expression of *Pdgfra* between uninfected control group and groups infected with the MHV-68 with or without prior hyperoxia exposure (**Figure 4.42.**). When considering both sexes together, no changes in gene expression were observed.

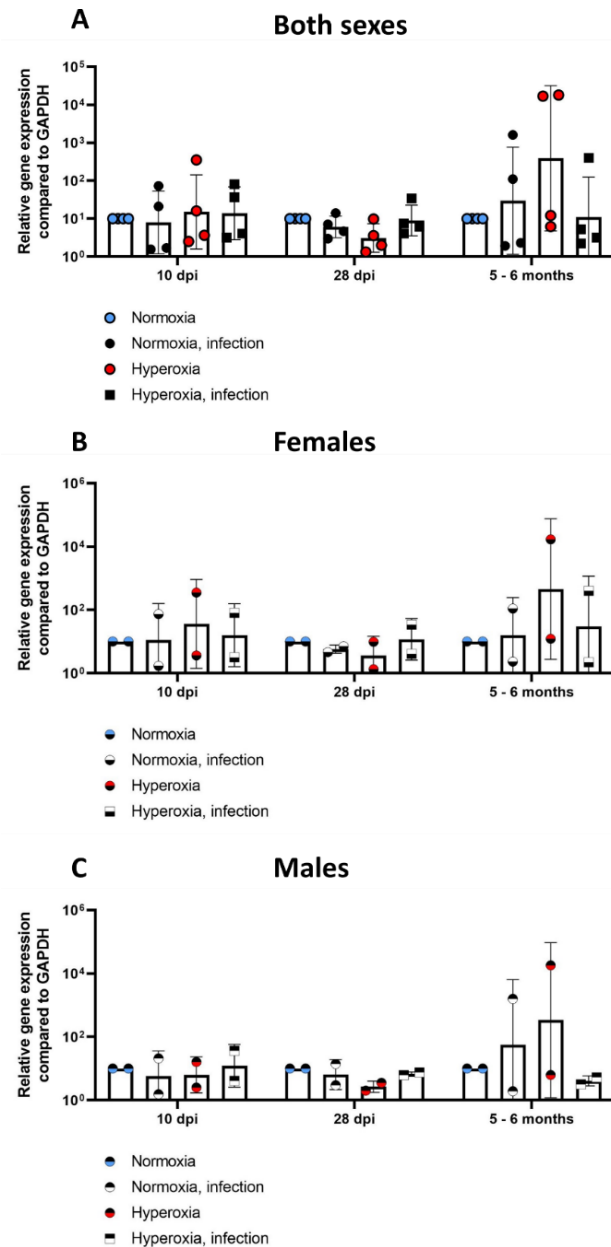


Figure 4.42. *Pdgfra* gene expression in adult mice in the double-hit model.

A – both sexes, B – female mice (n=2), C – male mice (n=2). qPCR was used to quantitate the mRNA expression of *Pdgfra* in whole lung lysates from $\text{FiO}_2 = 0.4$ – treated and virus-infected mice and controls harvested 10 days, 28 days, and 5 – 6 months after treatment. *Gapdh* was used as a reference gene. Data are represented as median with interquartile range. Two-way ANOVA test with multiple comparisons corrections.

Section 4.1.5 presented findings from *in vitro* experiments that showed decreased PCNA protein and gene expression following hyperoxia exposure or MHV-68 infection, alone or in combination. The results from the *in vivo* experiment (**Figure 4.43.**) were intriguing: on days 10 and 28 post-infection, *Pcna* gene expression was not changed by MHV-68 infection, hyperoxia exposure, or

double-hit model. However, at 5 – 6 months post-infection, the mRNA expression of *Pcna* was significantly downregulated by MHV-68 with prior hyperoxia exposure comparing with day 10 post-infection (**Figure 4.43. A**). Females demonstrated a significant impact of both hyperoxia exposure and MHV-68 infection on gene expression (**Figure 4.43. B**).

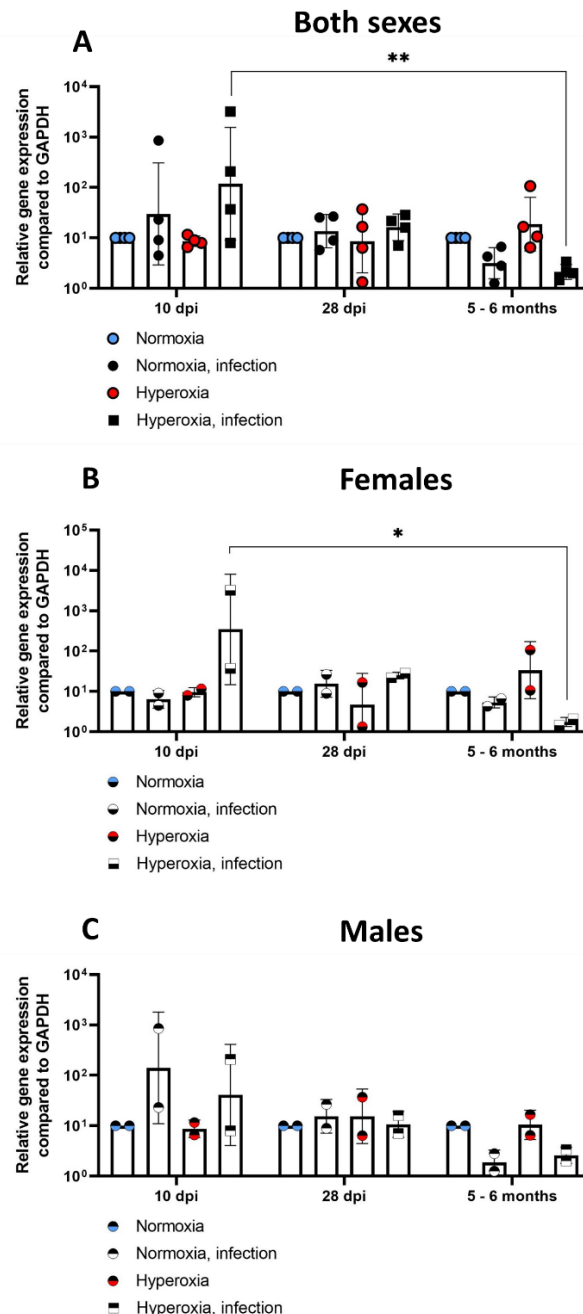


Figure 4.43. *Pcna* gene expression in adult mice in the double-hit model.

A – both sexes, B – female mice (n=2), C – male mice (n=2). qPCR was used to quantitate the mRNA expression of *Pcna* in whole lung lysates from FiO₂ = 0.4 – treated and virus-infected mice and controls harvested 10 days, 28 days, and 5 – 6 months after treatment. *Gapdh* was used as a reference gene. Data are represented as median with interquartile range. Two-way ANOVA test with multiple comparisons corrections. *p-value < 0.05, **p-value < 0.01.

In section 4.1.6, *Acta2* gene expression was investigated in relation to the effect of hyperoxia exposure and MHV-68 infection in CCL-206 cells and mouse primary fibroblasts. The results revealed no significant changes in the expression of the *Acta2* gene in these cells. However, to further explore the potential impact of the virus infection on the fibroblast population during hyperoxia injury, an investigation of the mRNA expression in whole lung lysates was conducted (Figure 4.44.). The analysis of the results showed that MHV-68 infection with prior hyperoxia exposure led to decreased gene expression within 5-6 months of infection. Hyperoxia exposure alone resulted in no changes in *Acta2* gene expression. Notably, the virus infection together with hyperoxia exposure appeared to trigger long-lasting mechanisms. Males demonstrated a significant impact of both hyperoxia exposure and MHV-68 infection on gene expression in adult mice.

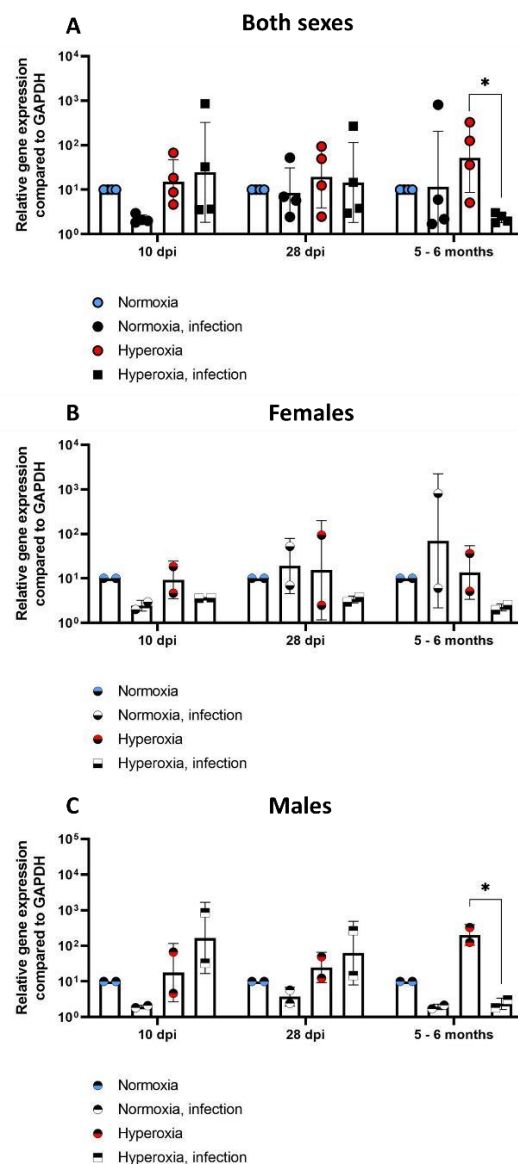


Figure 4.44. *Acta2* gene expression in adult mice in the double-hit model.

A – both sexes, B – female mice (n=2), C – male mice (n=2). qPCR was used to quantitate the mRNA expression of *Acta2* in whole lung lysates from $FiO_2 = 0.4$ – treated and virus-infected mice and controls harvested 10 days, 28 days, and 5 – 6 months after treatment. *Gapdh* was used as a reference gene. Data are represented as median with interquartile range. Two-way ANOVA test with multiple comparisons corrections. *p-value < 0.05, **p-value < 0.01.

In recent studies, it has been revealed that individuals subjected to severe hyperoxia treatment ($FiO_2 > 0.7$) exhibit activation of the canonical WNT/ β -catenin signaling pathway, accompanied by a decrease in fibroblasts expressing *Pdgf-R α* (Riccetti et al., 2022; Sucre et al., 2020). During the saccular phase of lung development, the dysregulation of *Wnt5a*, a non-canonical WNT ligand, impedes the differentiation of alveolar epithelial type I cells, myofibroblasts, and endothelial cells, thereby obstructing the development of distal airways (C. Li et al., 2020). Additionally, *Hif1a*, a crucial gene acting as an oxygen sensor, plays a significant role in normal lung development (Kirschner et al., 2022).

To investigate the impact of cell cycle regulation on key developmental pathways and cellular functions in mice exposed to hyperoxia and MHV-68 infection and controls, I assessed the mRNA expression levels of *Wnt5a* and *Hif1a* genes in whole lung lysates subjected to both normoxia and hyperoxia conditions ($FiO_2 = 0.4$) and infected with MHV-68.

Mice, regardless of whether they were previously infected with MHV-68 or exposed to hyperoxia for 24 hours or not, including control uninfected mice, did not display any noticeable difference in *HiF1a* gene expression on days 10 and 28, as well as 5 to 6 months post-infection (**Figure 4.45.**). Additionally, both females and males exhibited similar gene expression levels. In contrast, the expression of the *Wnt5a* gene was found to be notably increased after hyperoxia exposure at day 28 post-infection compared with that in the uninfected samples (**Figure 4.46.**). Subsequently, at 5-6 months post-infection, *Wnt5a* expression significantly decreased in mice following MHV-68 infection after hyperoxia exposure, with lower gene expression observed in the samples exposed to the double-hit (virus infection and hyperoxia). No differences were revealed between females and males in the *Wnt5a* gene expression.

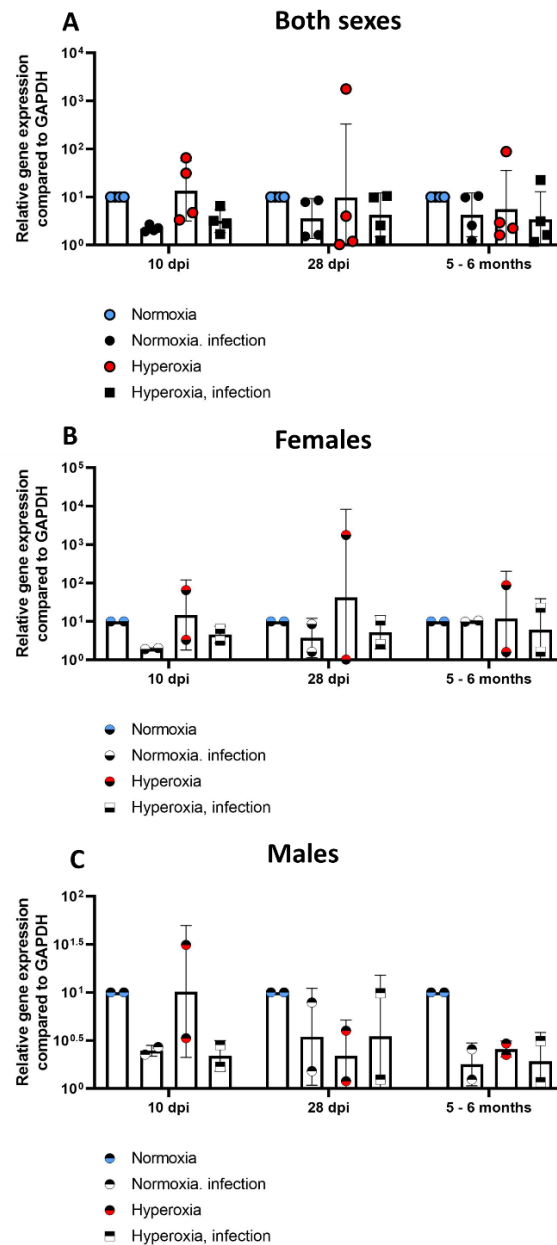


Figure 4.45. *Hif1a* gene expression in adult mice in the double-hit model.

A – both sexes, B – female mice (n=2), C – male mice (n=2). qPCR was used to quantitate the mRNA expression of *Hif1a* in whole lung lysates from $FiO_2 = 0.4$ – treated and virus-infected mice and controls harvested 10 days, 28 days, and 5 – 6 months after treatment. *Gapdh* was used as a reference gene. Data are represented as median with interquartile range. Two-way ANOVA test with multiple comparisons corrections.

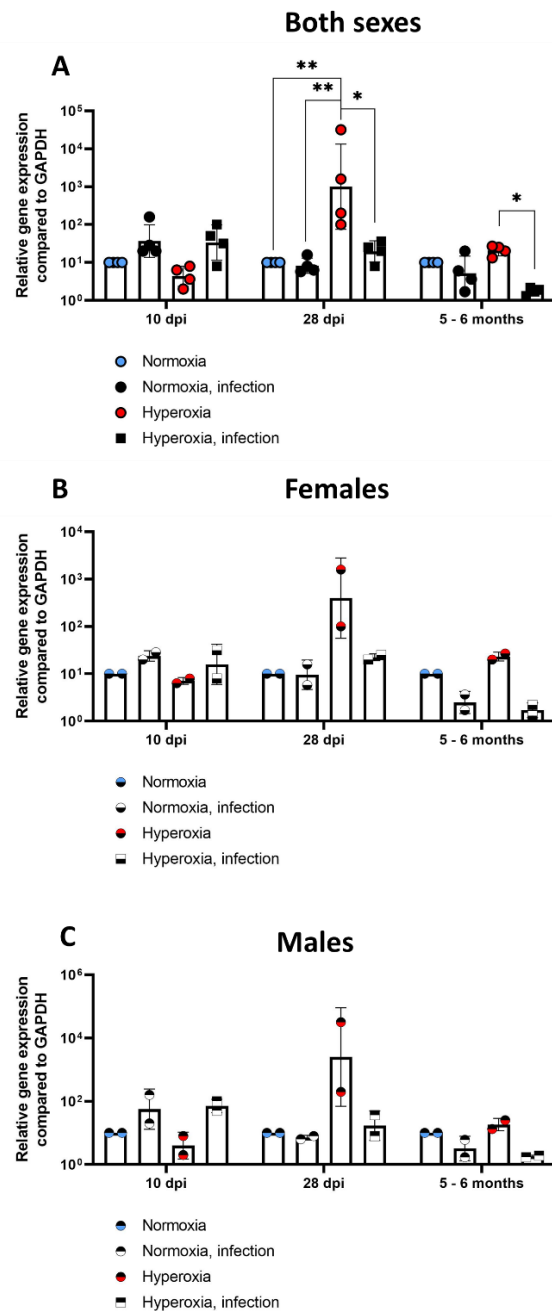


Figure 4.46. *Wnt5a* gene expression in adult mice in the double-hit model.

A – both sexes, B – female mice (n=2), C – male mice (n=2). qPCR was used to quantitate the mRNA expression of *Wnt5a* in whole lung lysates from $FiO_2 = 0.4$ – treated and virus-infected mice and controls harvested 10 days, 28 days, and 5 – 6 months after treatment. *Gapdh* was used as a reference gene. Data are represented as median with interquartile range. Two-way ANOVA test with multiple comparisons corrections. *p-value < 0.05, **p-value < 0.01.

5. Discussion

Viral infections have been implicated in causing persistent epithelial and fibrotic injuries in the lungs, playing a significant role in the pathogenesis of fibrosis (Mora, A. L. et al, 2005). In the past few years, there has been an increasing focus on the connection between viral infections and pulmonary fibrosis, particularly following the emergence of SARS-CoV-2 in 2019. Nevertheless, there remains a lack of comprehensive understanding regarding the mechanisms responsible for virus-induced pulmonary disturbances (Huang, W. J. and Tang, X. X., 2021).

To minimize the need for *in vivo* experiments, I initially established an *in vitro* viral infection model to evaluate potential *in vivo* implications. Neonatal mice lung primary fibroblasts, a major pulmonary cell type, were chosen for *in vitro* experiments. Also, I employed the CCL-206 cell line to reduce the number of sacrificed mice during the establishment of the experimental model. CCL-206 is a commercially available cell line with fibroblast morphology, originally isolated in 1964 from the lung of a normal male mouse.

Existing literature suggests that 18 to 24 hours of virus infection induces irreversible changes in lung fibroblasts (Boyd, D. F. et al, 2020; Wendisch, D. et al, 2021). Employing a 24-hour MHV-68 infection, our study demonstrated changes in living mouse primary fibroblasts, with 48 and 72 hours. This extended timeframe allowed us to observe pronounced effects on living mouse primary fibroblasts, particularly in terms of Annexin V binding and necrosis processes. Wound healing and migration assays showed a reduced ability of infected CCL-206 cells and primary fibroblasts to proliferate and migrate compared to uninfected cells. The morphological changes observed, including cell shrinkage and detachment from the flask, further highlight the dynamic alterations occurring during prolonged infection periods. These changes, coupled with the observed decrease in *Pdgfra* and increase in *Vegf* gene expression, provide valuable indicators of the virus-induced modulation of key molecular pathways in infected mouse lung primary fibroblasts. Elevated *Vegf* expression is linked to pulmonary vascular permeability and pulmonary fibrosis (Amano, H. et al, 2019), while PDGFR inhibition can attenuate typical features of lung fibrosis (Abdollahi, A. et al, 2005). Downregulated *Pdgfra* expression in infected fibroblasts contradicted fibrosis-like injuries, and unaltered α SMA gene expression supported the non-

fibrotic nature of the viral infection. Our results imply that MHV-68 infection may lead to cell-cycle arrest, resulting in reductions in proliferation, apoptosis, migration, and *Pdgfra* gene expression. It is noteworthy that lytic infection by herpesviruses is known to induce cell cycle arrest at the G1/S transition, as evidenced by previous studies. Specifically, proteins from capsids of herpes simplex virus type 1, human cytomegalovirus, and Epstein-Barr virus (EBV) have been identified to induce the accumulation of G1/S cells (Paladino, P. et al, 2014). In another research, selected EBV proteins were examined for their effects on the cell cycle, verifying their impact on p53 and p21, which serve as regulators of the G1/S transition. Similarly, research involving human herpesvirus 6 (HHV-6) infection in human embryonic fibroblasts demonstrated decreased proliferation and increased apoptosis, with a specific observation of cell cycle arrest at the G2/M phase (Li, L. et al, 2012). To further elucidate the exact phase of the cell cycle arrest induced by MHV-68 infection in lung cells, future studies can focus on investigating cell-cycle regulator proteins such as p53 and p21 for the G1/S phase, p27 for the G2/M phase, or overall cyclins and cyclin-dependent kinases (Cdks) responsible for guiding the cell through various checkpoints. Moreover, our findings support the idea that CCL-206 cells exhibit similar behavior to mouse primary lung fibroblasts, establishing their potential utility in refining *in vitro* experimental protocols for viral infection studies. This consistency between cell lines provides a practical opportunity for further exploration and optimization of experimental procedures in a controlled *in vitro* setting.

In *in vivo* viral infection studies, mice older than 4 weeks are commonly utilized (Ceneviva, Z. J. et al, 2023; Altamirano-Lagos, M. J. et al, 2019; Du, J. et al, 2021; Bastidas-Legarda, L. Y. et al, 2017). However, limited research has focused on mice in the developmental stage of lung development and the impact of viral infection on lung development. Previous studies using a neonatal mouse model investigated the susceptibility to infection with Coxsackievirus B1 at 1, 3, 5, 7, 14, and 21 days postnatal (DOL), revealing increased vulnerability in younger mice and survival in 21-day-old mice. The age of initial infection is recognized as a crucial risk factor, with both increased susceptibility to virus infection and disease severity linked to an immature immune system. In this investigation, mice were infected at the age of 13–15 DOL. Tissue specimens were subsequently collected on days 3, 6, 10, and 28 post-infection, as well as

5–6 months. This comprehensive temporal sampling aimed to assess perturbations in lung morphology and find out potential alterations in molecular pathways in the pulmonary tissue. A visual assessment scoring system was implemented to quantify the impact of virus infection on pulmonary morphology. The analysis revealed a noteworthy distinction between infected and control lungs at days 10, 28, and 5–6 months post MHV-68 infection. Histological examination using H&E staining showcased dense areas in the lungs and enlarged alveoli with evident damage, with the highest incidence observed in lungs infected for 10 days. The expression levels of *Acta2*, *Pdgfra*, *Wnt5a*, and *Pcna* genes in the infected samples remained unchanged. The observed mismatch between significant morphological changes in lung histology following MHV-68 infection and the absence of alterations in *Acta2*, *Pdgfra*, *Pcna*, and *Wnt5a* gene expressions prompts an exploration into the underlying mechanisms governing the viral impact on lung tissue. The apparent contradiction may be attributed, in part, to the dynamic nature of gene expressions during distinct stages of the viral infection cycle. Although the harvesting days were strategically chosen to encompass both the lytic and latent phases of MHV-68's impact on the lungs, the histological analysis did not include examination of gene expressions on days 3 and 6 post-infection. Notably, another research has demonstrated that alveolar epithelial cells exhibit downregulation of the *Wnt5a* gene on day 3 post-Influenza A infection, suggesting a potential early response to viral insult (Hancock, A. S. et al, 2018). Moreover, the observed gap in the repair processes between days 10 and 28 post-infection remains unexplored. In the context of Influenza infection, it has been documented that *Pcna* gene expression is upregulated on day 15 post-infection, corresponding to the later phase of recovery (Tan, K. S. et al, 2014). This temporal discrepancy underscores the need for a more comprehensive time-course analysis to elucidate the intricate temporal dynamics of molecular changes associated with MHV-68 infection. In conclusion, while the histological changes suggest a significant impact on lung tissue, the absence of concurrent alterations in selected gene expressions underscores the complexity of viral-host interactions. A more detailed exploration, particularly considering the temporal nuances and phases of viral infection, will provide a clearer understanding of the mechanistic intricacies governing the observed phenomena.

The next part of my thesis was dedicated to the study of Bronchopulmonary dysplasia (BPD) and how MHV-68 infection can change its development. Among children diagnosed with bronchopulmonary dysplasia, respiratory viral infections resulted in substantial morbidity. This morbidity encompassed prolonged and frequent hospitalizations, particularly during the peak of the respiratory viral season (Resch, B. et al, 2016). Animal models are crucial in understanding the progression of diseases and in the early stages of drug development. An advantageous aspect of animal experimental models for BPD study is that neonatal rodents are delivered during the sacular stage of lung development, equivalent to the 24-32 week gestation period in humans. There is no requirement to artificially induce premature birth (Costa, R. H. et al, 2001). The effects of severe hyperoxia ($FiO_2 = 0.7$ to 1.0) exposure in the mouse lung have been widely employed in studies related to BPD concerning short and long-term consequences. Researchers face challenges in selecting a singular exposure regimen for mice and implementing it across various methodologies. In many investigations, neonatal mouse pups were exposed to high levels of oxygen – 75% (Wickramasinghe, L. C. et al, 2021), 85% (Shrestha, D. et al, 2021), or even 100% (Woeller, C. F. et al, 2021) for a duration ranging from 4 to 14 days. Then mice were sacrificed either immediately following hyperoxia exposure, in one week, or two months. These studies have reported different lung injuries, such as septal wall thickening, fibrosis, expanded alveoli, and pulmonary interstitial emphysema. While these studies have shown promise as BPD animal models, it is important to note that the used oxygen levels do not align with the clinically relevant hyperoxia exposure for preterm infants. Clinically relevant models allow researchers to better mimic the complex pathophysiology of BPD observed in human patients. This provides a more accurate representation of the disease's progression, allowing for a deeper understanding of the underlying mechanisms and contributing factors. Furthermore, given that BPD is considered a lifelong condition, there is a notable lack of studies concerning the effects of hyperoxia conditions in the long term which would be reflected when studying e.g. 6-month-old mice. Therefore, my study addressed also the establishment of a more clinically relevant BPD animal model *in vitro* and *in vivo* to study life-long consequences.

Current experimental models may not fully recapitulate the complexity of BPD observed in human patients. By creating more clinically relevant models, researchers can better mirror the pathological features of BPD seen in infants, enhancing the translatability of findings to human disease. Improved models can provide insights into the dynamic progression of BPD. This includes studying the evolution of fibrosis, inflammation, and lung development over time, helping researchers understand the temporal aspects of the disease, and identifying critical windows for potential interventions. Enhanced *in vitro* models may reduce the reliance on animal studies, providing a more ethical and cost-effective means of studying BPD. This aligns with the principles of the 3Rs (Replacement, Reduction, Refinement) in animal research.

BPD is primarily characterized by damaged alveoli and tissue destruction. Earlier investigations into mice exposed to $\text{FiO}_2 = 0.4$ for 24 hours revealed diminished PDGF signaling as a significant contributor to BPD, as documented by Oak et al. in 2017. Exposing mice to hyperoxia ($\text{FiO}_2 = 0.4$) for 24 hours reflected mild clinical conditions and induced BPD-like conditions without severe lung injuries in contrast to the outcomes of 100% exposure experiments (Buczynski, B. W. et al, 2012). To achieve this, my experimental plan aimed to strike a balance between replicating BPD conditions and ensuring a high survival rate among the mice after all the necessary manipulations, enabling the investigation of mice 5 to 6 months after the double-hit treatment, i. e. after both hyperoxia and virus infection.

Notably, exposure of lung fibroblasts to 40% oxygen for 24 hours in both CCL-206 cells and primary mouse lung fibroblasts did not exhibit notable morphological changes in the shape of fibroblasts. Analysis of Annexin V binding indicated no differences between exposed fibroblasts and control samples, while Caspase 3/7 activity and necrosis were significantly reduced. Exposure to elevated concentrations of oxygen leads to direct cellular oxidative damage due to heightened production of reactive oxygen species (Pagano, A. et al, 2006). Several factors could contribute to the observed phenomenon of decreased apoptosis and necrosis in lung fibroblasts after hyperoxia exposure, coupled with no discernible changes in cell morphology. For example, lung fibroblasts may activate adaptive mechanisms in response to hyperoxia, which could mitigate apoptosis and necrosis. Various studies employing morphological and

biochemical analyses have consistently demonstrated the multimodal nature of hyperoxia-induced pulmonary cell death, encompassing both necrosis and apoptosis. Numerous investigations across diverse animal models have established a correlative association between the severity of hyperoxic acute lung injury and heightened apoptosis, as corroborated by the works of Mantell and Lee (2000). So, the observed lack of changes in cell morphology may be time-dependent. Significant alterations in cell structure might occur at later time points after hyperoxia exposure, while the initial stages are marked by adaptive responses and minimal morphological changes. Future investigations can be made in the field of the molecular pathways of necrosis and apoptosis studies during the first 24 hours of virus infection with several time-points checking. However, current data revealed hyperoxia exposure ($FiO_2 = 0.4$) impact on the immortalized and primary lung fibroblasts.

CCL-206 cells demonstrated increased Caspase 3/7 activity after hyperoxia exposure, unlike primary fibroblasts. CCL-206 cells are likely immortalized cells derived from a specific tissue, and they may have altered genetic characteristics for apoptosis due to the immortalization process. This may impact their responses in contrast to primary fibroblasts, which are directly sourced from tissues and maintain more native characteristics. Immortalized cells, having been artificially modified to proliferate continuously, may lack certain attributes or functions typical of regular cells (Carter, M. et al, 2023). Notably, they lose cell cycle checkpoint pathways and avoid the senescence process (Soice, E. and Johnston, J., 2021). It is plausible that the interconnected processes of proliferation and apoptosis in immortalized lung fibroblasts have been underexplored, warranting future investigations in this direction. For instance, a more in-depth examination of apoptosis markers in hyperoxia-exposed primary cells and commercially available cell lines or a comparative analysis of multiple commercial cell lines to assess variations in apoptosis induction could be avenues for future research.

Hyperoxia exposure for 24 hours did not induce changes in fibroblast proliferation, migration, or the expression of *Acta2* and *Pdgfra* genes. Existing knowledge indicates the significance of PDGFR alpha-positive (PDGFRA+) fibroblasts in alveolarization, and studies have noted a reduction of PDGFRA+ fibroblasts in BPD (Ricetti, M. R. et al, 2022). Additionally, it has been observed

that moderate hyperoxia (40%) leads to a decrease in the proliferation of human lung fibroblasts (You, K. et al, 2019). I suggest that a FiO_2 of 0.4 is sufficient to induce alterations in fibroblasts, but it may not universally impact different cell lines across all molecular pathways. Also, these results may suggest that the initial 24-hour hyperoxia exposure for fibroblasts may have prompted an adaptive or compensatory response to increased oxygen levels. Potential mechanisms underlying this response could involve increased repair processes or the activation of alternative survival pathways. Future investigations should deepen into specific cellular markers associated with apoptosis and necrosis to further elucidate these processes.

As previously discussed, the transforming growth factor β (TGF β) pathway plays a main role in lung development, organ injury, and fibrosis (Calthorpe, R. J. et al, 2021). TGF β is implicated in the development of BPD, with most studies reporting elevated protein levels in samples associated with BPD (Lecarpentier, Y. et al, 2019; Calthorpe, R. J. et al, 2023). Furthermore, treatment of primary human epithelial cells with TGF β has been shown to enhance respiratory syncytial virus infection (Gibbs, J. D. et al, 2009). In our *in vitro* study, I employed TGF β stimulation on CCL-206 cells and primary mouse lung fibroblasts to investigate its potential to influence MHV-68 replication and infection outcomes. I compared the effects of TGF β treatment with hyperoxia exposure to assess their impact on the virus. One similarity observed was that TGF β did not affect the infection rate of primary fibroblasts or their metabolic activity; however, these were the extent of the similarities.

Differences emerged in the virus replication curves, with TGF β having no significant impact, while exposure to hyperoxia led to a significant reduction. Moreover, TGF β treatment significantly decreased the initiation of apoptosis at 72 hours post-infection and did not influence the necrosis processes of primary fibroblasts. In contrast, hyperoxia exposure had a significant effect on decreasing the necrosis process within the first 24 hours of virus infection. Subsequent analysis using a wound healing "scratch" assay revealed no significant difference between control and TGF β -treated samples, unlike the pronounced effect of hyperoxia exposure. Collectively, these findings highlight distinct effects of fibroblast stimulation through TGF β treatment and hyperoxia exposure. TGF β operates through specific signaling pathways, such as the Smad-dependent

pathway, to regulate cellular processes like proliferation, differentiation, and extracellular matrix synthesis (Schiffer, M. et al, 200). Hyperoxia, on the other hand, primarily induces oxidative stress and can activate pathways associated with reactive oxygen species (ROS) production (Singer, M. et al, 2021). The diversity in signaling cascades can lead to different downstream effects in fibroblasts. TGF β treatment appeared to have a lesser impact on virus infection and its consequences in primary mouse fibroblasts.

Studies of the virus infection in patients with BPD are often presented as cohort research reviews of human samples. In contrast, many mouse model studies have primarily focused on the influence of BPD on adult illnesses, with mice being infected as adults at the age of 8 – 9 weeks (O'Reilly, M. A. et al, 2007). Here, my focus was on investigating the lifelong consequences of both virus infection and BPD and how infection can impact the development of BPD. To achieve this, MHV-68 infection was performed 8 days after exposing 5 – 8 days old mice to hyperoxia, allowing the pups time to rest and recover. This decision resulted in a stable and functional *in vivo* mouse model, with the health of the mice assessed based on their appearance and weight. This mouse model cannot be used to study severe BPD consequences or the high virus dosage impact because it requires relatively healthy, long-lived mice.

Multiple studies have indicated that hypoxia can enhance MHV-68 production (Andreansky et al., 2019). A comprehensive review of the interplay between oxygen levels and viral replication proposed that low oxygen can influence cellular metabolism, the immune system, and the efficacy of antiviral agents (Liu, P. J. et al, 2020). However, there is limited knowledge regarding the impact of hyperoxia exposure. For instance, the provision of 100% oxygen has been shown to induce inflammation and trigger a multicellular immune response (Hanidzar, D. et al, 2020).

In this study, I postulated that moderate oxygen concentrations may also influence following virus replication. I conducted investigations both *in vitro* and *in vivo* to explore this hypothesis. Notably, the viral replication curve exhibited a significant reduction in primary lung fibroblasts when exposed to hyperoxia for 24 hours. At the same time, the lytic titer in the mouse lungs increased significantly during the acute phase of viral infection. However, there was no change in the

viral genomic load in the mouse spleen, as both control and exposed to hyperoxia mice displayed similar trends.

These findings suggest that isolated mouse primary lung fibroblasts may respond differently to virus infection compared to the entire lung. Subsequent analysis revealed that these cells exhibited reduced proliferation and migration, which may explain the lower virus production, as viral replication is reliant on host cell amounts. The increased titer in mouse lungs could also be associated with enhanced immune response in lung cells due to the hyperoxia exposure, which could limit viral replication. Numerous experimental investigations in the past have confirmed the association between hyperoxia and adverse consequences, encompassing disruptions in immune responses, aberrant metabolic functions, and changes in hemodynamics and alveolar barrier integrity (Hanidziar, D. et al, 2021). Acute lung injury induced by hyperoxia is distinguished by the arrival of inflammatory cells, heightened pulmonary permeability, and damage or death of endothelial and epithelial cells. Cytokines play a role in coordinating some of these effects (Bhandari, V. and Elias, J. A., 2006). For a more comprehensive understanding of the increased virus titer in the lungs, it is advisable to assess titer from the first day after hyperoxia exposure to day 10 post-infection and to examine immune protein levels, for example, cytokines and interferons.

Histological examinations using H&E-staining on lung samples revealed that the double-hit model resulted in notable morphological alterations in adult alveoli. Notably, these changes were visually indistinguishable from those observed in mice infected with MHV-68. The Radial Alveolar Count (RAC) method serves as a reliable indicator of lung growth during intrauterine and early postnatal development, as well as throughout childhood. This methodology has found application in evaluating lung development under various experimental conditions (Ortega-Martínez, M. et al, 2014). In the current investigation, neither control mice nor those subjected solely to hyperoxia exposure or virus infection exhibited significant alterations in their RAC values. This finding is intriguing, especially when compared to other studies where hyperoxia exposure led to an increase in RAC in the lungs of rats (Liang, Z. et al, 2021) and mice (Wang, H. et al, 2014). It's noteworthy that in certain studies, hyperoxia exposure extended beyond 24 hours, lasting, for example, 7 days. Such prolonged exposure to elevated oxygen levels resulted in more pronounced changes in lung morphology than what we

observed in our experimental conditions. I consider that 24-hour exposure during the early days of life had a mild impact on lung morphology.

However, the double-hit model, involving concurrent hyperoxia exposure and MHV-68 infection, induced a significant increase in RAC numbers within mouse lungs on days 10, 28, and 5–6 months post-infection compared to instances of singular hyperoxia exposure or MHV-68 infection alone. Remarkably, the development of RAC displayed gender-specific patterns, with female mice manifesting elevated RAC numbers on day 10 post-infection, while male mice exhibited higher counts on day 28 post-infection.

This difference in RAC development can be attributed to the different rates of developmental changes occurring in female and male mice. Such variations may exert an influence on the response to both hyperoxia exposure and viral infection. The disparate peaks in the radial alveolar count at distinct time points likely mirror the different developmental characteristics of female and male mice.

Another indicative sign of BPD is the thickness of the alveolar septal wall (Pozarska, A. et al, 2017). In my study, the provision of additional oxygen at a 40% concentration did not result in any notable changes in wall thickness. Similarly, virus infection did not affect septal wall thickness. However, in the case of adult mice subjected to a double-hit model, there was a significant decrease in the septal thickness. Interestingly, preliminary exposure to hyperoxia made the alveolar walls more vulnerable to MHV-68 infection, underscoring the interdependent nature of these injuries. At the same time, neither hyperoxia exposure, nor MHV-68 infection, nor their combination had any impact on vessel count in the lungs. The observed changes could indicate a balance between processes promoting tissue repair and remodeling after a double-hit model in the lungs. Thinner alveolar walls might result from ongoing repair, while increased RAC reflects a compensatory mechanism to restore lung structure.

A pivotal discovery in the current investigation was the reduction in both cell proliferation and myofibroblast formation markers within the emphysema-like phenotype. Notably, the *in vitro* analysis of primary mouse lung fibroblasts indicated no changes in *Pcna* and *Acta2* gene expression during the initial 24 hours following virus infection. In contrast, *in vivo* analysis showed a significant decrease in these markers after MHV-68 infection in adult mice following a double-hit injury period of 5 to 6 months. This decline may be associated with the

impaired repair and remodeling processes in mouse lungs induced by the combination of hyperoxia exposure and MHV-68 infection. Taken together, these findings imply that cell-cycle arrest in the early stages of virus infection may be the initial event driving histological changes in adult lungs.

Another gene subjected to expression analysis, both *in vitro* and *in vivo*, was *Pdgfra*. This gene's expression is essential to septation and alveolarization and has been reported to be diminished in the alveoli of infants with BPD (Popova, A. et al, 2014). In my *in vitro* investigations, a significant reduction in protein and gene expression of *Pdgfra* was observed following MHV-68 infection in both control and hyperoxia-exposed fibroblasts. However, in the case of *in vivo* analysis, *Pdgfra* gene expression remained unchanged over time and across various experimental conditions. These findings may suggest that while *Pdgfra* expression is attenuated in human BPD samples, the chosen hyperoxia exposure and viral infection dose were insufficient to induce a significant shift in gene expression in adult mice, despite observable changes in the initial 24 hours post-infection. In future research projects, it would be advantageous to focus on the lytic acute phase of virus infection within the host organism. This emphasis would involve examining developmental and immune response pathways, alongside evaluating cell cycle checkpoints during the initial days of infection.

Hif1a is recognized as a crucial factor in the development of BPD and may potentially contribute to lung injury protection (Zhang, Y. et al, 2019). In contrast to other studies that have reported significant reductions in *Hif1a* gene expression in the lungs of rats with BPD (Hirsch, K. et al, 2020), our research uncovered no alterations in *Hif1a* gene expression in mouse lungs. It is important to note that oxygen-sensing proteins play a main role in the adaptive response to changes in oxygen levels, and this study did not investigate post-translational modifications that may be occurring.

Wnt5a stands out as a key gene linked to lung development, and its dysregulation has been associated with the initiation of various chronic lung diseases such as lung cancer, idiopathic pulmonary fibrosis (IPF), and chronic obstructive pulmonary disease (COPD) (Aros, C. J, et al, 2021; Liu, T. et al., 2021; Newman, D. R. et al., 2016). Inactivating *Wnt5a* during the postnatal phase disrupts alveologenesis, resulting in a phenotype reminiscent of bronchopulmonary dysplasia (BPD) (Li, C. et al, 2020). Studies involving healthy human fibroblasts

and fibroblasts from patients with pulmonary fibrosis have indicated an increase in Wnt5a expression, correlated with enhanced proliferation and resistance to apoptosis (Vuga et al., 2009). Our *in vivo* experiments revealed an upregulation of Wnt5a gene expression on day 10 post-infection following exposure to hyperoxia, but a downregulation at 5 to 6 months post-infection. Interestingly, on day 28 post-infection, gene expression levels appeared relatively consistent in controls and hyperoxia and MHV-68 infection treated mice. These fluctuations in Wnt5a expression highlight a complex mechanism, emphasizing the potential pivotal role that Wnt5a may play in lung development, injury, and repair.

Sex-related differences exist in many lung diseases throughout the lifespan (Carey, M. A. et al. 2007; Townsend, E. A. et al. 2012). Traditionally, due to limited clinical samples, researchers have often resorted to combining both sexes in their studies. However, recent years have witnessed the acknowledgment of sex as a factor that can influence the course and susceptibility to various illnesses. For example, asthma exhibits different patterns, more commonly afflicting boys during childhood and transitioning to a higher incidence in girls during adulthood. In contrast, COPD is more prevalent in women, while BPD tends to affect boys more than girls (Silveyra, P. et al, 2021, Townsel, C. D. et al, 2017). In my study, I conducted separate analyses for males and females to investigate potential differences. MHV-68 infection and hyperoxia exposure of mouse primary fibroblasts revealed no significant differences in females and males in the apoptosis, necrosis, proliferation, migration studies, and developmental *Pdgfra*, *Vegf*, and *Acta2* genes expression investigations. *In vivo* experiments yielded further insights. The lytic MHV-68 titer was notably elevated after hyperoxia exposure on days 3 and 6 post-infection, specifically in females. Radial alveolar count was significantly higher in males compared to those infected in normoxia, while it was lower in females. To gain a more comprehensive understanding of these sex-related differences, further analysis of the acute phase of virus infection is warranted.

Conclusions.

Viral infections are implicated in persistent lung injuries, contributing to fibrosis, with emerging focus on herpesviruses's role. This study aimed to clarify the impact of virus-induced pulmonary disturbances and hyperoxia-induced changes in lung development, as well as their reciprocal influence, employing the newly established by our group *in vitro* neonatal mouse lung fibroblast model and *in vivo* neonatal mouse model subjected to MHV-68 infection and hyperoxia (FiO₂ = 0.4, 24 hours). The 24-hour MHV-68 infection induced morphological changes, reduced fibroblast proliferation and migration, and altered gene expressions, suggesting virus-induced cell-cycle arrest. *In vivo*, the double-hit model revealed significant morphological alterations, increased Radial Alveolar Count, and gender-specific differences in developmental patterns. Contrasting effects of TGFβ and hyperoxia on virus replication were observed *in vitro*. BPD investigation implicated fibroblast responses to hyperoxia, hinting at adaptive mechanisms. Distinct effects were noted between immortalized and primary fibroblasts. Hyperoxia altered virus titer *in vitro* and *in vivo*, suggesting complex interactions influencing fibroblast responses. Histological changes correlated with altered gene expressions, emphasizing the need for detailed temporal analysis. The double-hit model's impact on BPD development, *Wnt5a* and *Hif1a* expressions, and sex-related differences underscored the complicated interplay between hyperoxia, viral infection, and lung development. The study provides insights into potential future investigations for mitigating virus-induced lung injuries and refining experimental models for BPD research.

References

- Alenzi, F.Q.B. (2004) 'Links between apoptosis, proliferation and the cell cycle', *British Journal of Biomedical Science*, 61(2), pp. 99–102. Available at: <https://doi.org/10.1080/09674845.2004.11732652>.
- Alsuwaidi, A.R. *et al.* (2017) 'Sirolimus alters lung pathology and viral load following influenza A virus infection', *Respiratory Research*, 18(1). Available at: <https://doi.org/10.1186/s12931-017-0618-6>.
- Altamirano-Lagos, M.J. *et al.* (2019) 'Current animal models for understanding the pathology caused by the respiratory syncytial virus', *Frontiers in Microbiology*, 10(MAY). Available at: <https://doi.org/10.3389/fmicb.2019.00873>.
- Alvira, C.M. (2016) 'Aberrant pulmonary vascular growth and remodeling in bronchopulmonary dysplasia', *Frontiers in Medicine*, 3(MAY). Available at: <https://doi.org/10.3389/fmed.2016.00021>.
- Amano, H. *et al.* (2021) 'VEGFR1-tyrosine kinase signaling in pulmonary fibrosis', *Inflammation and Regeneration*, 41(1). Available at: <https://doi.org/10.1186/s41232-021-00166-7>.
- Aros, C.J., Pantoja, C.J. and Gomperts, B.N. (2021) 'Wnt signaling in lung development, regeneration, and disease progression', *Communications Biology*, 4(1). Available at: <https://doi.org/10.1038/s42003-021-02118-w>.
- Askenazi, S.S. and Perlman, M. (1979) 'Pulmonary hypoplasia: Lung weight and radial alveolar count as criteria of diagnosis', *Archives of Disease in Childhood*, 54(8), pp. 614–618. Available at: <https://doi.org/10.1136/adc.54.8.614>.
- Baker, C.D. and Abman, S.H. (2015) 'Impaired pulmonary vascular development in bronchopulmonary dysplasia', in *Neonatology*. S. Karger AG, pp. 344–351. Available at: <https://doi.org/10.1159/000381129>.
- Banskota, S. *et al.* (2022) 'Engineered virus-like particles for efficient in vivo delivery of therapeutic proteins', *Cell*, 185(2), pp. 250-265.e16. Available at: <https://doi.org/10.1016/j.cell.2021.12.021>.
- Barratt, S.L. *et al.* (2018) 'VEGF (Vascular endothelial growth factor) and fibrotic lung disease', *International Journal of Molecular Sciences*, 19(5). Available at: <https://doi.org/10.3390/ijms19051269>.
- Been, J.V. and Zimmermann, L.J.I. (2009) 'Histological chorioamnionitis and respiratory outcome in preterm infants', *Archives of Disease in Childhood: Fetal and Neonatal Edition*, 94(3). Available at: <https://doi.org/10.1136/adc.2008.150458>.
- Bortz, E. *et al.* (2018) 'Proteomics of bronchoalveolar lavage fluid reveals a lung oxidative stress response in murine herpesvirus-68 infection', *Viruses*, 10(12). Available at: <https://doi.org/10.3390/v10120670>.
- Bose, C. *et al.* (2009) 'Fetal growth restriction and chronic lung disease among infants born before the 28th week of gestation', *Pediatrics*, 124(3). Available at: <https://doi.org/10.1542/peds.2008-3249>.
- Bourbon, J.R. *et al.* (2009) 'Bronchopulmonary dysplasia and emphysema: in search of common therapeutic targets', *Trends in Molecular Medicine*, 15(4), pp. 169–179. Available at: <https://doi.org/10.1016/j.molmed.2009.02.003>.
- Boyd, D.F. *et al.* (2020) 'Exuberant fibroblast activity compromises lung function via ADAMTS4', *Nature*, 587(7834), pp. 466–471. Available at: <https://doi.org/10.1038/s41586-020-2877-5>.

- Brauchle, E. *et al.* (2014) 'Cell death stages in single apoptotic and necrotic cells monitored by Raman microspectroscopy', *Scientific Reports*, 4. Available at: <https://doi.org/10.1038/srep04698>.
- Buczynski, B.W. *et al.* (2012) 'Lung development and the host response to influenza A virus are altered by different doses of neonatal oxygen in mice', *American Journal of Physiology - Lung Cellular and Molecular Physiology*, 302(10). Available at: <https://doi.org/10.1152/ajplung.00026.2012>.
- Burri, P.H. (2006) 'Structural aspects of postnatal lung development - Alveolar formation and growth', in *Biology of the Neonate*, pp. 313–322. Available at: <https://doi.org/10.1159/000092868>.
- Calabrese, F. *et al.* (2013) 'Herpes Virus Infection Is Associated with Vascular Remodeling and Pulmonary Hypertension in Idiopathic Pulmonary Fibrosis', *PLoS ONE*, 8(2). Available at: <https://doi.org/10.1371/journal.pone.0055715>.
- Carlo, W.A. *et al.* (2014) 'Respiratory support in preterm infants at birth', *Pediatrics*, 133(1), pp. 171–174. Available at: <https://doi.org/10.1542/peds.2013-3442>.
- Ceneviva, Z.J., Norlander, A.E. and Stokes Peebles, R. (2022) 'Mouse Models of Respiratory Syncytial Virus Infection', in *Methods in Molecular Biology*. Humana Press Inc., pp. 19–41. Available at: https://doi.org/10.1007/978-1-0716-2364-0_2.
- Chen, I.T. *et al.* (2022) 'Molecular mechanisms underlying hyperoxia-induced lung fibrosis', *Pediatrics and Neonatology*, 63(2), pp. 109–116. Available at: <https://doi.org/10.1016/j.pedneo.2021.11.008>.
- Cigana, C. *et al.* (2016) 'Tracking the immunopathological response to *Pseudomonas aeruginosa* during respiratory infections', *Scientific Reports*, 6. Available at: <https://doi.org/10.1038/srep21465>.
- Collins, C.M. and Speck, S.H. (2012) 'Tracking murine gammaherpesvirus 68 infection of germinal center B cells in vivo', *PLoS ONE*, 7(3). Available at: <https://doi.org/10.1371/journal.pone.0033230>.
- Cooney, T.P. and Thurlbeck, W.M. (no date) *The radial alveolar count method of Emery and Mithal: a reappraisal 1-Postnatal lung growth*.
- Costa, Robert H *et al.* (2001) *Transcription factors in mouse lung development and function*, *Am J Physiol Lung Cell Mol Physiol*, pp. 823–838. Available at: <http://www.ajplung.org/L823>.
- Davidson, M.R., Gazdar, A.F. and Clarke, B.E. (2013) 'The pivotal role of pathology in the management of lung cancer', *Journal of Thoracic Disease*, 5(SUPPL.5). Available at: <https://doi.org/10.3978/j.issn.2072-1439.2013.08.43>.
- Dayaram, T. and Marriott, S.J. (2008) 'Effect of transforming viruses on molecular mechanisms associated with cancer', *Journal of Cellular Physiology*, 216(2), pp. 309–314. Available at: <https://doi.org/10.1002/jcp.21439>.
- Dong, S., Forrest, J.C. and Liang, X. (2017) 'Murine gammaherpesvirus 68: A small animal model for gammaherpesvirus-associated diseases', in *Advances in Experimental Medicine and Biology*. Springer New York LLC, pp. 225–236. Available at: https://doi.org/10.1007/978-981-10-5765-6_14.
- Doyle, L.W. *et al.* (2017) 'Ventilation in Extremely Preterm Infants and Respiratory Function at 8 Years', *New England Journal of Medicine*, 377(4), pp. 329–337. Available at: <https://doi.org/10.1056/nejmoa1700827>.
- Drakopanagiotakis, F. *et al.* (2008) 'Apoptosis in lung injury and fibrosis', *European Respiratory Journal*, 32(6), pp. 1631–1638. Available at: <https://doi.org/10.1183/09031936.00176807>.

- Du, Y. *et al.* (2021) 'In Vivo Mouse Models for Hepatitis B Virus Infection and Their Application', *Frontiers in Immunology*, 12. Available at: <https://doi.org/10.3389/fimmu.2021.766534>.
- Dushianthan, A. *et al.* (2023) 'Alveolar Hyperoxia and Exacerbation of Lung Injury in Critically Ill SARS-CoV-2 Pneumonia', *Medical Sciences*, 11(4), p. 70. Available at: <https://doi.org/10.3390/medsci11040070>.
- Dylag, A.M. *et al.* (2020) 'Pulmonary mechanics and structural lung development after neonatal hyperoxia in mice', *Pediatric Research*, 87(7), pp. 1201–1210. Available at: <https://doi.org/10.1038/s41390-019-0723-y>.
- Ebrahimi, B. *et al.* (2001) Murine Gammaherpesvirus-68 Infection Causes Multi-Organ Fibrosis and Alters Leukocyte Trafficking in Interferon-Receptor Knockout Mice, *American Journal of Pathology*.
- Elattal, R. *et al.* (2013) 'Pulmonary alveolar and vascular morphometry after gel plug occlusion of the trachea in a fetal rabbit model of CDH', *International Journal of Surgery*, 11(7), pp. 558–561. Available at: <https://doi.org/10.1016/j.ijso.2013.05.033>.
- Elmore, S. *Apoptosis: A Review of Programmed Cell Death*.
- Engel, M. *et al.* (2020) 'A comparison of four different models of acute respiratory distress syndrome in sheep', *Respiratory Research*, 21(1). Available at: <https://doi.org/10.1186/s12931-020-01475-0>.
- Ewers, M. *et al.* (2019) *ALZHEIMER'S DISEASE Increased soluble TREM2 in cerebrospinal fluid is associated with reduced cognitive and clinical decline in Alzheimer's disease for the Alzheimer's Disease Neuroimaging Initiative*, *Sci. Transl. Med.*, p. 6221. Available at: <http://stm.sciencemag.org/>.
- Farrar, B.G. *et al.* (no date) *Reporting and interpreting non-significant results in animal cognition research*.
- Gan, E.S. and Ooi, E.E. (2020) 'Oxygen: Viral friend or foe?', *Virology Journal*, 17(1). Available at: <https://doi.org/10.1186/s12985-020-01374-2>.
- George, P.M. *et al.* (2022) *A persistent neutrophil-associated immune signature characterizes post-COVID-19 pulmonary sequelae*. Available at: <https://www.science.org>.
- Ghonim, M.A. *et al.* (2023) 'Pulmonary inflammation and fibroblast immunoregulation: from bench to bedside', *Journal of Clinical Investigation*, 133(17). Available at: <https://doi.org/10.1172/JCI170499>.
- Giusto, K. *et al.* (2021) 'Hyperoxia-induced bronchopulmonary dysplasia: Better models for better therapies', *DMM Disease Models and Mechanisms*, 14(2). Available at: <https://doi.org/10.1242/DMM.047753>.
- Golden, T. *et al.* (2021) 'Comprehensive dataset to assess morphological changes subsequent to bleomycin exposure', *Data in Brief*, 37. Available at: <https://doi.org/10.1016/j.dib.2021.107270>.
- Grus, J. (2019) *Data Science from Scratch SECOND EDITION First Principles with Python*. Available at: <http://oreilly.com>.
- Gualdoni, G.A. *et al.* (2018) 'Rhinovirus induces an anabolic reprogramming in host cell metabolism essential for viral replication', *Proceedings of the National Academy of Sciences of the United States of America*, 115(30), pp. E7158–E7165. Available at: <https://doi.org/10.1073/pnas.1800525115>.
- Hanson, K.M. *et al.* (2019) 'Apoptosis Resistance in Fibroblasts Precedes Progressive Scarring in Pulmonary Fibrosis and Is Partially Mediated by Toll-Like Receptor 4 Activation', *Toxicological Sciences*, 170(2), pp. 489–498. Available at: <https://doi.org/10.1093/toxsci/kfz103>.

- Herring, M.J. *et al.* (2014) 'Growth of alveoli during postnatal development in humans based on stereological estimation', *Am J Physiol Lung Cell Mol Physiol*, 307, pp. 338–344. Available at: <https://doi.org/10.1152/ajplung.00094.2014.-Al>.
- Holtkötter, H. *et al.* (2018) 'Forensic differentiation between peripheral and menstrual blood in cases of alleged sexual assault—validating an immunochromatographic multiplex assay for simultaneous detection of human hemoglobin and D-dimer', *International Journal of Legal Medicine*, 132(3), pp. 683–690. Available at: <https://doi.org/10.1007/s00414-017-1719-y>.
- Hu, J., Wang, Y. and Yuan, Y. (2021) 'Inhibitors of APE1 redox function effectively inhibit γ -herpesvirus replication in vitro and in vivo', *Antiviral Research*, 185. Available at: <https://doi.org/10.1016/j.antiviral.2020.104985>.
- Huang, R. *et al.* (2021) 'Hypoxia and viral infectious diseases', *JCI Insight*, 6(7). Available at: <https://doi.org/10.1172/jci.insight.147190>.
- Huang, W.J. and Tang, X.X. (2021) 'Virus infection induced pulmonary fibrosis', *Journal of Translational Medicine*, 19(1). Available at: <https://doi.org/10.1186/s12967-021-03159-9>.
- Hurskainen, M. *et al.* (2021) 'Single cell transcriptomic analysis of murine lung development on hyperoxia-induced damage', *Nature Communications*, 12(1). Available at: <https://doi.org/10.1038/s41467-021-21865-2>.
- Imai, K. *et al.* (2005) 'Correlation of lung surface area to apoptosis and proliferation in human emphysema', *European Respiratory Journal*, 25(2), pp. 250–258. Available at: <https://doi.org/10.1183/09031936.05.00023704>.
- Jaramillo-Rangel, G. *et al.* (2023) 'Back to the Basics: Usefulness of Naturally Aged Mouse Models and Immunohistochemical and Quantitative Morphologic Methods in Studying Mechanisms of Lung Aging and Associated Diseases', *Biomedicines*, 11(7). Available at: <https://doi.org/10.3390/biomedicines11072075>.
- Jobe, A.H. and Kallapur, S.G. (2010) 'Long term consequences of oxygen therapy in the neonatal period', *Seminars in Fetal and Neonatal Medicine*, 15(4), pp. 230–235. Available at: <https://doi.org/10.1016/j.siny.2010.03.007>.
- Keeler, S.P. *et al.* (2018) 'Influenza A Virus Infection Causes Chronic Lung Disease Linked to Sites of Active Viral RNA Remnants', *The Journal of Immunology*, 201(8), pp. 2354–2368. Available at: <https://doi.org/10.4049/jimmunol.1800671>.
- Kelly, N.J. *et al.* (2016) 'Automated measurement of blood vessels in tissues from microscopy images', *Current Protocols in Cytometry*, 2016, p. 12.44.1-12.44.13. Available at: <https://doi.org/10.1002/cpcy.10>.
- Kranz, K.M. and Siepmann, G. *MHV-68 Mausmodell Entzündliche Organveränderungen (ZNS, Herz und Lunge) nach neonataler MHV-68 Infektion bei B6-(Rag1) TM-, BALB/c wildtyp-und C57BL/6 wildtyp-Mäusen.*
- Kutle, I., Dittrich, A. and Wirth, D. (2023) 'Mouse Models for Human Herpesviruses', *Pathogens*, 12(7). Available at: <https://doi.org/10.3390/pathogens12070953>.
- Lam, D.K. *et al.* (2023) 'Improved cytosine base editors generated from TadA variants', *Nature Biotechnology*, 41(5), pp. 686–697. Available at: <https://doi.org/10.1038/s41587-022-01611-9>.
- Langer, C.J. *et al.* (2010) 'The evolving role of histology in the management of advanced non - small-cell lung cancer', *Journal of Clinical Oncology*, 28(36), pp. 5311–5320. Available at: <https://doi.org/10.1200/JCO.2010.28.8126>.
- Lee, S. *et al.* (2018) 'Influenza A Virus Infection Triggers Pyroptosis and Apoptosis of Respiratory Epithelial Cells through the Type I Interferon Signaling Pathway in a Mutually

- Exclusive Manner', *Journal of Virology*, 92(14). Available at: <https://doi.org/10.1128/jvi.00396-18>.
- Leung, V. *et al.* (2018) 'Arrive has not arrived: Support for the arrive (animal research: Reporting of in vivo experiments) guidelines does not improve the reporting quality of papers in animal welfare, analgesia or anesthesia', *PLoS ONE*, 13(5). Available at: <https://doi.org/10.1371/journal.pone.0197882>.
- Liang, C.C., Park, A.Y. and Guan, J.L. (2007) 'In vitro scratch assay: A convenient and inexpensive method for analysis of cell migration in vitro', *Nature Protocols*, 2(2), pp. 329–333. Available at: <https://doi.org/10.1038/nprot.2007.30>.
- Lignelli, X.E. *et al.* (2019) 'Recent advances in our understanding of the mechanisms of lung alveolarization and bronchopulmonary dysplasia', *Am J Physiol Lung Cell Mol Physiol*, 317, pp. 832–887. Available at: <https://doi.org/10.1152/ajplung.00369.2019.-Bronchopulmonary>.
- Lilien, T.A. *et al.* (2022) 'Long-Term Pulmonary Dysfunction by Hyperoxia Exposure during Severe Viral Lower Respiratory Tract Infection in Mice', *Pathogens*, 11(11). Available at: <https://doi.org/10.3390/pathogens11111334>.
- Linden, D. *et al.* (2019) 'Respiratory viral infection: A potential "missing link" in the pathogenesis of COPD', *European Respiratory Review*, 28(151). Available at: <https://doi.org/10.1183/16000617.0063-2018>.
- Lingappan, K. and Savani, R.C. (2020) 'The wnt signaling pathway and the development of bronchopulmonary dysplasia', *American Journal of Respiratory and Critical Care Medicine*, 201(10), pp. 1174–1176. Available at: <https://doi.org/10.1164/rccm.202002-0277ED>.
- Liu, B. *et al.* (2022) 'A split prime editor with untethered reverse transcriptase and circular RNA template', *Nature Biotechnology*, 40(9), pp. 1388–1393. Available at: <https://doi.org/10.1038/s41587-022-01255-9>.
- Liu, P.J. *et al.* (2020) 'Oxygen sensing and viral replication: Implications for tropism and pathogenesis', *Viruses*, 12(11). Available at: <https://doi.org/10.3390/v12111213>.
- López-Rodríguez, D.M. *et al.* (2019) 'A role of hypoxia-inducible factor 1 alpha in Mouse Gammaherpesvirus 68 (MHV68) lytic replication and reactivation from latency', *PLoS Pathogens*, 15(12). Available at: <https://doi.org/10.1371/journal.ppat.1008192>.
- Malinow, R. *et al.* (2010) 'Introduction of green fluorescent protein (GFP) into hippocampal neurons through viral infection', *Cold Spring Harbor Protocols*, 5(4). Available at: <https://doi.org/10.1101/pdb.prot5406>.
- Mallia, P. *et al.* (2007) *Exacerbations of Asthma and Chronic Obstructive Pulmonary Disease (COPD): Focus on Virus Induced Exacerbations*, *Current Pharmaceutical Design*, pp. 73–97.
- Manicassamy, B. *et al.* (2010) 'Analysis of in vivo dynamics of influenza virus infection in mice using a GFP reporter virus', *Proceedings of the National Academy of Sciences of the United States of America*, 107(25), pp. 11531–11536. Available at: <https://doi.org/10.1073/pnas.0914994107>.
- Margraf, L.R. *et al.* (1991) *Morphometric Analysis of the Lung in Bronchopulmonary Dysplasia 1-3*, *AM REV RESPIR DIS*, pp. 391–400.
- Martinotti, S. and Ranzato, E. (2020) 'Scratch wound healing assay', in *Methods in Molecular Biology*. Humana Press Inc., pp. 225–229. Available at: https://doi.org/10.1007/7651_2019_259.
- Massa, C.B. *et al.* (2017) 'Histologic and biochemical alterations predict pulmonary mechanical dysfunction in aging mice with chronic lung inflammation', *PLoS*

- computational biology*, 13(8), p. e1005570. Available at: <https://doi.org/10.1371/journal.pcbi.1005570>.
- McClelland, R.D., Culp, T.N. and Marchant, D.J. (2021) 'Imaging Flow Cytometry and Confocal Immunofluorescence Microscopy of Virus-Host Cell Interactions', *Frontiers in Cellular and Infection Microbiology*, 11. Available at: <https://doi.org/10.3389/fcimb.2021.749039>.
- McManus, T.E. *et al.* (2008) 'High levels of Epstein-Barr virus in COPD', *European Respiratory Journal*, 31(6), pp. 1221–1226. Available at: <https://doi.org/10.1183/09031936.00107507>.
- Melville, J.M. and Moss, T.J.M. (2013) 'The immune consequences of preterm birth', *Frontiers in Neuroscience* [Preprint], (7 MAY). Available at: <https://doi.org/10.3389/fnins.2013.00079>.
- Montaudon, M. *et al.* (2007) 'Assessment of bronchial wall thickness and lumen diameter in human adults using multi-detector computed tomography: Comparison with theoretical models', *Journal of Anatomy*, 211(5), pp. 579–588. Available at: <https://doi.org/10.1111/j.1469-7580.2007.00811.x>.
- Mora AL, Woods CR, Garcia A, *et al.* Lung infection with gamma-herpesvirus induces progressive pulmonary fibrosis in Th2-biased mice. *Am J Physiol Lung Cell Mol Physiol*. 2005;289(5):L711-L721. Available at: <https://doi:10.1152/ajplung.00007.2005>.
- Mrázová, V. *et al.* (2015) 'Murine gammaherpesvirus (MHV-68) transforms cultured cells in vitro', *Intervirology*, 58(2), pp. 69–72. Available at: <https://doi.org/10.1159/000370071>.
- Mund, S.I., Stampanoni, M. and Schittny, J.C. (2008) 'Developmental alveolarization of the mouse lung', *Developmental Dynamics*, 237(8), pp. 2108–2116. Available at: <https://doi.org/10.1002/dvdy.21633>.
- Namba, F. (2021) 'An experimental animal model of bronchopulmonary dysplasia: Secondary publication', *Pediatrics International*, 63(5), pp. 504–509. Available at: <https://doi.org/10.1111/ped.14612>.
- Newman, D.R. *et al.* (2016) 'Expression of WNT5A in Idiopathic Pulmonary Fibrosis and Its Control by TGF- β and WNT7B in Human Lung Fibroblasts', *Journal of Histochemistry and Cytochemistry*, 64(2), pp. 99–111. Available at: <https://doi.org/10.1369/0022155415617988>.
- Neyts, J. and De Clercq, E. (1998) *In Vitro and In Vivo Inhibition of Murine Gamma Herpesvirus 68 Replication by Selected Antiviral Agents*, pp. 170–172.
- O'Reilly, M.A. *et al.* (2008) 'Neonatal hyperoxia enhances the inflammatory response in adult mice infected with influenza A virus', *American Journal of Respiratory and Critical Care Medicine*, 177(10), pp. 1103–1110. Available at: <https://doi.org/10.1164/rccm.200712-1839OC>.
- O'Reilly, M.A. *et al.* (2012) 'Neonatal oxygen increases sensitivity to influenza A virus infection in adult mice by suppressing epithelial expression of Ear1', *American Journal of Pathology*, 181(2), pp. 441–451. Available at: <https://doi.org/10.1016/j.ajpath.2012.05.005>.
- Ortega-Martínez, M. *et al.* (2014) *Radial alveolar count assessment in the aging*. Available at: <https://www.researchgate.net/publication/264496571>.
- Paladino, P. *et al.* (2014) 'Identification of Herpesvirus Proteins That Contribute to G 1 /S Arrest', *Journal of Virology*, 88(8), pp. 4480–4492. Available at: <https://doi.org/10.1128/jvi.00059-14>.
- Palmer, C.S. (2022) 'Innate metabolic responses against viral infections', *Nature Metabolism*, 4(10), pp. 1245–1259. Available at: <https://doi.org/10.1038/s42255-022-00652-3>.

- Popova, A.P. (2013) 'Mechanisms of bronchopulmonary dysplasia', *Journal of Cell Communication and Signaling*, 7(2), pp. 119–127. Available at: <https://doi.org/10.1007/s12079-013-0190-x>.
- Popova, A.P. *et al.* (2014) 'Reduced platelet-derived growth factor receptor expression is a primary feature of human bronchopulmonary dysplasia', *American Journal of Physiology - Lung Cellular and Molecular Physiology*, 307(3). Available at: <https://doi.org/10.1152/ajplung.00342.2013>.
- Pozarska, A. *et al.* (2017) 'Stereological monitoring of mouse lung alveolarization from the early postnatal period to adulthood', *Am J Physiol Lung Cell Mol Physiol*, 312, pp. 882–895. Available at: <https://doi.org/10.1152/ajplung.00492>.
- Ptaschinski, C. and Rochford, R. (2008) 'Infection of neonates with murine gammaherpesvirus 68 results in enhanced viral persistence in lungs and absence of infectious mononucleosis syndrome', *Journal of General Virology*, 89(5), pp. 1114–1121. Available at: <https://doi.org/10.1099/vir.0.83470-0>.
- Resch, B. *et al.* (2016) 'Prematurity and the burden of influenza and respiratory syncytial virus disease', *World Journal of Pediatrics*, 12(1), pp. 8–18. Available at: <https://doi.org/10.1007/s12519-015-0055-x>.
- Riccetti, M.R. *et al.* (2022) 'Maladaptive functional changes in alveolar fibroblasts due to perinatal hyperoxia impair epithelial differentiation'. Available at: <https://doi.org/10.1172/jci>.
- Sacher, C. *et al.* (2020) 'Asymmetry of fibrillar plaque burden in amyloid mouse models', *Journal of Nuclear Medicine*, 61(12), pp. 1825–1831. Available at: <https://doi.org/10.2967/jnumed.120.242750>.
- Saito, A., Horie, M. and Nagase, T. (2018) 'TGF- β signaling in lung health and disease', *International Journal of Molecular Sciences*, 19(8). Available at: <https://doi.org/10.3390/ijms19082460>.
- Santos, D.P. *et al.* (2016) 'Comprehensive protocols for CRISPR/Cas9-based gene editing in human pluripotent stem cells', *Current Protocols in Stem Cell Biology*, 2016. Available at: <https://doi.org/10.1002/cpsc.15>.
- Schiffer, M. *et al.* (2000) *Smad proteins and transforming growth factor-signaling*, *Kidney International*.
- Schlepckow, K. *et al.* (2020) 'Enhancing protective microglial activities with a dual function TREM 2 antibody to the stalk region', *EMBO Molecular Medicine*, 12(4). Available at: <https://doi.org/10.15252/emmm.201911227>.
- Schutte, B. *et al.* (1998) *Annexin V binding assay as a tool to measure apoptosis in differentiated neuronal cells*, *Journal of Neuroscience Methods*, pp. 63–69.
- Shrestha, D. *et al.* (2021) 'Pulmonary immune cell transcriptome changes in double-hit model of BPD induced by chorioamnionitis and postnatal hyperoxia', *Pediatric Research*, 90(3), pp. 565–575. Available at: <https://doi.org/10.1038/s41390-020-01319-z>.
- Singanayagam, A. *et al.* (2012) 'Viruses exacerbating chronic pulmonary disease: The role of immune modulation', *BMC Medicine*, 10. Available at: <https://doi.org/10.1186/1741-7015-10-27>.
- Soutiere, S.E., Tankersley, C.G. and Mitzner, W. (2004) 'Differences in alveolar size in inbred mouse strains', *Respiratory Physiology and Neurobiology*, 140(3), pp. 283–291. Available at: <https://doi.org/10.1016/j.resp.2004.02.003>.
- Stevenson, P.G. and Efsthathiou, S. (2005) *Review Immune Mechanisms in Murine Gammaherpesvirus-68 Infection*, *VIRAL IMMUNOLOGY*.
- Subramaniam, K., Kumar, H. and Tawhai, M.H. (2017) 'Evidence for age-dependent air-space enlargement contributing to loss of lung tissue elastic recoil pressure and

- increased shear modulus in older age', *J Appl Physiol*, 123, pp. 79–87. Available at: <https://doi.org/10.1152/jappphysiol.00208.2016.-As>.
- Sucré, J.M.S. *et al.* (2020) 'Hyperoxia injury in the developing lung is mediated by mesenchymal expression of Wnt5A', *American Journal of Respiratory and Critical Care Medicine*, 201(10), pp. 1249–1262. Available at: <https://doi.org/10.1164/RCCM.201908-1513OC>.
- Sumbria, D. *et al.* (2021) 'Virus Infections and Host Metabolism—Can We Manage the Interactions?', *Frontiers in Immunology*, 11. Available at: <https://doi.org/10.3389/fimmu.2020.594963>.
- Suzuki, K. *et al.* (2016) 'In vivo genome editing via CRISPR/Cas9 mediated homology-independent targeted integration', *Nature*, 540(7631), pp. 144–149. Available at: <https://doi.org/10.1038/nature20565>.
- Suzuki, K. and Izpisua Belmonte, J.C. (2018) 'In vivo genome editing via the HITI method as a tool for gene therapy', *Journal of Human Genetics*, 63(2), pp. 157–164. Available at: <https://doi.org/10.1038/s10038-017-0352-4>.
- Thébaud, B. *et al.* (2019) 'Bronchopulmonary dysplasia', *Nature Reviews Disease Primers*, 5(1). Available at: <https://doi.org/10.1038/s41572-019-0127-7>.
- Todd, N.W., Luzina, I.G. and Atamas, S.P. (2012) 'Molecular and cellular mechanisms of pulmonary fibrosis', *Fibrogenesis and Tissue Repair*, 5(1). Available at: <https://doi.org/10.1186/1755-1536-5-11>.
- Townsi, N. *et al.* (2018) 'The impact of respiratory viruses on lung health after preterm birth', *European Clinical Respiratory Journal*, 5(1). Available at: <https://doi.org/10.1080/20018525.2018.1487214>.
- Trompet, E. *et al.* (2020) 'Viral fitness of MHV-68 viruses harboring drug resistance mutations in the protein kinase or thymidine kinase', *Antiviral Research*, 182. Available at: <https://doi.org/10.1016/j.antiviral.2020.104901>.
- Truog, W.E. *et al.* (2008) *Chronic Hypoxia and Rat Lung Development: Analysis by Morphometry and Directed Microarray*.
- Vastag, L. *et al.* (2011) 'Divergent effects of human cytomegalovirus and herpes simplex virus-1 on cellular metabolism', *PLoS Pathogens*, 7(7). Available at: <https://doi.org/10.1371/journal.ppat.1002124>.
- Wang, C. *et al.* (2022) 'The heterogeneous immune landscape between lung adenocarcinoma and squamous carcinoma revealed by single-cell RNA sequencing', *Signal Transduction and Targeted Therapy*, 7(1). Available at: <https://doi.org/10.1038/s41392-022-01130-8>.
- Wang, Y., Tibbetts, S.A. and Krug, L.T. (2021) 'Annual Review of Virology Conquering the Host: Determinants of Pathogenesis Learned from Murine Gammaherpesvirus 68'. Available at: <https://doi.org/10.1146/annurev-virology-011921>.
- Wendisch, D. *et al.* (2021) 'SARS-CoV-2 infection triggers profibrotic macrophage responses and lung fibrosis', *Cell*, 184(26), pp. 6243–6261.e27. Available at: <https://doi.org/10.1016/j.cell.2021.11.033>.
- Wickramasinghe, L.C. *et al.* (2021) 'An Experimental Model of Bronchopulmonary Dysplasia Features Long-Term Retinal and Pulmonary Defects but Not Sustained Lung Inflammation', *Frontiers in Pediatrics*, 9. Available at: <https://doi.org/10.3389/fped.2021.689699>.
- Williams, K.J. (2014) 'Gammaherpesviruses and Pulmonary Fibrosis: Evidence From Humans, Horses, and Rodents', *Veterinary Pathology*, 51(2), pp. 372–384. Available at: <https://doi.org/10.1177/0300985814521838>.

Wu, J. *et al.* (2020) 'Chest CT Findings in Patients with Coronavirus Disease 2019 and Its Relationship with Clinical Features', *Investigative Radiology*, 55(5), pp. 257–261. Available at: <https://doi.org/10.1097/RLI.0000000000000670>.

Xia, S. *et al.* (2023) 'Neonatal hyperoxia induces activated pulmonary cellular states and sex-dependent transcriptomic changes in a model of experimental bronchopulmonary dysplasia', *American Journal of Physiology - Lung Cellular and Molecular Physiology*, 324(2), pp. L123–L140. Available at: <https://doi.org/10.1152/ajplung.00252.2022>.

Yamada, T. *et al.* (2013) 'Airspace enlargement with fibrosis shows characteristic histology and immunohistology different from usual interstitial pneumonia, nonspecific interstitial pneumonia and centrilobular emphysema', *Pathology International*, 63(4), pp. 206–213. Available at: <https://doi.org/10.1111/pin.12054>.

Yee, M. *et al.* (2020) 'Neonatal hyperoxia enhances age-dependent expression of SARS-CoV-2 receptors in mice', *Scientific Reports*, 10(1). Available at: <https://doi.org/10.1038/s41598-020-79595-2>.

Yin, Z. *et al.* 'Development of A Neonatal Mouse Model for Coxsackievirus B1 Antiviral Evaluation'. Available at: <https://doi.org/10.1007/s12250>.

Yumlu, S. *et al.* (2017) 'Gene editing and clonal isolation of human induced pluripotent stem cells using CRISPR/Cas9', *Methods*, 121–122, pp. 29–44. Available at: <https://doi.org/10.1016/j.ymeth.2017.05.009>.

Zhao, S. meng *et al.* (2018) 'Primary culture of lung fibroblasts from hyperoxia-exposed rats and a proliferative characteristics study', *Cytotechnology*, 70(2), pp. 751–760. Available at: <https://doi.org/10.1007/s10616-017-0179-z>.

Acknowledgments

I would like to express my gratitude to all those who have contributed to the completion of this work.

I want to thank my supervisor, Prof. Dr. Heiko Adler, for his professional supervision over the past years. It was my great pleasure to work together with him.

Special thanks go to Dr. Anne Hilgendorff, the Principal Investigator, for her invaluable support, guidance, and contributions.

I would like to extend my sincere appreciation to PD Dr. Barbara Adler, a member of my thesis committee, for her valuable feedback and suggestions throughout the research project.

I extend my gratitude to former and current members of the AH group, including Motaharehsadat Heydarian, Prajakta Oak, Carola Voss, Julia Waiden, Juliane Schneider, Susanne Mehring, Elisabeth Schindler, Aakruti Nayak, Friederike Haefner, and Inga Meincke provided essential scientific input and technical support. Their friendship and good times during the project were also greatly appreciated.

Erika Gonzalez Rodriguez, PhD, I thank you deeply for your support and exceptional help.

Ursula Rambold, Helmholtz Zentrum in Munich, provided valuable support and assistance with flow cytometry analysis. I am grateful for her expertise and contributions.

My sincere gratitude goes to my fellow PhD students, especially Anna Herbst and Angelika Fischbeck, for generously imparting their expertise, insights, and recommendations on the day-to-day operations in the lab.

I also thank Daniela Dietel, Elisabeth Hennen, Anastasia Van der Berg, and all technical assistants and administrative staff at the Comprehensive Pneumology administrative staff at the Comprehensive Pneumology centre for their invaluable assistance and support.

Special thanks to Dr. Claudia Staab-Weijnitz and Dr. Melanie Penning for their excellent support in guiding every PhD candidate throughout the procedure.

Many thanks to all my friends and family who have provided me with great support over the past years and have always believed in me.

Affidavit



Affidavit

Dmitrieva, Anna

Surname, first name

Marchioninstr.

Street

81377, München, Germany

Zip code, town, country

I hereby declare, that the submitted thesis entitled:

Virus infections as risk factors in the development of bronchopulmonary dysplasia (BPD)

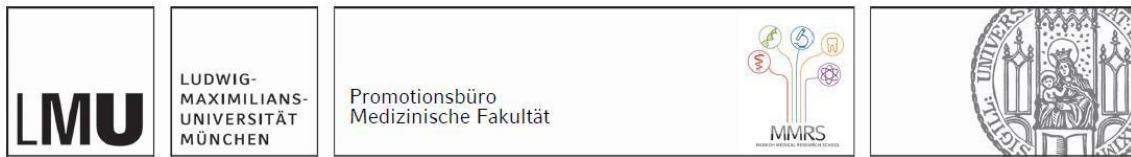
is my own work. I have only used the sources indicated and have not made unauthorised use of services of a third party. Where the work of others has been quoted or reproduced, the source is always given.

I further declare that the dissertation presented here has not been submitted in the same or similar form to any other institution for the purpose of obtaining an academic degree.

Erlangen, 24.06.2024
place, date

Anna Dmitrieva
Signature doctoral candidate

Confirmation of congruency



**Confirmation of congruency between printed and electronic version of
the doctoral thesis**

Dmitrieva, Anna

Surname, first name

Marchioninstr.

Street

81377, München, Germany

Zip code, town, country

I hereby declare, that the submitted thesis entitled:

Virus infections as risk factors in the development of bronchopulmonary dysplasia (BPD)
.....

is congruent with the printed version both in content and format.

Erlangen, 24.06.2024

place, date

Anna Dmitrieva

Signature doctoral candidate